

AD-A160 188 THE INFLUENCE OF SPECIFIC FACTORS AFFECTING SPALL IN  
EXPLOSIVELY LOADED S. (U) APPLIED RESEARCH ASSOCIATES  
INC ALBUQUERQUE NM D H MERKLE ET AL. 22 MAR 85  
UNCLASSIFIED AFOSR-TR-85-0834 F49620-83-C-0145 F/G 8/13

THE INFLUENCE OF SPECIFIC FACTORS AFFECTING SPALL IN  
EXPLOSIVELY LOADED S. (U) APPLIED RESEARCH ASSOCIATES  
INC ALBUQUERQUE NM D H MERKLE ET AL. 22 MAR 85  
AFOSR-TR-85-0834 F49620-83-C-0145 F/G 8/13

141

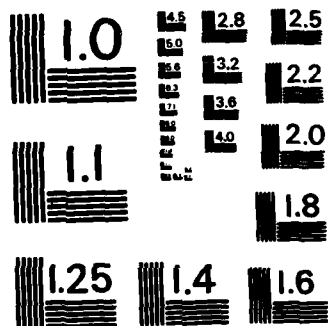
AFOSR-TR-85-0834 F49620-83-C-0145

F/G 8/13

NL

END

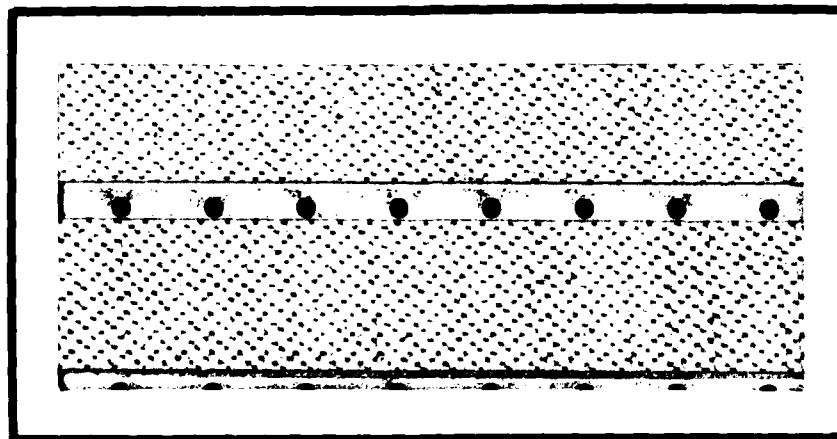
5. **THE MEETING**



MICROCOPY RESOLUTION TEST CHART  
NATIONAL BUREAU OF STANDARDS-1963-A

(2)

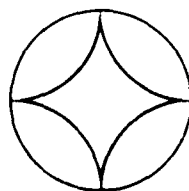
AD-A160 188



DTIC  
ELECTE  
OCT 15 1985  
A

Approved for public release;  
distribution unlimited.

DTIC FILE COPY



APPLIED  
RESEARCH  
ASSOCIATES, INC.

Engineering and Applied Science

85 10 11 054

②

AIR FORCE OFFICE OF SCIENTIFIC RESEARCH ALBES  
UNCLASSIFIED

MATTHEW J. ... Division  
Chief, Technical ...

THE INFLUENCE OF SPECIFIC FACTORS AFFECTING SPALL  
IN EXPLOSIVELY LOADED SOIL

Douglas H. Merkle  
James C. Partch  
Peter T. Dzwilewski

Applied Research Associates, Inc.  
4300 San Mateo Blvd. NE, Suite A220  
Albuquerque, NM 87110

22 March 1985

Final Report for the Period 1 August 1983-31 January 1985

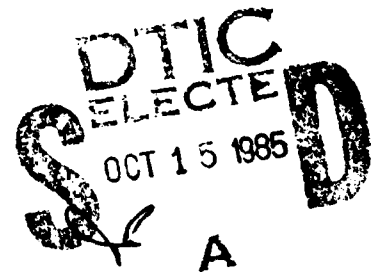
Contract No. F49620-83-C-0145

This work sponsored by the Air Force Office of  
Scientific Research under

Program Element 61102F  
Project 2309  
Task A1

Prepared for  
Director of Physical and Geophysical Sciences  
Air Force Office of Scientific Research  
Bolling AFB, DC 20332

UNCLASSIFIED



**SECURITY CLASSIFICATION OF THIS PAGE (When Data Entered)**

DD FORM 1473  
1 JAN 73

**EDITION OF 1 NOV 65 IS OBSOLETE**

UNCLASSIFIED

**SECURITY CLASSIFICATION OF THIS PAGE (When Data Entered)**

UNCLASSIFIED

SECURITY CLASSIFICATION OF THIS PAGE(When Data Entered)

> observation that the computed directly coupled spall zone is pear shaped. The directly coupled spall zone size scales consistently with the cube root of the yield in the neighborhood of one megaton yield, and is dramatically reduced by hysteresis. The presence of a hard layer in one calculation had no effect on the maximum directly coupled spall depth on axis, but did increase the apex angle of the vertical cone within which directly coupled spall occurred.

< The calculations demonstrated conclusively that spall can be studied numerically using the STEALTH computer code. A more extensive numerical study should now be accomplished on a large mainframe computer, in which cratering and spall are investigated simultaneously. The purpose of such a study would be to evaluate the influence of early time source region details, and computational procedural details such as zone size, rezoning, and time step. *Report: → (Fig. 1)*

B

UNCLASSIFIED

SECURITY CLASSIFICATION OF THIS PAGE(When Data Entered)

# TABLE OF CONTENTS

<u>Section</u>	<u>Title</u>	<u>Page</u>
1.0	INTRODUCTION	1
2.0	DISCUSSION	3
	2.1 Problem Definition	3
	2.2 Computational Strategy	10
	2.3 Calculational Results	20
3.0	SUMMARY AND CONCLUSIONS	27
4.0	REFERENCES	28
	APPENDICES	
A.	Stress-Strain Relations	A-1
B.	Computer Plots	B-1



Accession For	
NTIS CRA&I	<input checked="" type="checkbox"/>
DTIC TAB	<input type="checkbox"/>
Unannounced	<input type="checkbox"/>
Justification	
By	
Distribution/	
Availability Codes	
Dist	Avail and/or Special
A1	

## LIST OF TABLES

<u>Number</u>	<u>Title</u>	<u>Page</u>
2.1	Experimental Spall Data from Near-Surface Detonations	6-7
2.2	Summary of Eight Directly Coupled Spall Calculations	11



## LIST OF FIGURES

<u>Number</u>	<u>Title</u>	<u>Page</u>
2.1	Surface Vertical Motion Above a Contained Nuclear Detonation in Rock--RANIER Event	4
2.2	Sketch of Typical Spall Regions and Nomenclature	8
2.3a	CRT Velocity Field at 1 Millisecond, Before Dezoning	13
2.3b	CRT Velocity Field at 1 Millisecond, After Dezoning	14
2.4	Yield Scaled Velocity Field Used for STEALTH to Define the Source Region for a 1 Mt Calculation	15
2.5	Peak Vertical Velocity on Axis from STEALTH Calculations 3, 4, and 5	16
2.6	STEALTH Grid and Velocity Waveform Target Points for 1 Mt Yield	18
2.7	Comparison of Scaled Directly Coupled Spall Zones for Non-Hysteretic Material Model	23
2.8	Comparison of Scaled Directly Coupled Spall Zones for Hysteretic Material Model	24
2.9	Comparison of Scaled Directly Coupled Spall Zones for Hysteretic Material Model with One and Two Layers	26

## 1.0 INTRODUCTION

This report documents the results of research accomplished under Air Force Office of Scientific Research contract F49620-83-C-0145, "The Influence of Specific Factors Affecting Spall in Explosively Loaded Soil," during the period 1 August 1983 through 31 January 1985. Applied Research Associates, Inc. has written two previous AFOSR reports on the subject of spall in soil (References 1 and 2). Spall in explosively loaded soil is caused by tensile failure, i.e., loss of particle to particle contact resulting from dynamic tensile strain. A spalled soil particle undergoes ballistic motion ( $-1g$  vertical acceleration) because the only significant vertical force acting on it is the downward force of gravity. Spall most frequently occurs at or near a free surface, but can also occur at a considerable distance from a free surface if the proper dynamic tensile strain conditions are present.

Reference 2 deals mainly with near surface soil spall due to airblast loading, but also attempts to infer the shape and size of the spall zone due to directly coupled energy from a near surface explosion, on the basis of very limited field test measurements. At the request of the Civil Engineering Research Division of the Air Force Weapons Laboratory (AFWL/NTE), the current effort focused on spall in soil due to directly coupled energy from a near surface explosion. The directly coupled spall problem has two parts. The first part concerns the shape and size of the spall zone due to directly coupled energy from a near surface explosion. The second part concerns the effect of directly coupled spall on the ground shock signal beyond the spall zone. The research reported herein focused on the first part; the shape and size of the directly coupled spall zone. Previous attempts to deduce the shape and size of the directly coupled spall zone from test data (Reference 2) have yielded inconclusive results, because of the lack of a sufficient number of vertical velocity measurements extending to an adequate depth directly beneath and at small horizontal ranges from the explosion. The second part of the directly coupled spall problem (far field waveform effects) was not addressed. This was because the computational mesh size required to adequately model the directly coupled spall zone material behavior was so small that the resulting

computational grid size was too small to yield ground shock waveforms at large distances beyond the directly coupled spall zone. Reflections from artificial but necessary computational grid boundaries were another reason for not calculating far field ground shock waveforms. The grid boundaries were far enough from the directly coupled spall zone not to have any effect on it, but not far enough from it to permit far field ground shock waveform calculations.

The specific factors affecting spall in soil due to directly coupled energy from a near surface explosion studied in the current effort were:

1. Weapon yield
2. Soil hysteresis
3. Site layering

Closed form solutions to two dimensional, intense stress wave propagation problems in soil, of the kind considered here, are all but impossible, and numerical methods must be used. The production calculations were done on ARA's HP1000 computer rather than on the AFWL CRAY, to maintain a reasonable schedule. This decision did impact the project technically, because the version of the STEALTH computer code which resides on the ARA HP1000 computer does not have a rezone/dezone option, due to limited storage capacity. This meant the calculations had to be accomplished in such a way as to avoid extreme distortion of the computational grid. This was accomplished by defining the explosion source region at a late enough time that it did not produce extreme distortion of the nearby soil grid, but at some possible sacrifice of accuracy.

Section 2.1 of this report defines the directly coupled spall problem in detail; Section 2.2 discusses the computational strategy employed; and Section 2.3 presents and analyzes the results of the computer calculations. Section 3 contains a summary of principal results and conclusions, and gives recommendations for future research on the subject of soil spall.

## 2.0 DISCUSSION

### 2.1 Problem Definition

Spall, in the sense of a tensile failure at the end of a bar subjected to an intense compression wave, or at the ground surface from an underground burst, or on the back side of a concrete wall impacted by fragments has long been well known. These cases all fall within Rinehart's classic definition of spall, i.e., "fracturing caused when a high intensity, transient stress wave reflects from a free surface" (Reference 3). For a normally incident compression wave in elastic, single phase materials, fairly simple relationships can be established to predict the initiation and location of spall fractures. These relationships depend upon:

1. The resistance of the material to fracture
2. The magnitude and shape of incoming stress waves

The classic case of surface spall in rock directly above a contained nuclear explosion occurred during the RANIER Event of Operation PLUMBBOB, a 1.7 Kt nuclear detonation 900 ft below the top of Ranier Mesa in Area 12 of the Nevada Test Site, on September 19, 1957 (References 4 and 5). It was RANIER ground shock data which prompted the still ongoing detailed study of explosion-induced ground shock spall (Reference 6). Figure 2.1 shows the surface vertical motion (recorded acceleration, and velocity obtained by integrating the recorded acceleration) which occurred directly above the RANIER detonation. Three distinct phases are evident in both the acceleration and velocity curves:

1. an initial upward motion
2. a prolonged  $-1g$  free-fall, or dwell, in this case of about 380 milliseconds duration, and
3. a sharp upward impact, or "rejoin"

Perret postulated that the above curves describe the motion of a rock mass given initial upward momentum by the upward-propagating compressive stress wave generated by the weapon detonation, then separated from the rock mass below by a distinct horizontal fracture, caused by the reflected tensile wave propagating downward from the free surface. The separated mass then undergoes "free" (ballistic) motion under the influence of gravity, until impacting the rock mass below. Glasstone and Dolan (Reference 7) describe spall from a shallow underground burst as follows:

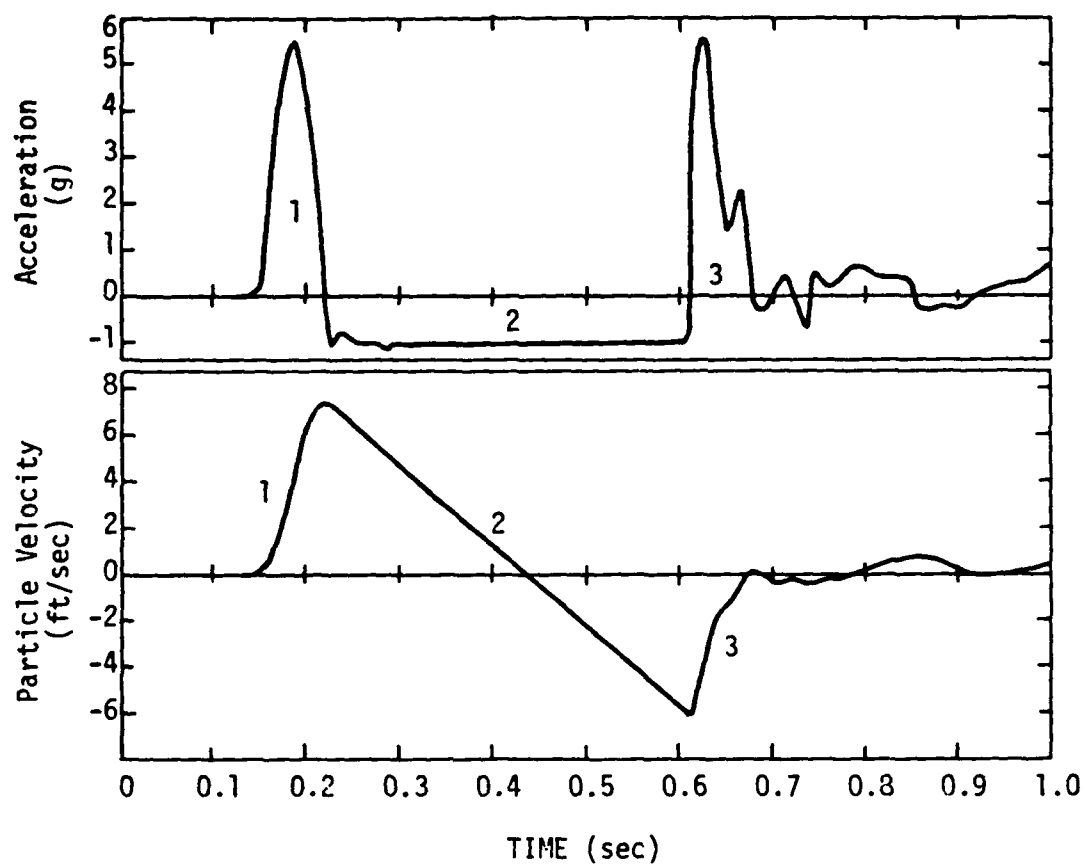


FIGURE 2.1

Surface Vertical Motion Above A Contained Nuclear Detonation In  
Rock - RANIER Event

When a nuclear weapon is exploded under the ground, a sphere of extremely hot, high-pressure gases, including vaporized weapon residues and rock, is formed. This is the equivalent of the fireball in an air or surface burst. The rapid expansion of the gas bubble initiates a ground shock wave which travels in all directions away from the burst point. When the upwardly directed shock (compression) wave reaches the earth's surface, it is reflected back as a rarefaction (or tension) wave. If the tension exceeds the tensile strength of the surface material, the upper layers of the ground will spall, i.e., split off into more-or-less horizontal layers. Then, as a result of the momentum imparted by the incident shock wave, these layers move upward at a speed which may be about 150 (or more) feet per second.

Spall-type ground motion has by no means been restricted to contained detonations in competent rock. Numerous ground shock records have been obtained in soil, for both contained and near-surface detonations, in which the vertical ground motion has exhibited all three of the characteristic spall features shown in Figure 2.1. Nor are such motions seen only near the ground surface. There are, however, significant differences in waveform detail between spall in soil and spall in rock.

Analyses of single and multiburst ground motion data from the MISERS BLUFF Phases I and II high explosive experiments showed that spall phenomena due to pore air expansion were strongly evident in the near surface ground motions immediately following local airblast effects. Measured ground motions from the PRE-MULTIBURST Phases I and II and PRE-HYBRID GUST high explosive experiments also contain similar spall features. The presence of spall probably accounts for much of the failure of empirical superposition procedures to correctly predict the frequency content and, in some cases, the peak time domain amplitude and time of occurrence of the large upward motion observed in ground motion records from multiburst explosions (References 8 and 9). Table 2.1 summarizes available experimental spall data from near surface U.S. chemical and nuclear explosions (Reference 2). The quantities  $R_s$  and  $z_s$  in Table 2.1 are defined in Figure 2.2 from Reference 2.

Spall is one of the less well understood and more troublesome mechanisms affecting explosive ground motion analysis and prediction. It is an important consideration for the geophysical community in attempting to differentiate between an explosion and an earthquake, or to describe an

TABLE 2.1  
EXPERIMENTAL SPALL DATA FROM NEAR-SURFACE DETONATIONS

Event	Charge* Configuration	Yield (tons)	Charge	Test Medium	D <sub>wt</sub> (m) **	D <sub>br</sub> (m) ***	R <sub>s</sub> (m) ****	Z <sub>s</sub> (m)
DISTANT PLAIN 6	STS	100	TNT	silty clay and sand layers	7.6	>60	>49	>5
PRAIRIE FLAT	STS	500	TNT	silty clay and sand layers	7.6	>60	>43	>5
DIAL PACK	STS	500	TNT	silty clay and sand layers	7.6	>60	>130	>6
FLAT TOP II	HBS	20	TNT	desert playa - layers of dry silt, clay and sand	>150	>150	>20 [38]*	>0.5
FLAT TOP III	HBS	20	TNT	desert playa - layers of dry silt, clay and sand	>150	>150	>20 [35]	>5
MIXED COMPANY III	STS	500	TNT	sandy-clayey silt over sandstone	>150	2.5	125 [121]	>9 [12]
PRE-MINE THROW IV-1	STS	0.52	Nitro- methane	desert playa - layers of dry silt, clay and sand	>150	>150	[25]	only shallow data
PRE-MINE THROW IV-2	STS	0.50	TNT	desert playa - layers of dry silt, clay and sand	>150	>150	[25]	
PRE-MINE THROW IV-3	STS	7.25	NM	desert playa - layers of dry silt, clay and sand	>150	>150	[61]	
PRE-MINE THROW IV-4	STS	0.52	NM	desert playa - layers of dry silt, clay and sand	>150	>150	[25]	
PRE-MINE THROW IV-5	HBS	0.50	TNT	desert playa - layers of dry silt, clay and sand	>150	>150	[25]	
PRE-MINE THROW IV-6	STS	102.4	NM	desert playa - layers of dry silt, clay and sand	>150	>150	[147]	
PRE-MINE THROW IV-7	HBS	0.13	TNT	desert playa - layers of dry silt, clay and sand	>150	>150	[16]	
PRE-DICE THROW II-1	STS	100	TNT	clayey silt and sand	2.1	>150	40	2
PRE-DICE THROW II-2	STC	120	ANFO	clayey silt and sand	2.1	>150	95	2
MIDDLE GUST 1	HBS	20	TNT	wet clay over shale	1.2	3.0	61	>6.1

TABLE 2.1  
(Continued)

EXPERIMENTAL SPALL DATA FROM NEAR-SURFACE DETONATIONS

Event	Charge Configuration	Yield (tons)	Charge	Test Medium	$D_{wt}$ (m)	$D_{br}$ (m)	$R_s$ (m)	$z_s$ (m)
MIDDLE GUST 2	4.8m HOB sphere	100	TNT	wet clay over shale	1.2	3.0	37	>6.1
MIDDLE GUST 3	STS	100	TNT	wet clay over shale	1.2	3.0	61	>6.1
MIDDLE GUST 4	STS	100	TNT	dry clay over shale	>150	8.5	?	?
MIDDLE GUST 5	HBS	20	TNT	dry clay over shale	>150	8.5	52	12.2
PHG I-06	Berm	0.042	C-4	layers of dry silt, sand and caliche	90	>150	10.5	2.3
PHG I-07	STS	0.128	TNT	layers of dry silt, sand and caliche	90	>150	18	2.8
PHG I-09	STS	0.128	TNT	layers of dry silt, sand and caliche	90	>150	15	2.4
MISERS BLUFF II-1	STC	120	ANFO	fine silt overlying gravelly sand	10.7	30.5	>200	4.0
PRE-MULTIPLE BURST 1	HBS	0.13	TNT	layers of dry silt, sand and caliche	90	>150	16	>.23
PRE-MULTIPLE BURST 2	STS	0.13	TNT	layers of dry silt, sand and caliche	90	>150	22	>1
PRE-MULTIPLE BURST 5	HOB sphere	0.13	TNT	layers of dry silt, sand and caliche	90	>150	18	>.23
MINERAL ROCK	STS	100	TNT	granite	>150	0	NS	NS
MINE ORE	STS	100	TNT	granite	>150	0	NS	NS
MINE UNDER	HOB	100	TNT	granite	>150	0	NS	NS
JANGLE U	DDB (5.18 m)	1200	Nuclear	fine sand mixed with gravel	>150	>150	110	>6.1

\*STS = surface tangent sphere

HBS = half buried sphere

STC = surface tangent cylinder with hemispherical cap

HOB = height of burst

DDB = depth of burst

\*\* $D_{wt}$  = depth to water table

\*\*\* $D_{br}$  = depth to bedrock

\*\*\*\* $R_s$  at  $z = 0.5$  m

\*[ $z_s$ ] was estimated from spall impact velocity data



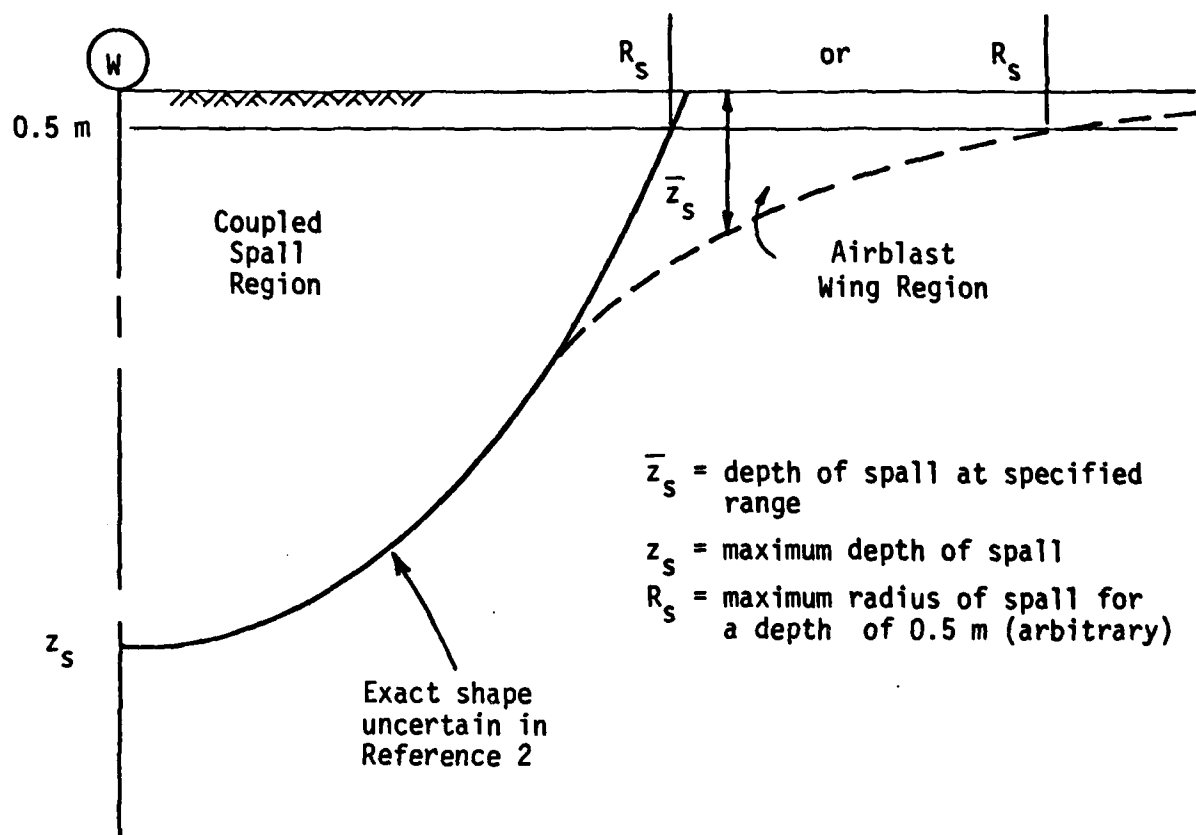


FIGURE 2.2  
 Sketch of Typical Spall Regions  
 and Nomenclature

explosion based on the characteristics of measured ground motion. It is equally as important for the weapon effects community in attempting to predict large yield effects from small yield tests, because late time spall behavior is gravity dominated, but gravity is usually neglected in explosive effects scaling. Uncertainties associated with spall arise in connection with nuclear detonation detection/discrimination, ground motion frequency analysis, yield scaling, HE/NE equivalence determination, and the use of superposition to calculate the resultant ground motion due to both airblast and directly transmitted ground shock, as well as due to multiple explosions.

For a near surface burst, the problem is much more complex than for classic one-dimensional spall. Near surface explosions generate various types of waves which are reflected and refracted in layered geologies, and cause complex wave interactions at the ground surface. In addition, both positive and negative local air pressures can augment or retard the spall process. Finally, geologic materials (particularly soils) are particulate, multiphase, highly nonlinear, inelastic, nonhomogeneous, and often anisotropic, particularly under the influence of tensile stress.

The definition of spall used here is a generalization of Rinehart's, recognizing that spall in soil is simply loss of particle contact (tensile failure) under dynamic loading, followed by sudden contact reestablishment (impact rejoin). Soil spall manifests itself as a prolonged  $-1g$  free fall, followed by a sharp upward impact. Auld (Reference 2) used the following criteria to determine from measured ground shock records whether spall had occurred:

1.  $-1g$  ( $-0.5$  to  $-2.0g$ ) vertical acceleration dwell ( $\geq 5$  ms), which is identifiable directly on a vertical acceleration record, or as the slope of a vertical velocity record
2. identifiable impulsive rejoin signal on both the vertical and horizontal acceleration records
3. rejoin amplitude ( $\geq 0.05$  m/s) observed on the vertical velocity record

These criteria are similar to those utilized by previous investigators, but with numerical values specified. They were used to assemble Table 2.1.

Auld, et al. (Reference 10) suggested that the zone of spalled material surrounding a near-surface explosion can be considered to consist

of two parts: a bowl-shaped volume of material, designated the "coupled spall region"; and a shallow extension of the basic spalled volume, designated the "negative airblast wing region." Figure 2.2 illustrates these two zones as they might occur from a typical near-surface detonation. Any of the possible spall mechanisms or a combination of these mechanisms may be responsible for the spall observed in the so called coupled spall region, e.g., direct waves, head waves, reflected waves, or surface waves.

The problem addressed herein is to define the shape and extent of the spall zone due to directly coupled energy from a near surface explosion in soil, as a function of explosion yield, soil hysteresis, and site layering. The approach was to perform eight two-dimensional, axially symmetric calculations, using the Lagrangian, explicit, dynamic finite difference computer code, STEALTH (Reference 11). The input to seven of the eight calculations was an initial kinetic energy source region distribution near the surface of a soil halfspace, plus a nuclear surface airblast pressure distribution. The input to the eighth calculation was an HE surface airblast pressure distribution only, which is the conventional representation of a near surface HE explosion. The results of the finite difference calculations are presented in the form of velocity-time waveforms and -lg dwell contours. Spall features, when present, have been identified from the velocity waveforms. The shape and extent of the directly coupled spall zone has been defined from the dwell contours. The identifiable properties of the directly coupled spall zone are then related to the loading, material and site property parameters. An important feature of the calculated results is that the directly coupled spall zone turned out to be pear shaped.

## 2.2 Computational Strategy

Eight STEALTH calculations were performed to define the shape and extent of the spall zone due to directly coupled energy from a near surface explosion in soil, as a function of explosion yield, soil hysteresis, and site layering. These calculations are summarized in Table 2.2. All eight calculations were two dimensional and axially symmetric, and employed a Lagrangian spatial grid and explicit time integration.

Attempts to initiate the calculations by depositing internal energy in a few of the rectangular zones surrounding the origin at time zero failed

TABLE 2.2  
SUMMARY OF EIGHT DIRECTLY COUPLED SPALL CALCULATIONS

<u>Run Number</u>	<u>Yield, MT</u>	<u>Equation of State</u>	<u>Layers</u>	<u>Surface Loading</u>
1	1.0	non-hysteretic	1	Speicher-Brode
2	2.0	non-hysteretic	1	Speicher-Brode
3	0.5	non-hysteretic	1	Speicher-Brode
4	1.0	hysteretic	1	Speicher-Brode
5	2.0	hysteretic	1	Speicher-Brode
6	0.5	hysteretic	1	Speicher-Brode
7	1.0	hysteretic	2	Speicher-Brode
8	1.0*	non-hysteretic	1	AMCLOAD (HE)

\*The conventional representation of a surface HE explosion involves airblast only. Therefore no initial kinetic energy source region was used in this calculation.

due to large grid distortion, which stopped the calculation. Rezoning was not possible with the version of STEALTH installed on the ARA HP1000 computer, due to limited storage capacity. In addition, the early time directly coupled spall zone for these calculations was also somewhat rectangular, which seemed suspicious. Consequently, the velocity field at 1 millisecond from a CRT 2 Kt alluvium cratering calculation, using the arbitrary Lagrangian/Eulerian code CRALE (Reference 12) was spatially and temporally yield cube root scaled and used to initiate Runs 1 through 7 in Table 2.2. The CRT calculation (designated R1) had been initiated using the state of the art Benchmark 3 (BM3) nuclear source developed by S<sup>3</sup>.

Figure 2.3a shows the velocity field in the CRT source region at 1 millisecond. To increase the calculational time step in CRALE, CRT performed a 2 to 1 dezoning of the entire grid at 1 millisecond. Figure 2.3b shows the velocity field in the CRT source region immediately after dezoning. The yield cube root scaled finite difference grid used in the ARA STEALTH calculations was superimposed on this modified CRALE grid. Figure 2.4 shows the yield cube root scaled velocity field used to start the ARA 1 Mt STEALTH calculations. The 1 Mt STEALTH grid was about the same size as the dezoned CRALE grid in the horizontal direction, and about 4/3 as large in the vertical direction. However, the STEALTH three point time domain central differencing scheme has a higher order truncation accuracy than does the CRALE two point time domain forward differencing scheme, and the higher order accuracy of STEALTH should have offset, at least in part, any detrimental effects the CRALE dezoning had on stress attenuation or spall zone shape and size. For a detailed discussion of the accuracy of the CRT 2 Kt alluvium cratering calculation, see Reference 13.

A plot of peak vertical velocity along the center axis for Runs 3, 4, and 5 is shown in Figure 2.5. This figure shows that the peak vertical velocity on axis varied with yield cube root scaled depth in a manner similar to that of empirical data for material with a comparable wavespeed analyzed by Cooper in Reference 14. Reference 13 shows that the rate of calculated peak stress attenuation is affected by source region waveform details, especially rise time, as well as by geometric and material behavior, and by numerical methods and zoning. The fact that the calculated peak stress attenuation data from the current STEALTH spall calculation, for

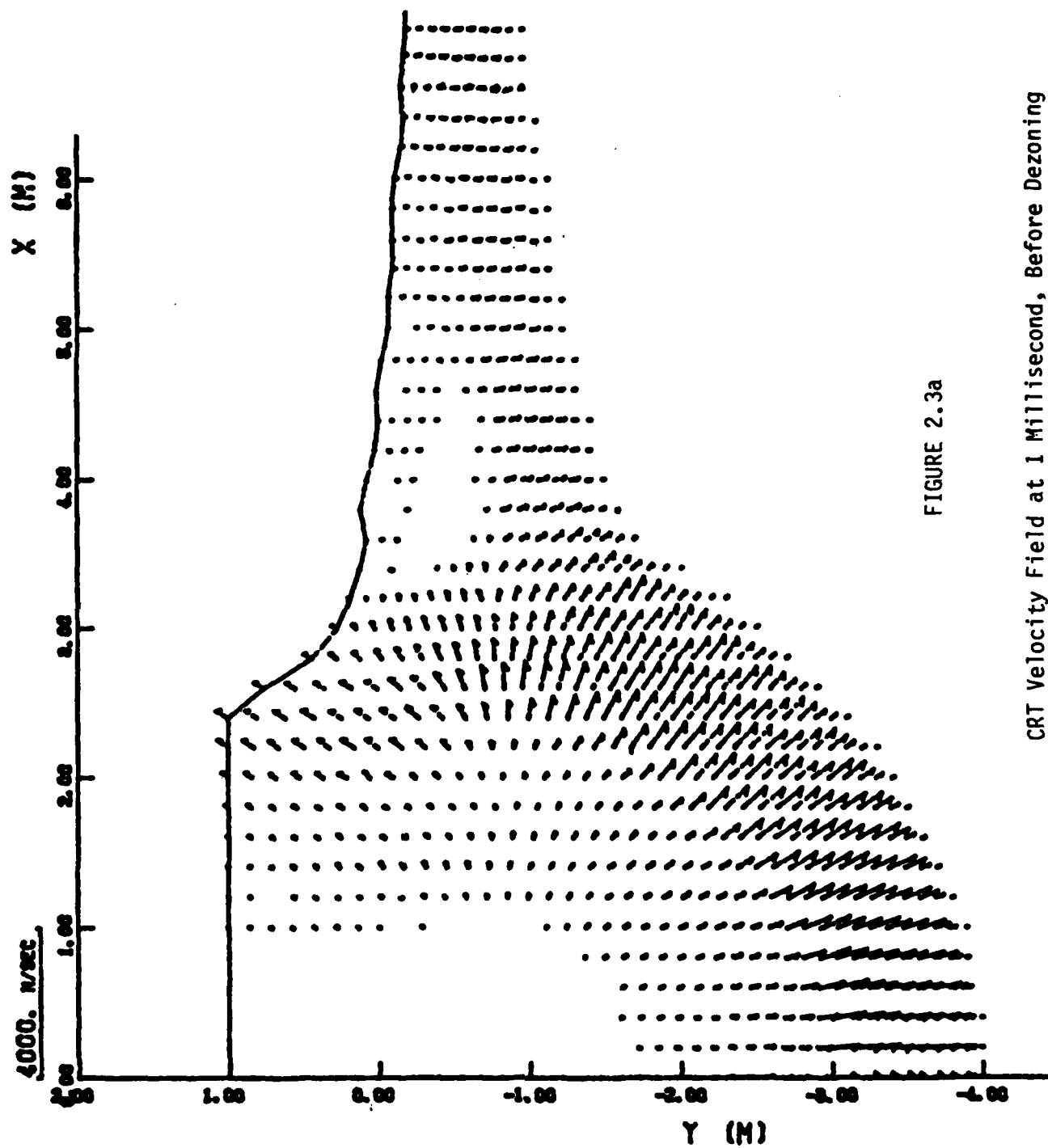


FIGURE 2.3a

CRT Velocity Field at 1 Millisecond, Before Dezoning

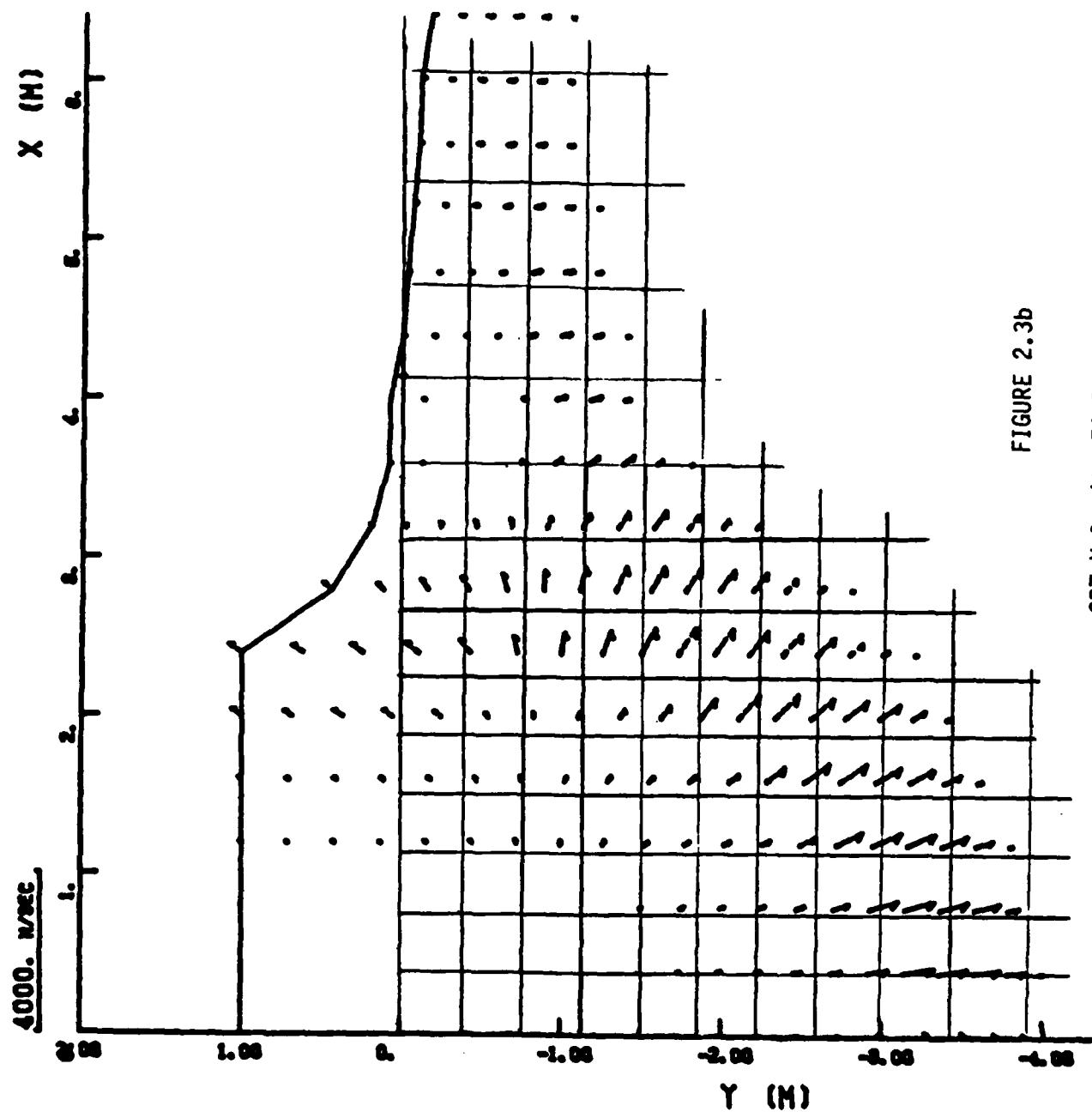


FIGURE 2.3b

CRT Velocity Field at 1 Millisecond , After Dezoning

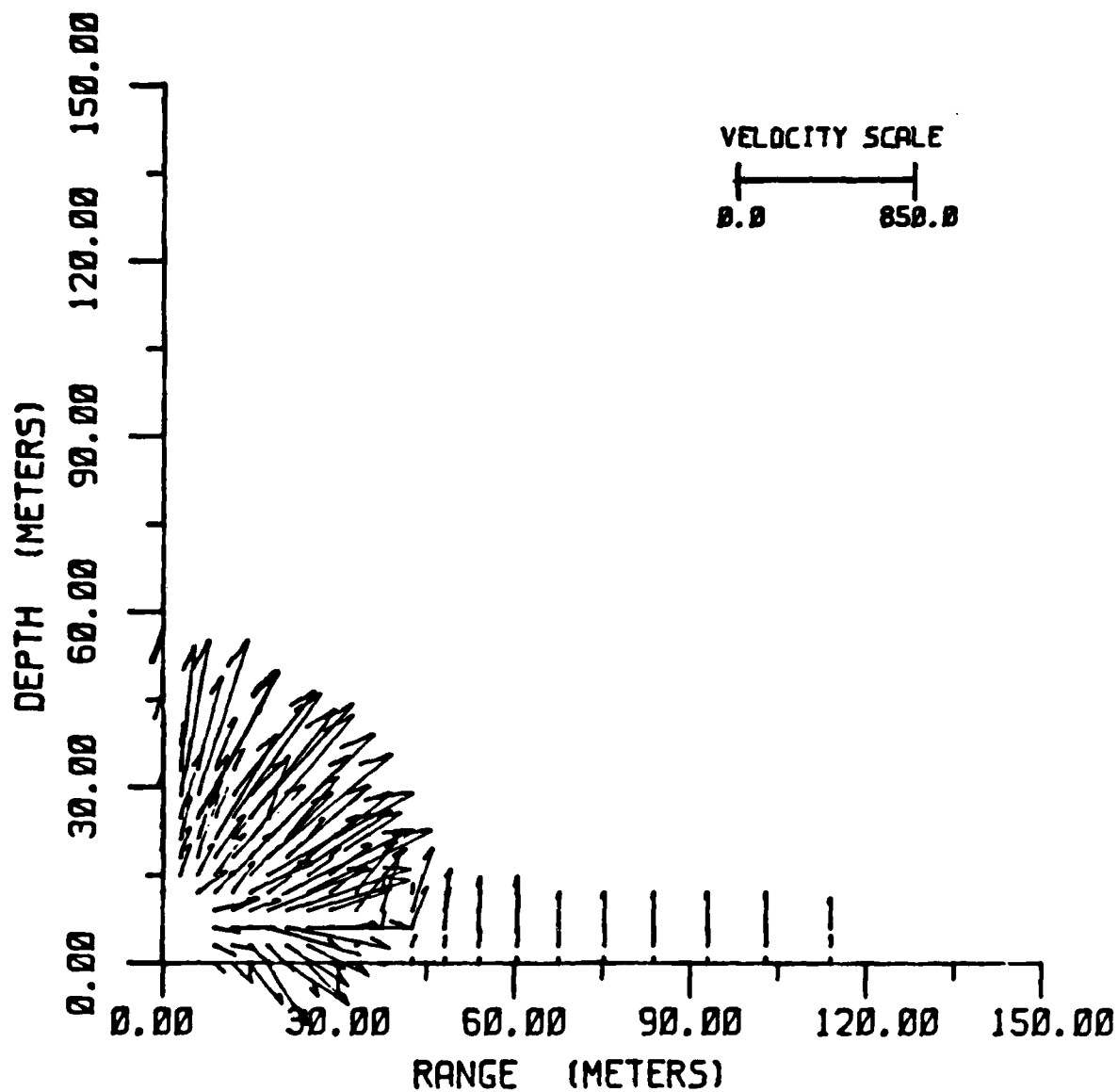


FIGURE 2.4

Yield Scaled Velocity Field Used in STEALTH to Define  
the Source Region for a 1 Mt Calculation



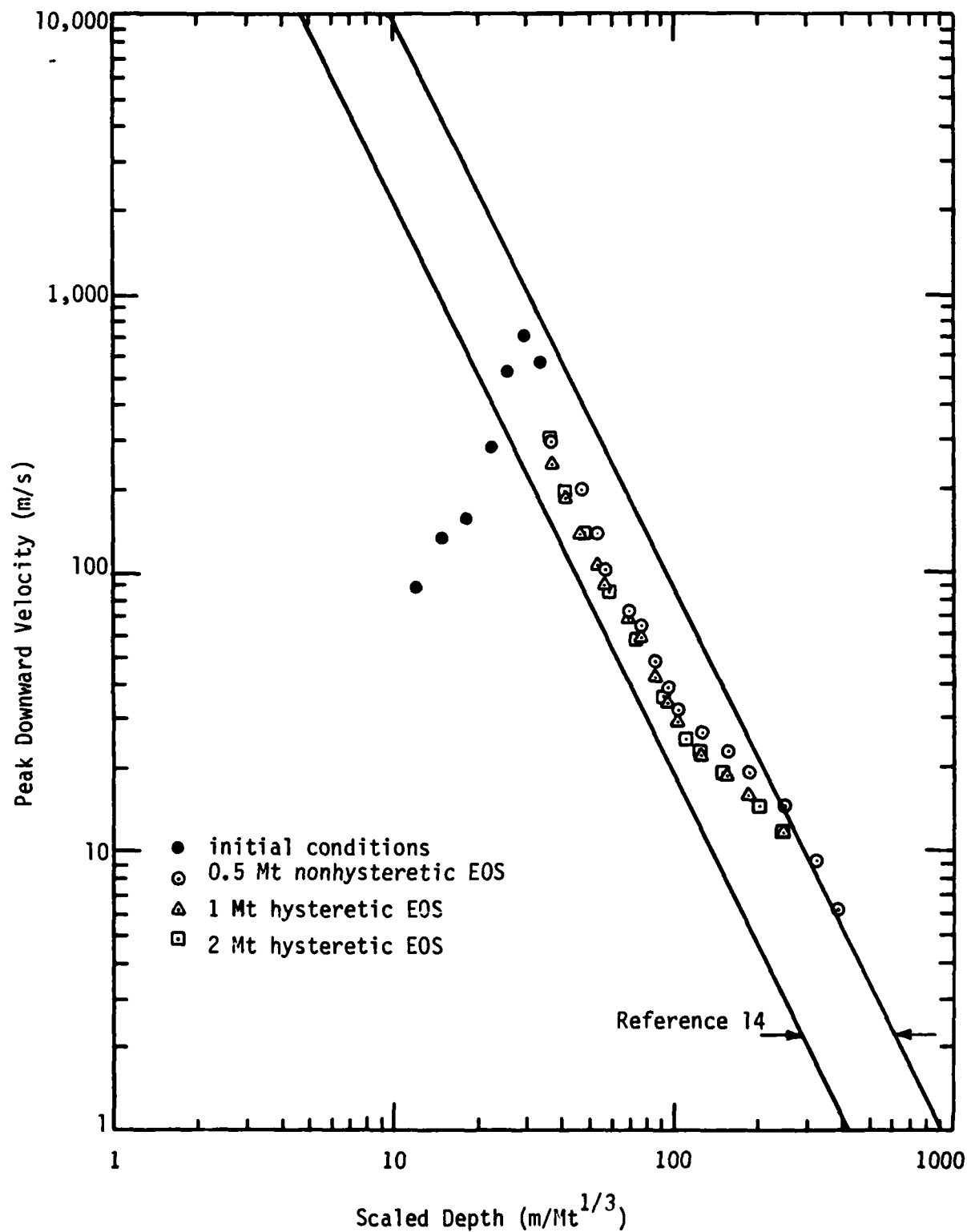


FIGURE 2.5

Peak Vertical Velocity on Axis from STEALTH  
Calculations 3, 4 and 5

both non-hysteretic and hysteretic material, compare favorably with Cooper's attenuation bounds from Reference 14 is cause to infer the reasonableness of CRT's R1 source region velocity field used to start the STEALTH spall calculations.

The finite difference grid for all eight runs consisted of 1600 nodes, arranged so that there were 39 zones in both the X and Y directions. A constant scaled zone size of  $3 \text{ meters/Mt}^{1/3}$  was used in both the X and Y directions for the first 15 meters of the grid. An initial zone size of  $3 \text{ meters/Mt}^{1/3}$  and a geometric progression of 1.09 were used to define the remainder of the grid. The finite difference grid and the locations of the velocity waveform target points are shown in Figure 2.6. The distance from the origin corresponding to selected grid lines is given below.

#### COMPUTATIONAL GRID LINE LOCATIONS

I, J	Z, $\text{m/Mt}^{1/3}$
1	0
2	3
3	6
4	9
5	12
6	15
7	18
10	28.72
15	54.06
20	93.06
25	153.06
30	245.37
35	387.41
40	605.95

I = range

J = depth

To simulate the nuclear surface airblast loading along the top boundary of the grid for Runs 1 through 7, a Speicher-Brode airblast

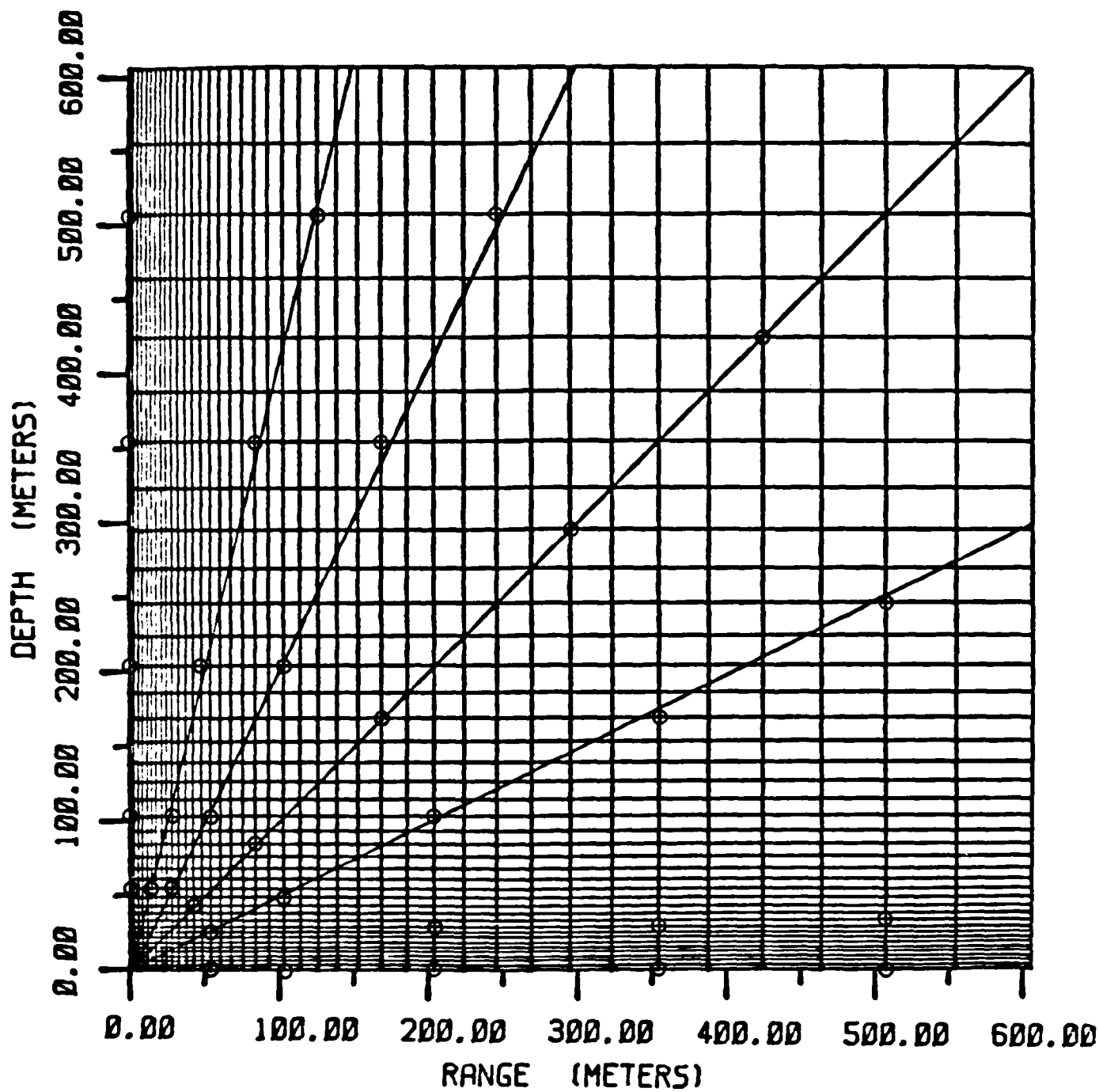


FIGURE 2.6

STEALTH Grid and Velocity Waveform Target Points  
for 1 Mt Yield

function (Reference 15) was used. Because all the calculations were run with axial symmetry, the Speicher-Brode airblast function was centered on the axis of symmetry and allowed to propagate outward to the edge of the grid.

To use STEALTH to study spall a soil stress-strain relation with low tensile stiffness was needed. Although spall is by nature a discontinuous phenomenon, it was convenient if not absolutely necessary to use a stress-strain relation which maintains continuity, i.e. which does not permit the material to fracture. This is because if two initially coincident material points separate they probably will not rejoin, but instead impact a zone boundary or another point. Describing this point or zone boundary impact process is beyond the capability of the STEALTH code. Consequently, displacements were assumed to be single valued, strains were related to displacement gradients, and stresses were expressed as functions of strains. The stress-strain equations are given in Appendix A.

The method used to determine if a particular node was in a state of spall was to check the vertical acceleration. If it was between  $-0.5$  and  $-2.0$  g's, the node was defined to be in a spalled state. This criterion was used to be consistent with the previously stated empirical spall criterion. The total and the longest continuous spall times were recorded for each node. Contours of longest continuous spall (dwell) time were plotted to define the shape and extent of the spall zone.

The first three calculations were run to determine the effect of explosion yield on the characteristics of the directly coupled spall zone. In all three calculations the axis of symmetry corresponded to the Y-axis, the radial and bottom boundaries were defined to be rigid, and the surface was defined as a pressure boundary. The Speicher-Brode airblast function was used to compute the surface airblast pressure as a function of time. The initial node spacing was determined from the 3 meter spacing used in the 1 Mt case, using cube root of yield scaling. The spacing in the 2.0 Mt calculation was 3.8 meters, and for the 0.5 Mt case the spacing was 2.4 meters. The magnitude of the velocity field used to define the initial kinetic energy was not changed; only the spatial placement of the velocity vectors was affected. Time was also scaled. The reason for using such a small yield range (0.5-2.0 Mt) was that gravity was kept constant, independent of yield.

It was therefore anticipated that yield cube root scaling would not strictly apply, and the purpose of the relatively small yield variation was to see what yield scaling law did apply. As it turned out, the yield scaling law which applies for the yield employed is approximately cube root, and limited computer resources prevented widening the yield range.

The fourth, fifth and sixth calculations were completed using the same initial velocity field, node spacing, yields, and boundary conditions as the first three calculations. The only difference between these and the first three calculations was the material model used. In these calculations the original material model was modified to allow for hysteresis.

The seventh calculation was performed to see what influence a material layer interface would have on the directly coupled spall zone. A second layer was introduced at a depth of 223.60 meters ( $J = 29$ ). The hysteretic material model was used in both layers. In the upper layer the material model was the same as the model used in Runs 4, 5, and 6. The second layer consisted of the same material model, except with coefficients four times as large as those in the first layer. The result of this change was to increase the material wave speed from 2000 meters/second in the first layer to 4000 meters/second in the second layer. The material density and Poisson's ratio were kept the same for both layers.

The final calculation was a 1 Mt HE, 1 layer calculation using the simple non-hysteretic material model. The boundary conditions and node spacing were the same as in the previous 1 Mt calculations. The surface airblast loading pressure was computed using the CRALE HE subroutine AMCLOAD (an empirical fit to MIDDLE GUST III airblast records) (Reference 16). The purpose of this run was to see if the nature of spall due to a near surface HE explosion differs substantially from that due to a near surface nuclear explosion of the same yield. Since the conventional representation of a surface HE explosion involves airblast only, the scaled CRT R1 initial velocity vector field was not used in this calculation.

### 2.3 Calculational Results

The criterion used to determine whether a node was in a state of spall was whether the vertical acceleration was between  $-0.5 \text{ g's}$  and  $2.0 \text{ g's}$ . As a means of graphically displaying the length of time each node was in spall,

a letter of the alphabet was used to represent each 0.010 second dwell interval as follows:

<u>Letter</u>	<u>Dwell Time, Sec</u>
"blank"	less than 0.010
A	0.010 to 0.020
B	0.020 to 0.030
C	0.030 to 0.040
D	0.040 to 0.050
E	0.050 to 0.060
F	0.060 to 0.070
G	0.070 to 0.080
H	0.080 to 0.090
I	0.090 to 0.100
J	greater than 0.100

These identifiers are plotted at the node locations, and the 10 msec dwell contour drawn by eye. The region enclosed by the 10 msec dwell contour is defined as the directly coupled spall zone.

Vertical velocity waveforms were also examined along a variety of radials from the origin. In the velocity waveforms a -1g acceleration is represented by a linear section in the waveform having a slope of  $-9.81 \text{ m/sec}^2$ .

The results from all eight calculations are presented in Appendix B. Note that Y is positive downward in all plots in Appendix B. Because of noise resulting from large zone aspect ratios, only results from within the first 30 I and J grid lines were examined. Appendix B is divided into four parts. The results for the non-hysteretic material model are presented on pages B-2 through B-15. The results for the hysteretic material model and one material layer are presented on pages B-16 through B-29. A comparison of the results for the one megaton, non-hysteretic material model with one layer (Run 1), the one megaton, hysteretic material model with one layer (Run 4), and the the one megaton, hysteretic material model with two layers (Run 7), is presented on pages B-30 through B-42. Pages B-43 and B-44 shows selected results from the one megaton HE (AMCLOAD loading) calculation (Run 8).

The objective of these calculations was to evaluate the influence of 1) yield, 2) hysteresis, and 3) layering on directly coupled spall in a numerical calculation. The influence of each of these variables on the shape and size of the spall zone due to directly coupled energy from a near surface explosion in soil is addressed below.

1. Yield--To examine the effect yield has on the directly coupled spall zone a comparison of the results from the one megaton, two megaton, and half megaton calculations was made. Figure 2.7 shows the scaled directly coupled spall zones resulting from calculations involving the non-hysteretic material model (Runs 1-3). The scaled directly coupled spall zones in non-hysteretic material for all three yields are consistent in size, but pear shaped, rather than bowl shaped. These pear shaped zones are similar in shape to that of pressure bulbs (contours of maximum principal stress) due to surface pressure applied over a circular area on an elastic half space. Since a near surface explosion also exerts intense pressure over a more or less circular area, the pear shaped configuration of the directly coupled spall zones appears reasonable, even though it departs from the bowl shaped configuration characteristic of explosive craters. The maximum directly coupled spall depth, which occurs on axis, is between 210 and 225  $m/(Mt)^{1/3}$ . Except for a lip which roughly coincides with the crater region, the directly coupled spall zone in non-hysteretic material lies within a 60 degree cone with its apex at the origin. (The cone directrices make a 30 degree angle with the grid centerline.) Figure 2.8 shows the scaled directly coupled spall zones resulting from calculations involving the hysteretic material model (Runs 4-6). The directly coupled spall zones in hysteretic material, for all three yields, are also consistent in size, and pear shaped. The maximum directly coupled spall depth, which occurs on axis, is between 165 and 190  $m/(Mt)^{1/3}$ . There is no directly coupled spall zone lip, as there was for the non-hysteretic material, and the directly coupled spall zone in hysteretic material lies within a 25 degree cone with its apex at the origin.

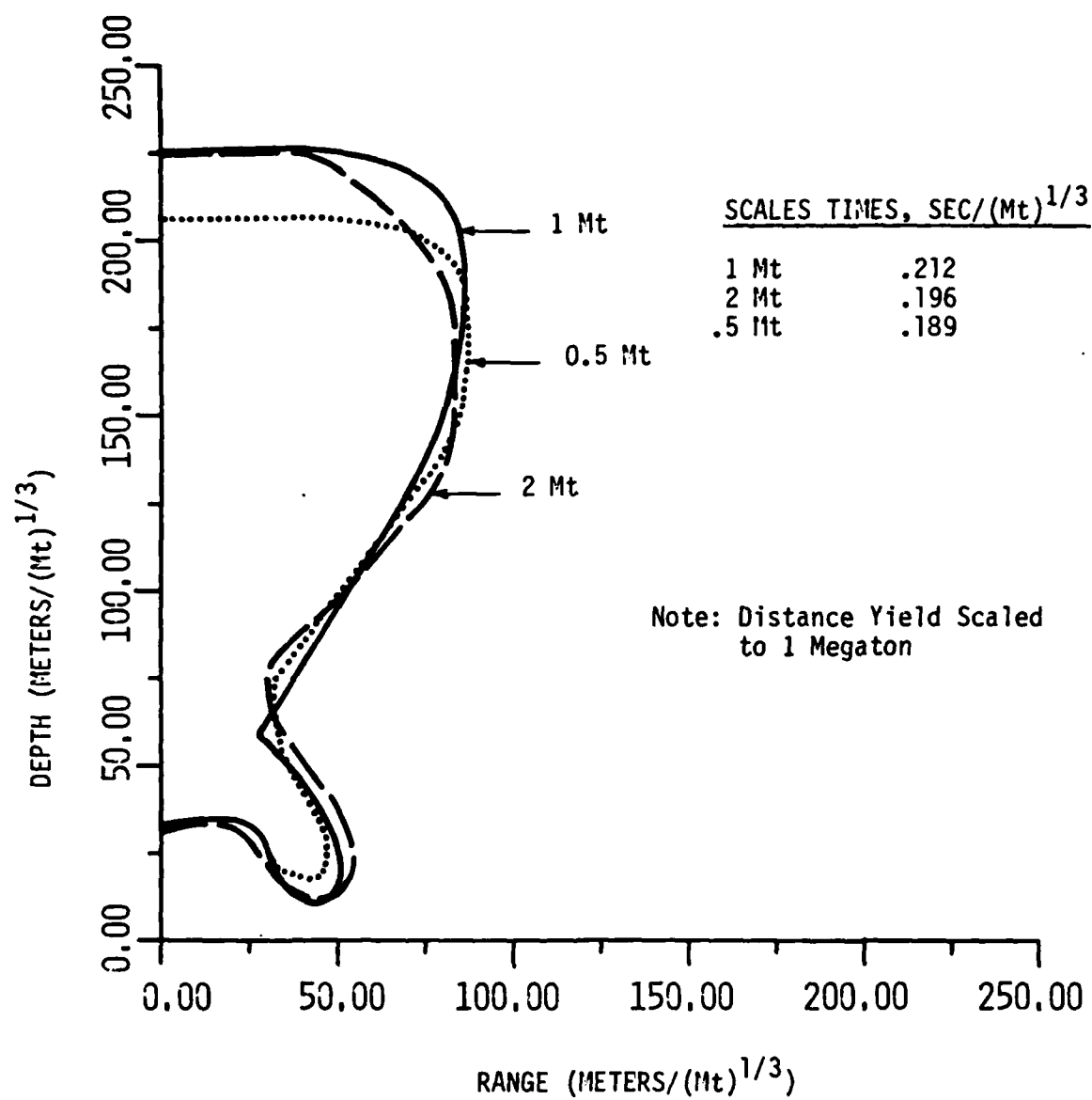


FIGURE 2.7

Comparison of Scaled Directly Coupled Spall Zones for Non-Hysteretic Material Model



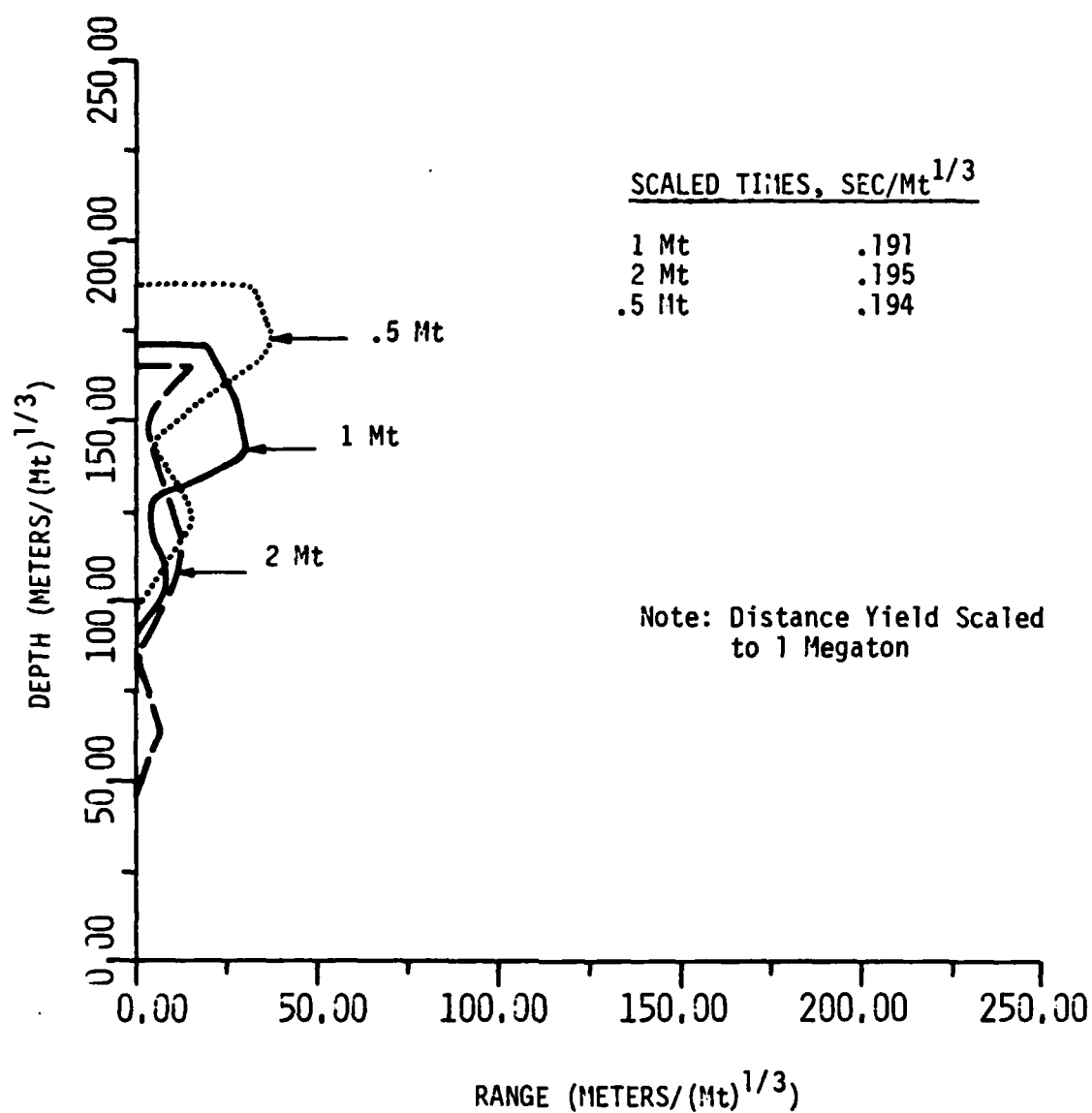


FIGURE 2.8

Comparison of Scaled Directly Coupled Spall Zones for Hysteretic Material Model

2. Hysteresis--The presence of hysteresis dramatically and consistently reduces the size of the directly coupled spall zone, as Figures 2.7 and 2.8 show. This suggests that a principal mechanism of spall due to directly coupled energy from a near surface explosion is tensile failure caused by late time release of stored strain energy.
3. Layering--Figure 2.9 shows that the second, stiffer layer at 223.60 meter depth had no effect on the depth of directly coupled spall on axis, in comparison with that for the hysteretic case with only one layer, but did widen the angle of the cone within which directly coupled spall occurred from 25 degrees to about 90 degrees.

The data on pages B-43 and B-44 show spall due to HE airblast only. The zone in which directly coupled spall occurred in Runs 1 through 7 shows no spall in Run 8, indicating that the principal spall agent in Runs 1 through 7 was directly coupled energy, as intended. Since directly coupled spall does occur for near surface HE explosions, however, the lack of directly coupled spall in Run 8 also indicates the need for a better theoretical representation of a near surface HE explosion.

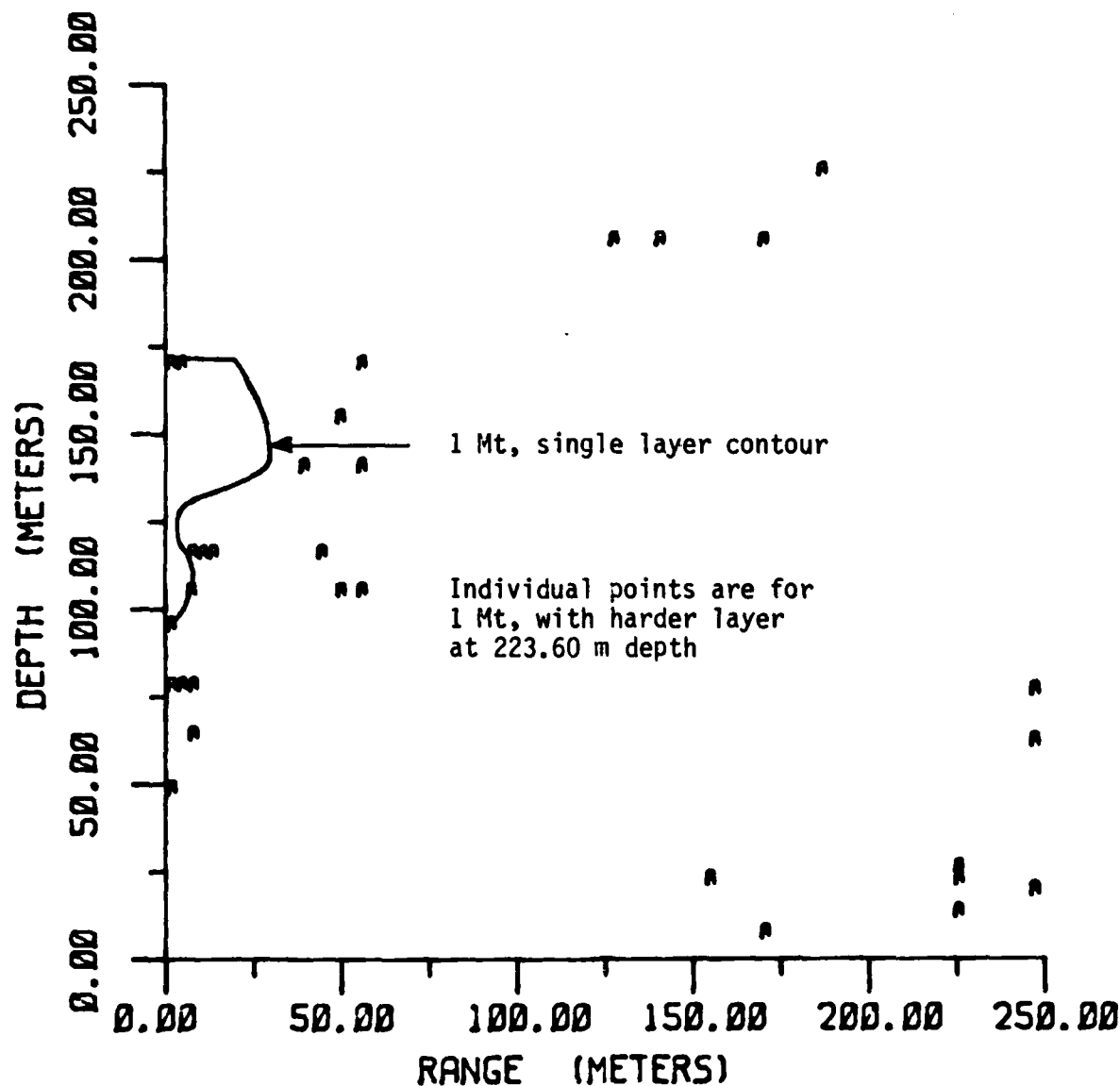


FIGURE 2.9

Comparison of Scaled Directly Coupled Spall Zones  
For Hysteretic Material Model With One and Two Layers

### 3.0 SUMMARY AND CONCLUSIONS

The purpose of this investigation was to evaluate the influence of explosion yield, soil hysteresis, and site layering on the shape and size of the spall zone due to directly coupled energy from a near surface explosion in soil. The investigation was done numerically on Applied Research Associates' HP1000 computer, using the Lagrangian, explicit dynamic finite difference computer code, STEALTH. The most important result is the observation that the computed directly coupled spall zone is pear shaped. The directly coupled spall zone size scales consistently with the cube root of the yield in the neighborhood of one megaton yield, and is dramatically reduced by hysteresis. The presence of a hard layer in one calculation had no effect on the maximum directly coupled spall depth on axis but did increase the apex angle of the vertical cone within which directly coupled spall occurred.

The calculations demonstrated conclusively that spall can be studied numerically using the STEALTH computer code. A more extensive numerical study should now be accomplished on a large mainframe computer, in which cratering and spall are investigated simultaneously. The purpose of such a study would be to evaluate the influence of early time source region details, and computational procedural details such as zone size, rezoning, and time step. When the shape and size of the spall zone due to directly coupled energy from a near surface explosion in soil has been well defined, the same source can then be used with confidence to study spall effects on ground shock waveforms well beyond the directly coupled spall zone.

#### 4.0 REFERENCES

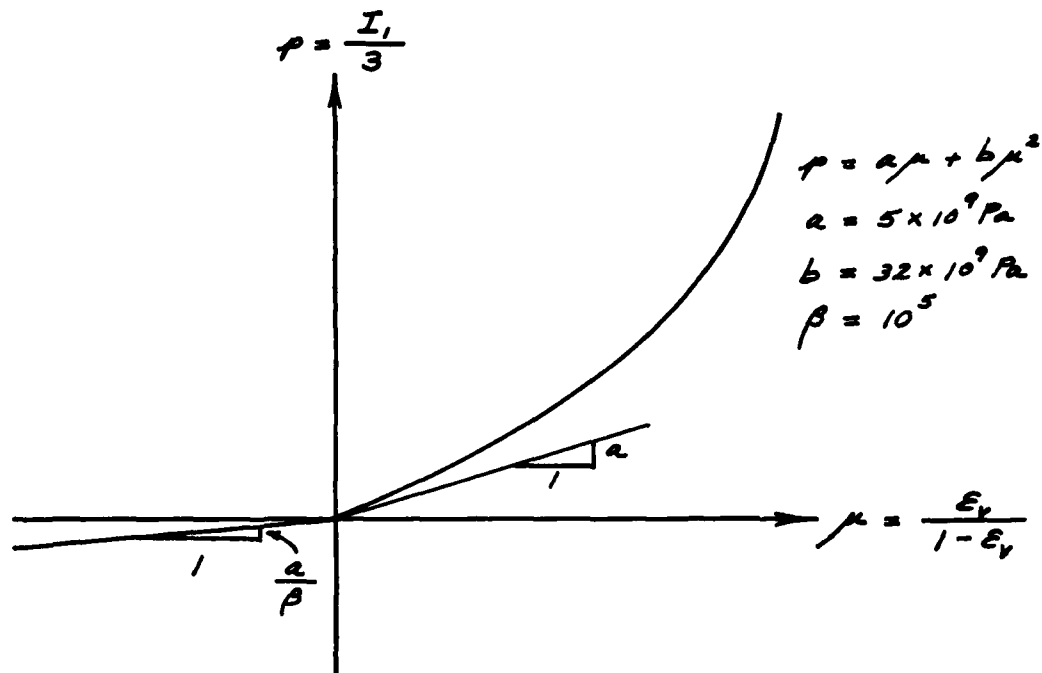
1. Merkle, D.H., "Basic Mechanisms of Spall From Near-Surface Explosions," Applied Research Associates report to the Air Force Office of Scientific Research, AFOSR-TR-80-1379, ADA 093882, 30 November 1980.
2. Merkle, D.H., H.E. Auld, W.C. Dass, J.C. Partch and P.T. Dzwilewski, "Effect of Spall on the Characteristics of Explosive Ground Motion," Applied Research Associates report to the Air Force Office of Scientific Research, AFOSR-TR-83-0060, ADA 125592, 10 September 1982.
3. Rinehart, J.S., STRESS TRANSIENTS IN SOLIDS, Hyperdynamics, Santa Fe, New Mexico, 1975.
4. Perret, W.R., "Subsurface Motion from a Contained Underground Detonation," WT-1529, Sandia Corporation, May 1961.
5. Perret, W.R., "Free-field and Surface Motion from a Nuclear Explosion in Alluvium: MERLIN Event," Sandia Lab Report SC-RR-69-334, November 1971.
6. Perret, W.R., "Surface Motion Near Underground Nuclear Explosion in Desert Alluvium," Operation NOUGAT I, Area 3, Nevada Test Site, SAND 77-1435, Sandia Laboratories, May 1978.
7. Glasstone, S. and P.J. Dolan, THE EFFECTS OF NUCLEAR WEAPONS, Third Edition, U.S. Government Printing Office, 1977.
8. Phillips, J.S. and J.L. Bratton, "MISERS BLUFF Phase I, Ground Shock Analysis of the Multiple Burst Experiments," CNSC IR 78-002 to Defense Nuclear Agency, 15 August 1978.
9. CNSC, "Preliminary Ground Shock Data Analysis of MISERS BLUFF Phase II," CNSC Progress Report No. 16, 9 January 1979.
10. Auld, H.E., D.M. Bradley, R. Brown, S.E. Blouin and B.W. Stump, "Data Analysis of the PRE-HYBRID GUST (PHG) Test Series," Applied Research Associates report to the Defense Nuclear Agency (submitted 16 August 1981; in review).
11. Hofmann, R., "STEALTH, a Lagrange Explicit Finite-Difference Code for Solids, Structural and Thermo-hydraulic Analysis," EPRI NP-176-1, Electric Power Research Institute, Palo Alto, CA, 1978.
12. Koik, V.E., letter to N. Lipner (TRW), 2 KT Calculation, Stress Plots From 25 KSI to 200 KSI Peak Overpressure, CRT N4387, 2 February 1984.
13. Dzwilewski, P.T., and J-Y Liu, "Fidelity of Ground Shock Calculations," Applied Research Associates report to the Defense Nuclear Agency, January 1985.

14. Cooper, H.F., "Empirical Studies of Ground Shock and Strong Motions in Rock," RDA report to the Defense Nuclear Agency, RDA-TR-3601-002, DNA 3245F, October 1973.
15. Schuster, S.H., and J.S. Macales, "Note on the Airblast Boundary Pressure Function Used in Calculations of Nuclear Surface Burst Problems," CRT-TN-3540-1, California Research and Technology, Inc., Chatsworth, California, March 1983.
16. Schuster, S.H., personal communication to P.T. Dzwilewski, California Research and Technology, Woodland Hills, CA, 5 May 1980.

APPENDIX A  
STRESS-STRAIN RELATIONS

## Non-Hysteretic Stress-Strain Relations

A simple tension-sensitive stress-strain relation in which one bulk modulus is used for compression and another smaller bulk modulus is used in tension was used as the material model. A constant material density and Poisson's ratio were used in both compression and tension.



$$\rho = 1760 \text{ KG/M}^3 \quad [1]$$

$$p = a\mu + b\mu^2 \quad (\mu \geq 0) \quad [2]$$

$$= \frac{a}{\beta}\mu \quad (\mu < 0) \quad [3]$$

$$\frac{dp}{d\mu} = B = a + 2b\mu \quad (\mu \geq 0) \quad [4]$$

$$= \frac{a}{\beta} \quad (\mu < 0) \quad [5]$$

$$\frac{dp}{d\epsilon_v} = K = \frac{B}{(1 - \epsilon_v)^2} \quad [6]$$

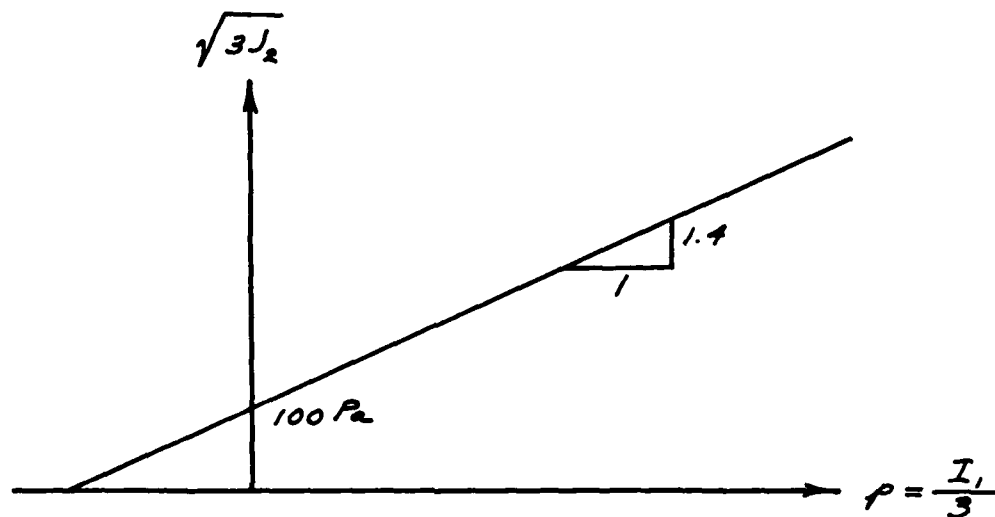


$$\nu = \frac{1}{3} \quad [7]$$

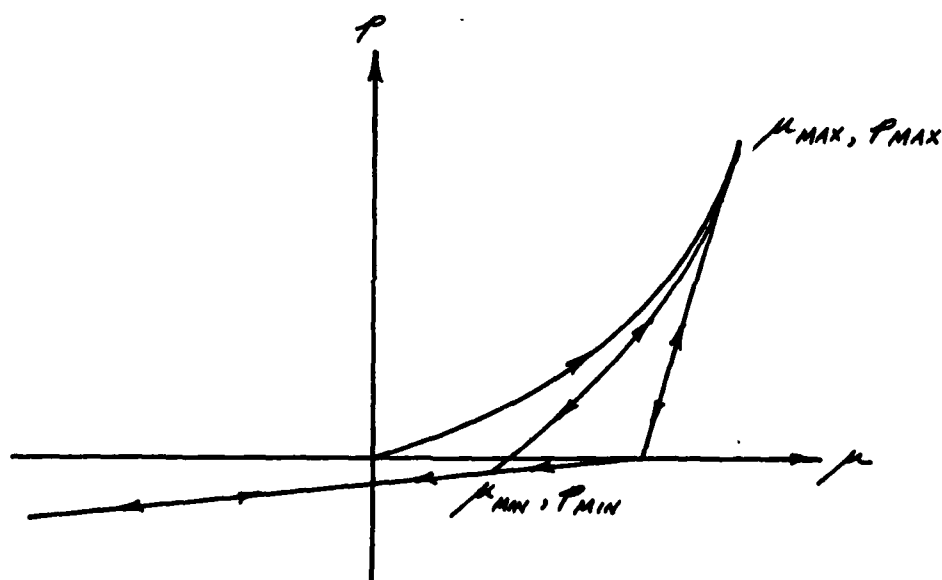
The Shear Modulus is

$$2G = \frac{3K(1-2\nu)}{1+\nu} \quad [8]$$

The Shear Failure surface is shown below. Shear failure surface violations are corrected at constant  $p$ .



### Hysteretic Stress-Strain Relations



$$\rho = 1760 \text{ KG/M}^3 \quad [9]$$

$$\mu \geq \mu_{\max}$$

$$p = a\mu + b\mu^2 \quad [10]$$

$$\mu_{\max} = \mu \quad [11]$$

$$p_{\max} = p \quad [12]$$

$$\mu_{\min} = \mu_{\max} - \frac{p_{\max}}{a+2b\mu_{\max}} \quad [13]$$

$$p_{\min} = 0 \quad [14]$$

$$\mu_{\min} < \mu < \mu_{\max} \text{ and } p_{\min} = 0$$

$$p = (a + 2b\mu_{\max})(\mu - \mu_{\min}) \quad [15]$$

$$\mu_{\min} < \mu < \mu_{\max} \text{ and } p_{\min} < 0$$

$$p = p_{\min} + c(\mu - \mu_{\min}) + d(\mu - \mu_{\min})^2 \quad [16]$$

where

$$d = \frac{(a+2b\mu_{\max})(\mu_{\max}-\mu_{\min}) - (p_{\max}-p_{\min})}{(\mu_{\max}-\mu_{\min})^2} \quad [17]$$

$$c = \frac{2(p_{\max}-p_{\min})}{\mu_{\max}-\mu_{\min}} - (a+2b\mu_{\max}) \quad [18]$$

$$0 \leq \mu < \mu_{\min}$$

$$p = p_{\min} + \frac{a}{8}(\mu - \mu_{\min}) \quad [19]$$

$$\mu_{min} = \mu \quad [20]$$

$$p_{min} = p \quad [21]$$

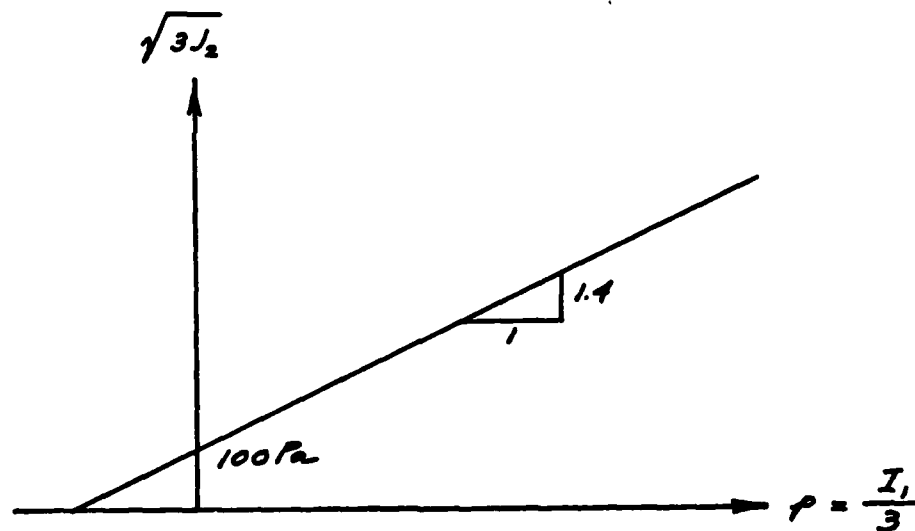
$$\mu < 0$$

$$p = p_{min} + \frac{a}{B}\mu \quad [22]$$

The shear modulus is

$$2G = \frac{3K(1-2\nu)}{1+\nu} \quad [8]$$

The shear failure surface is shown below. Shear failure surface violations are corrected at constant  $p$ .



#### Proof of Equations [17] and [18]

The basic equation is

$$p - p_{min} = c(\mu - \mu_{min}) + d(\mu - \mu_{min})^2 \quad [23]$$

and the two conditions determining the constants c and d are

$$P_{\max} - P_{\min} = c(\mu_{\max} - \mu_{\min}) + d(\mu_{\max} - \mu_{\min})^2 \quad [24]$$

$$c + 2d(\mu_{\max} - \mu_{\min}) = a + 2b\mu_{\max} \quad [25]$$

If we set

$$P_{\max} - P_{\min} = P \quad [26]$$

$$a + 2b\mu_{\max} = S \quad [27]$$

$$\mu_{\max} - \mu_{\min} = X \quad [28]$$

Then Equations [24] and [25] can be written in the form

$$Xc + X^2d = P \quad [29]$$

$$c + 2Xd = S \quad [30]$$

or

$$c + Xd = \frac{P}{X} \quad [31]$$

$$c + 2Xd = S \quad [32]$$

Subtracting Equation [31] from Equation [32] yields

$$Xd = S - \frac{P}{X} = \frac{SX - P}{X}$$

or

$$d = \frac{SX - P}{X^2} \quad [33]$$

and Equation [32] then yields

$$c = S - 2Xd = S - \frac{2(SX - P)}{X} = \frac{2P}{X} - S \quad [34]$$

The slopes of the various branches of the p-μ curve are as follows:

virgin compression:

$$B = a + 2b\mu_{\max} \quad [35]$$

straight line unloading-reloading:

$$B = a + 2b\mu_{\max} \quad [35]$$

$$\frac{\text{tension:}}{B} = \frac{a}{B} \quad [36]$$

parabolic unloading/reloading:

$$B = c + 2d(\mu - \mu_{\min}) \quad [37]$$

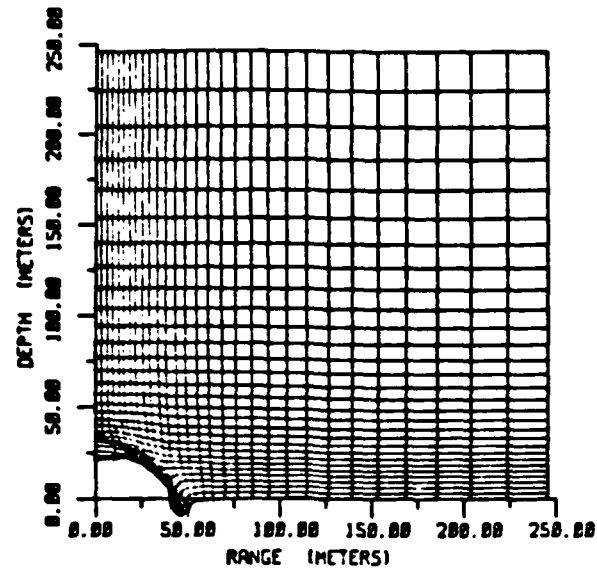
The bulk modulus is

$$\frac{dp}{d\varepsilon_v} = K = \frac{B}{(1 - \varepsilon_v)^2} \quad [6]$$

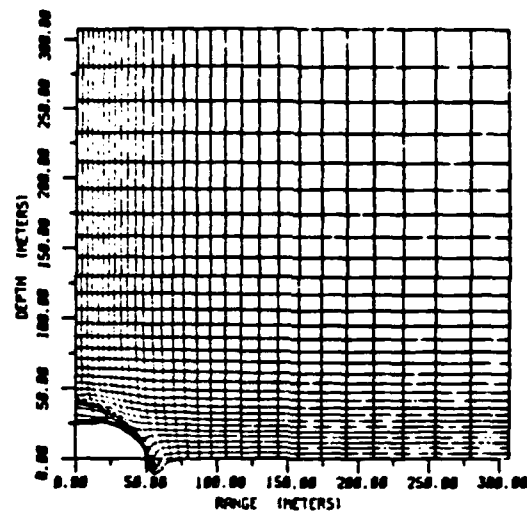
Poisson's ratio is an assumed constant.

$$\nu = \frac{1}{3} \quad [7]$$

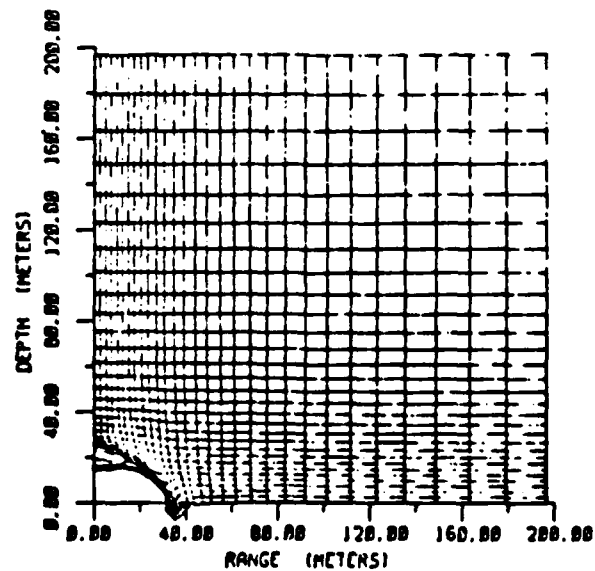
APPENDIX B  
COMPUTER PLOTS



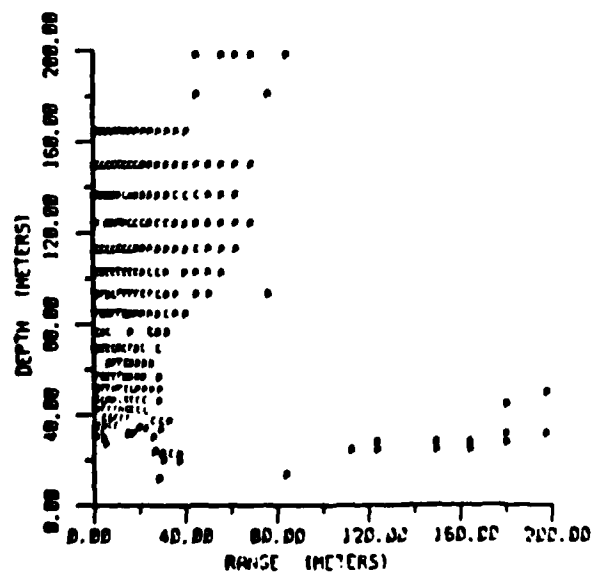
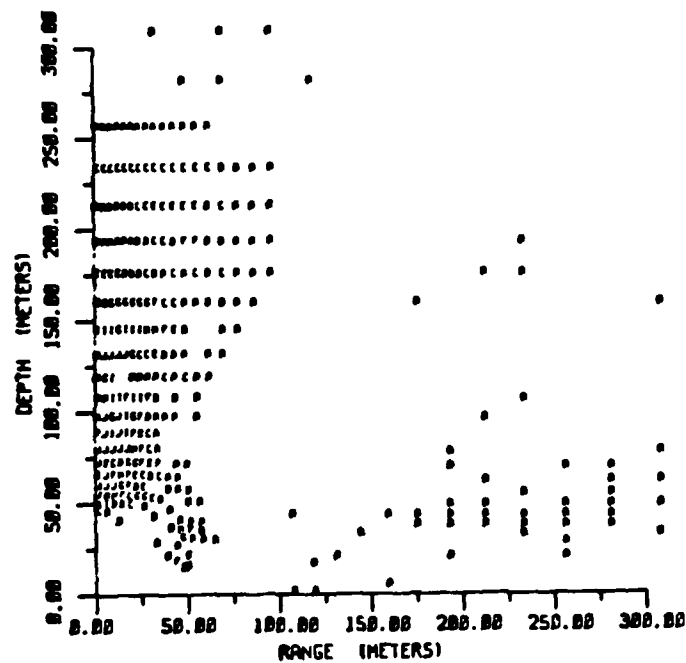
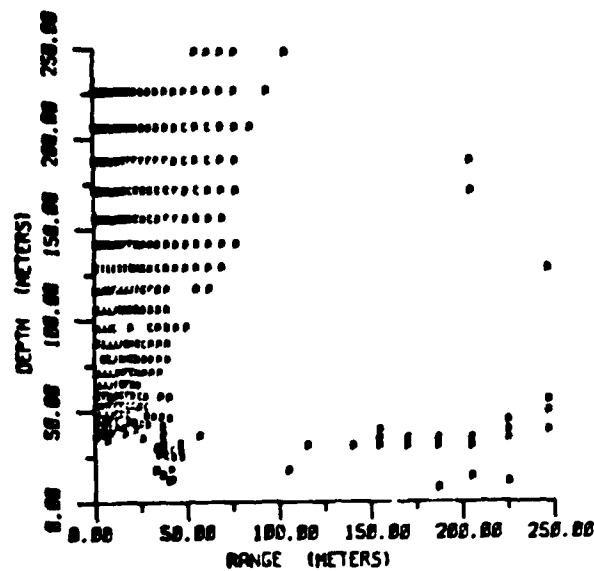
1MT  
CYCLE NUMBER 999  
TIME .21255



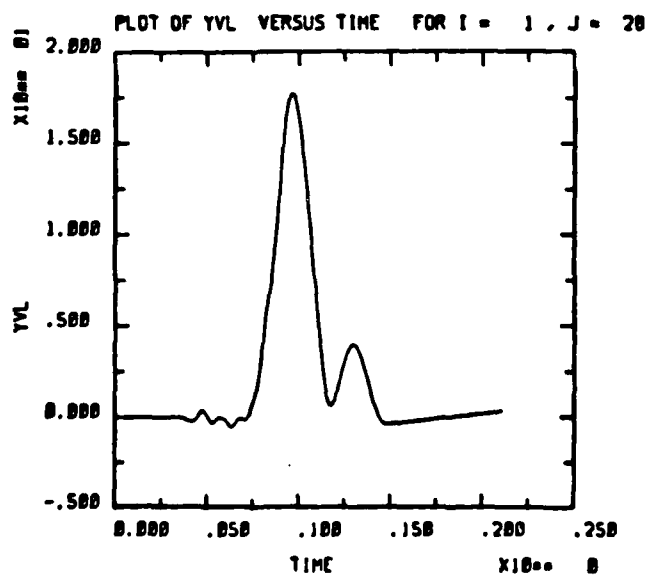
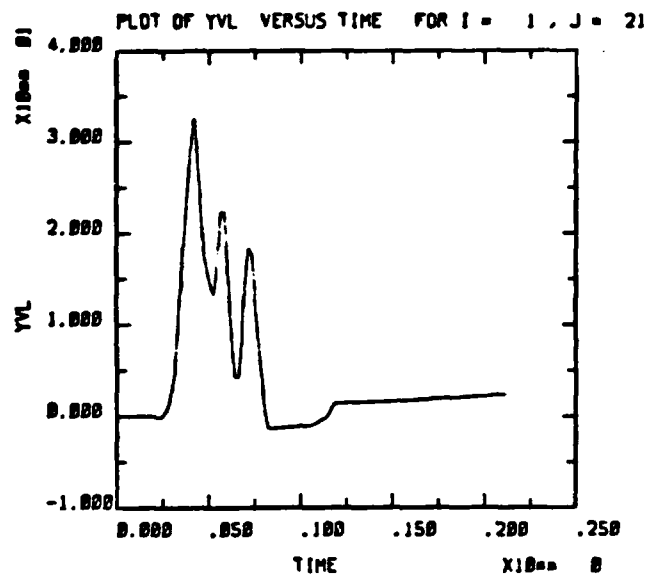
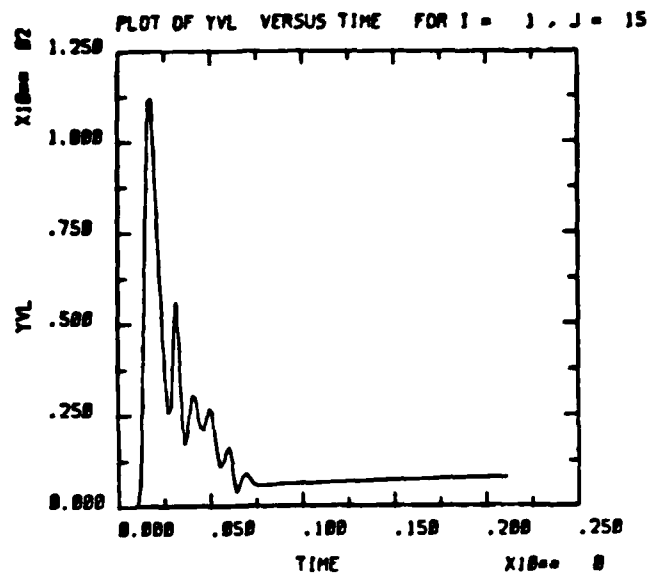
2.MT  
CYCLE NUMBER 858  
TIME .24717



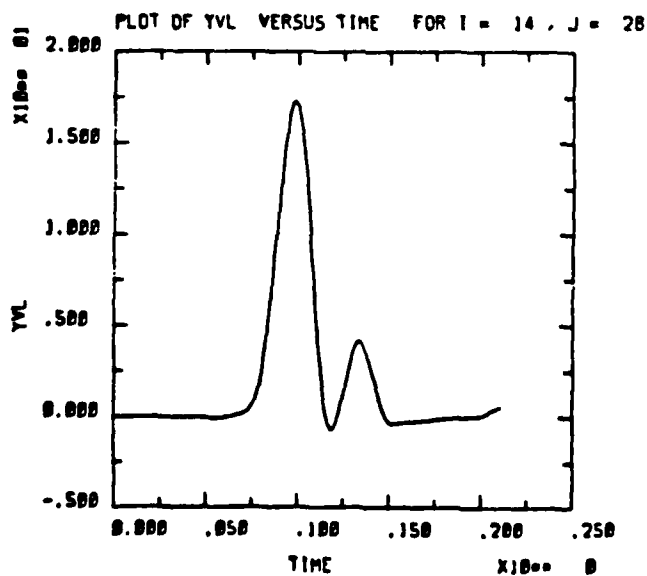
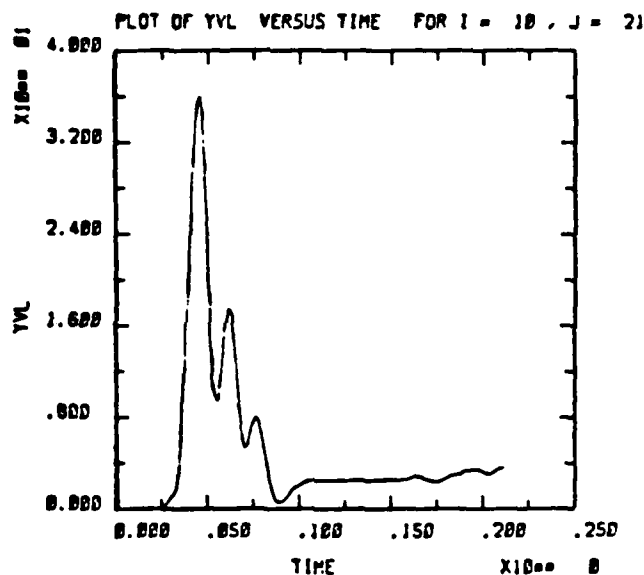
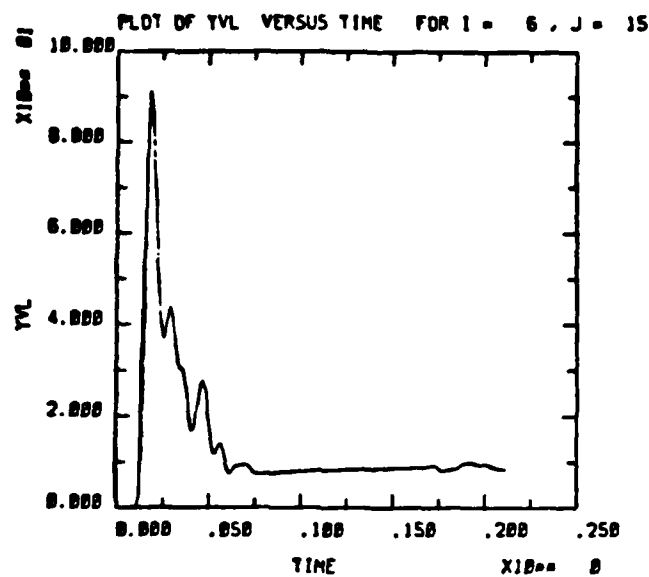
8.5MT  
CYCLE NUMBER 778  
TIME .15228



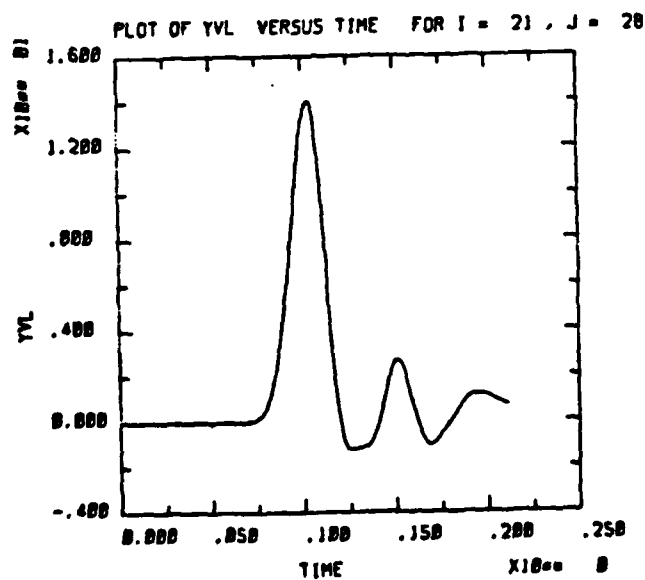
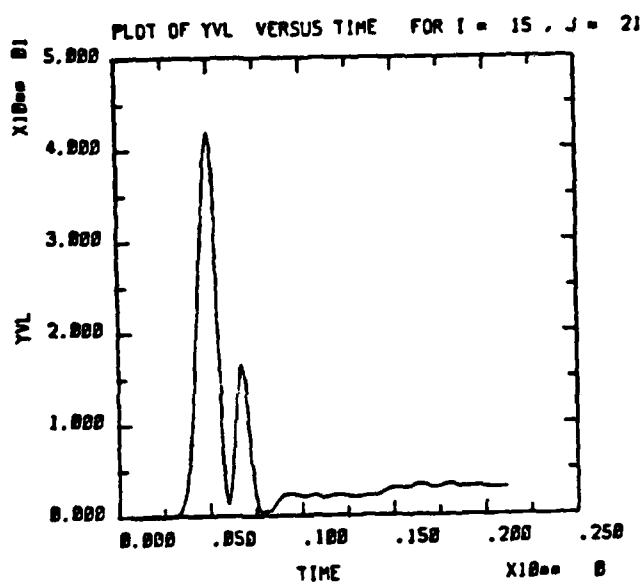
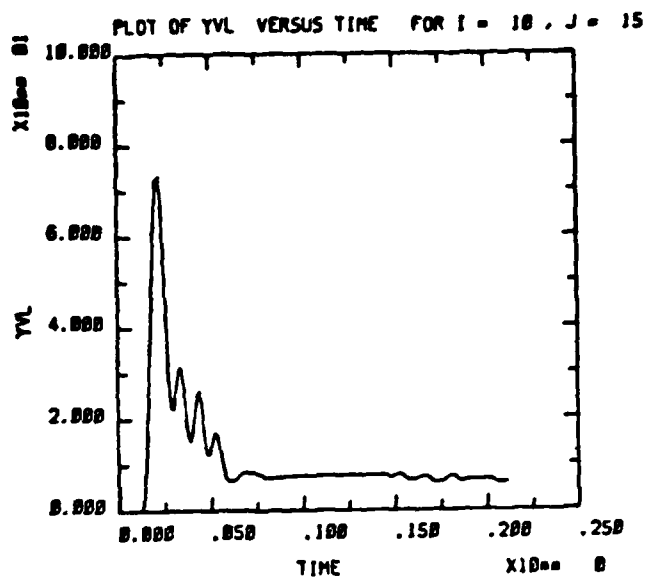




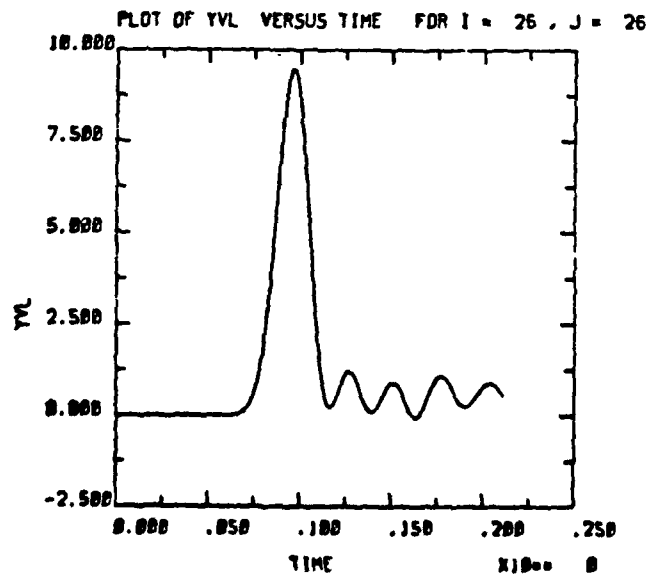
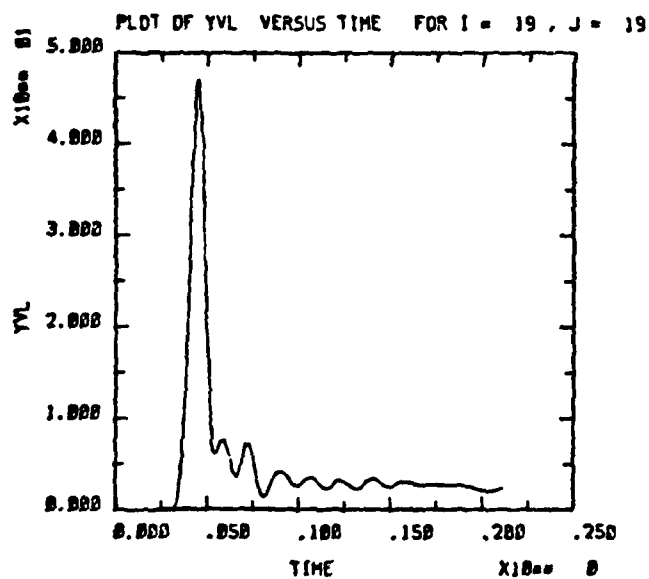
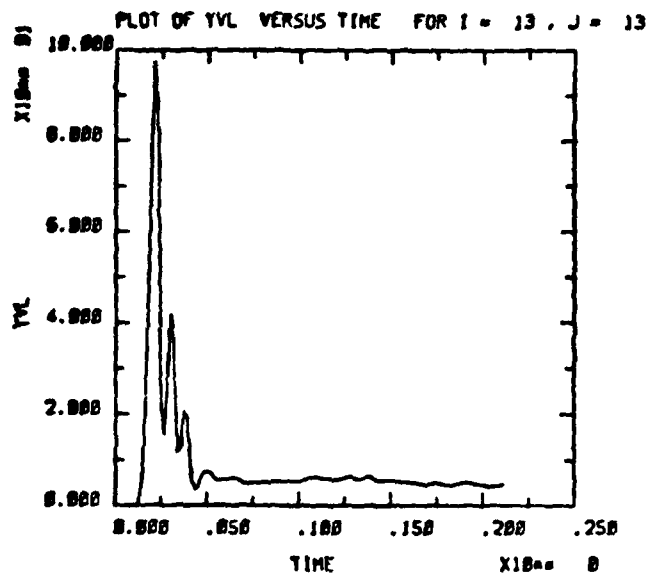
SPALL RUN No. 1, 1Mt, 1 Layer, Non-Hysteretic EOS



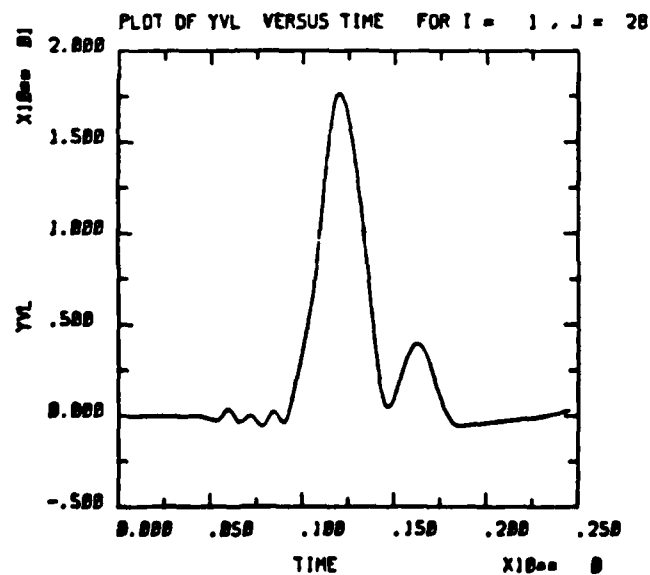
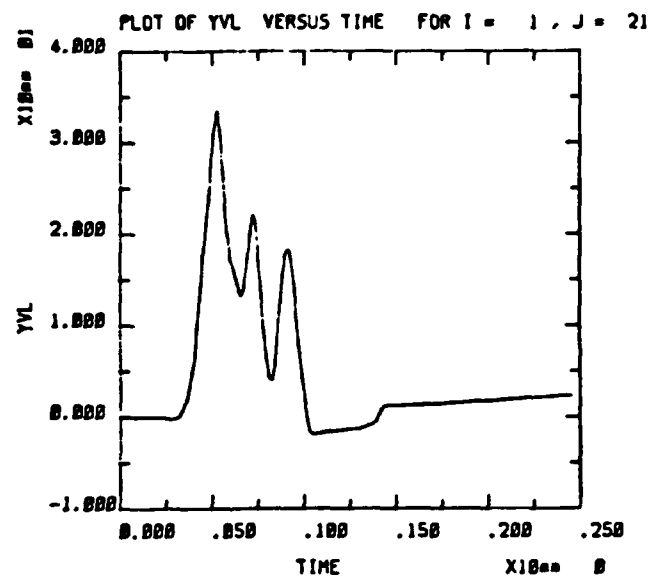
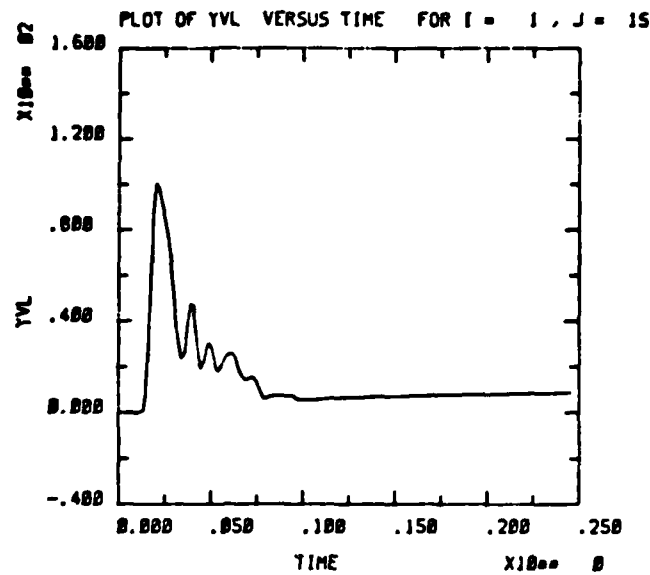
SPALL RUN No. 1, 1Mt, 1 Layer, Non-Hysteretic EOS



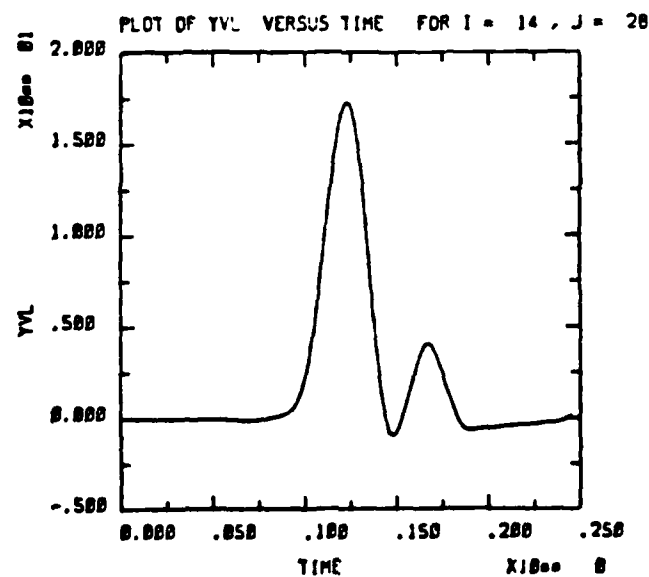
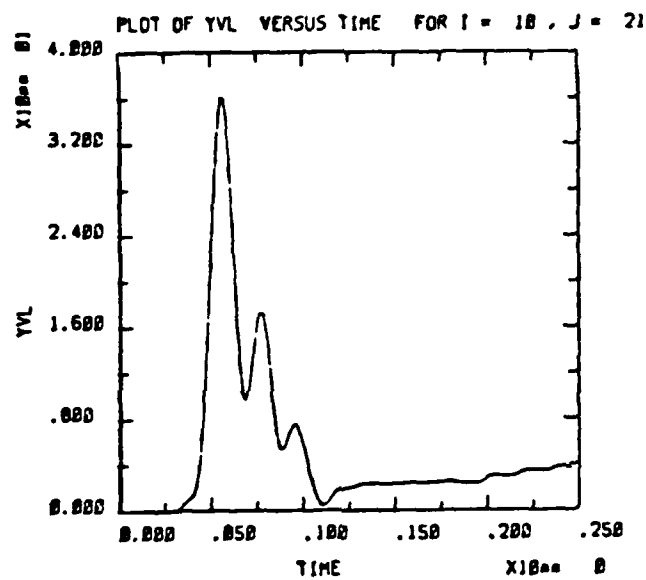
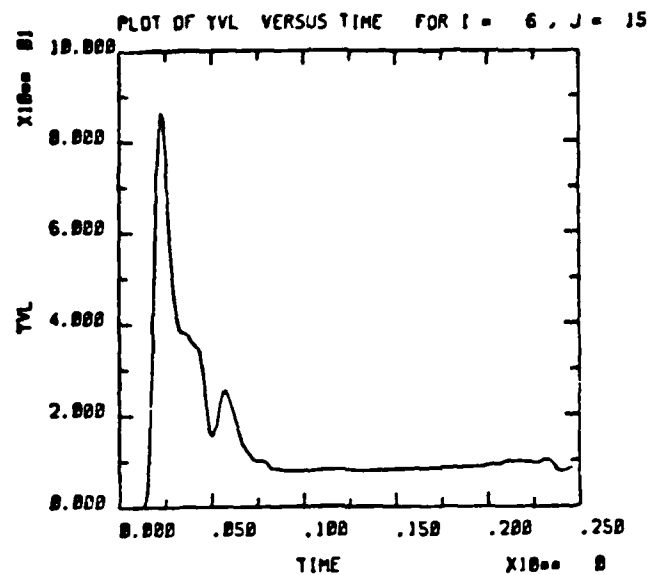
SPALL RUN No. 1, 1Mt, 1 Layer, Non-Hysteretic EOS



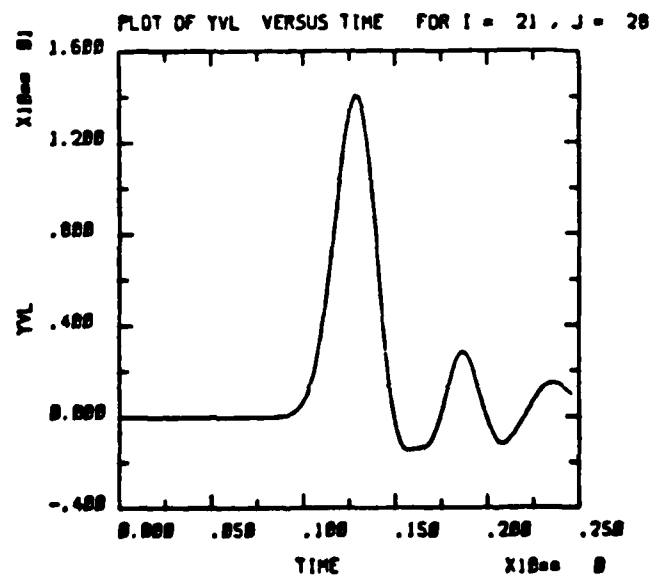
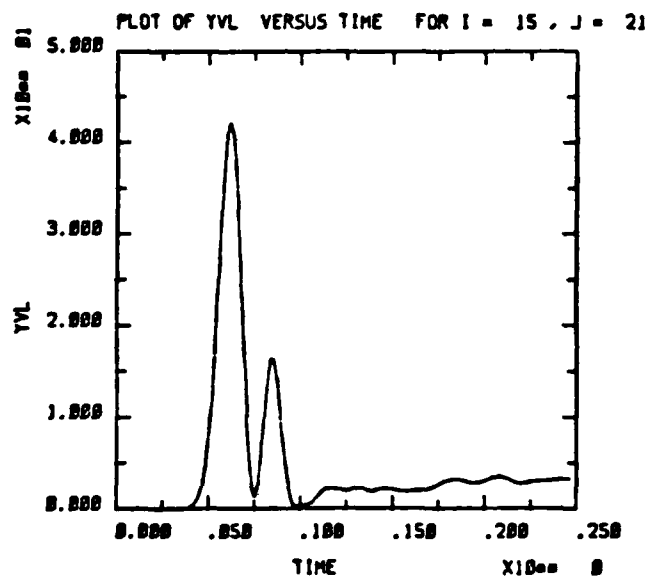
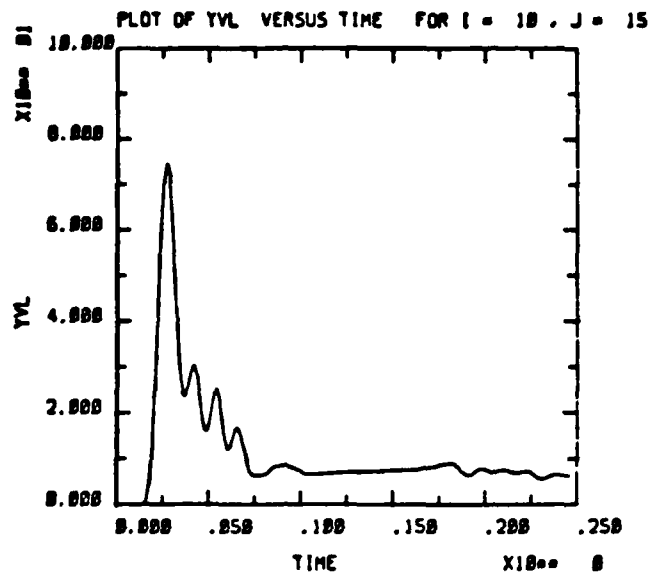
SPALL RUN No. 1, 1Mt, 1 Layer, Non-Hysteretic EOS



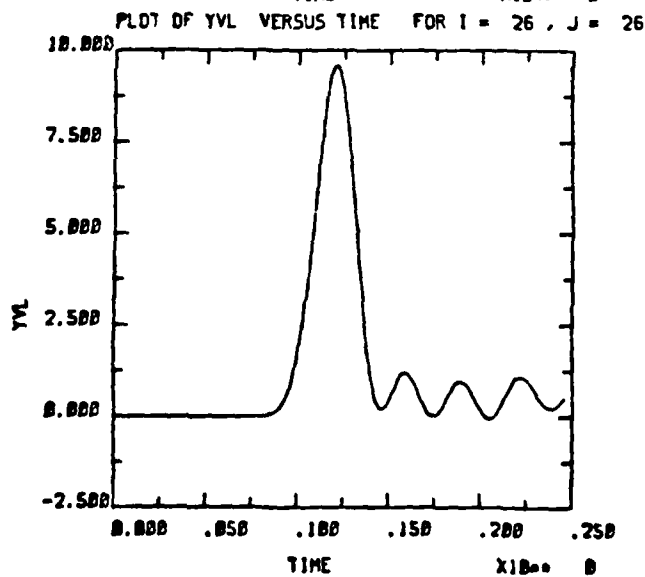
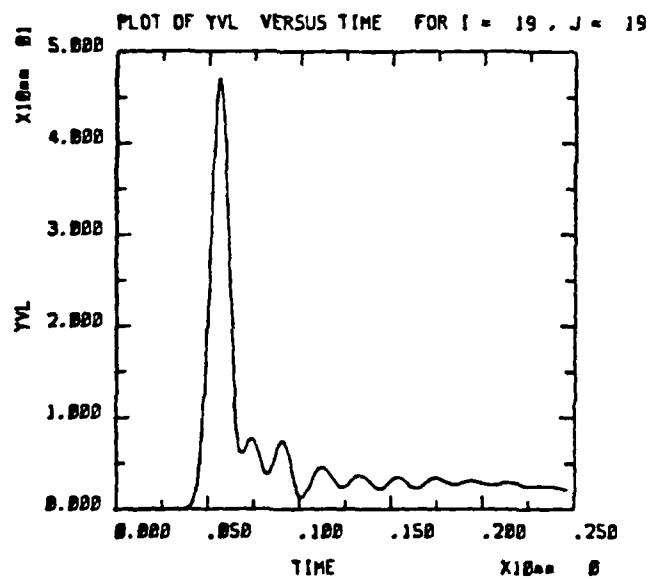
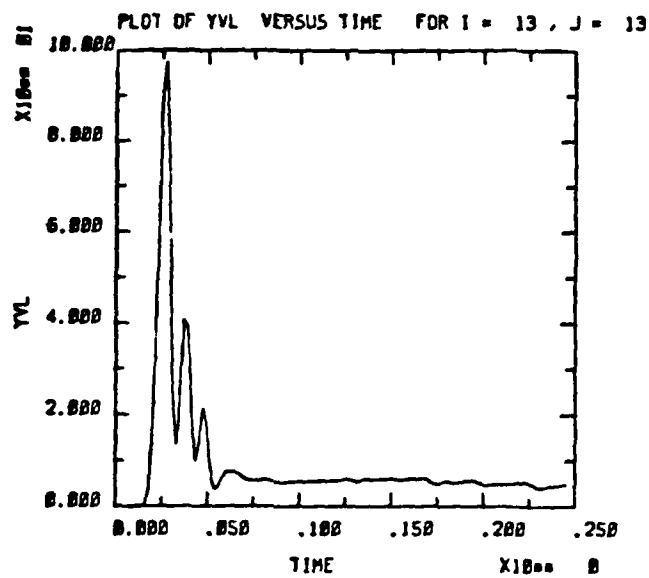
SPALL RUN No. 2, 2Mt, 1 Layer, Non-Hysteretic EOS



SPALL RUN No. 2, 2Mt, 1 Layer, Non-Hysteretic EOS

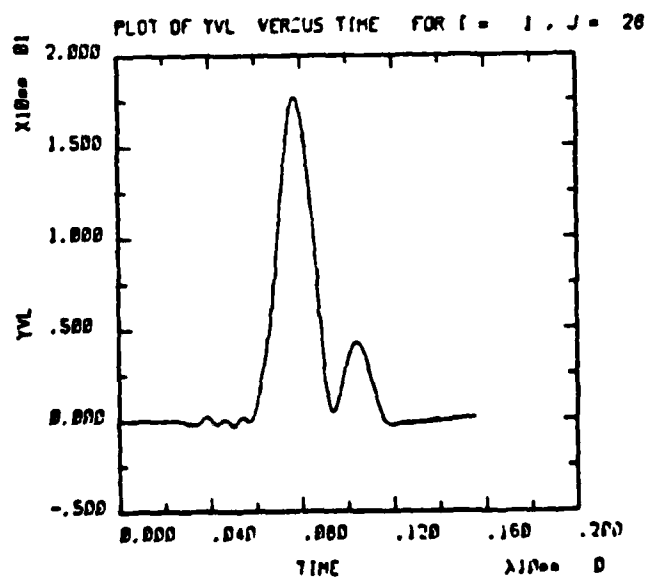
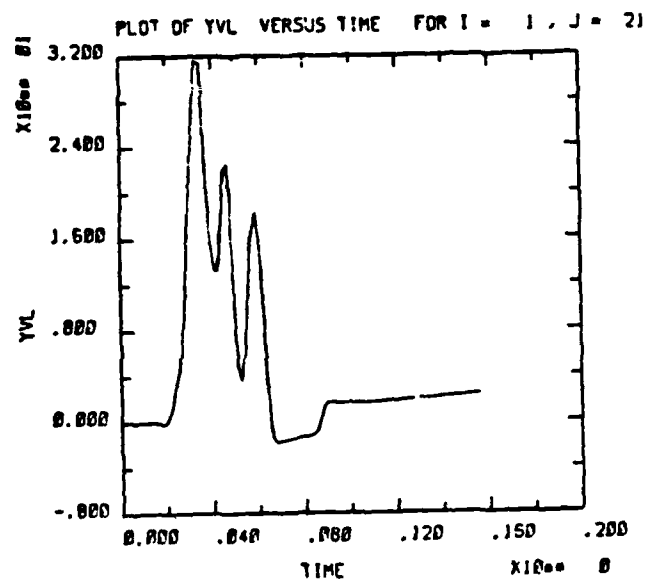
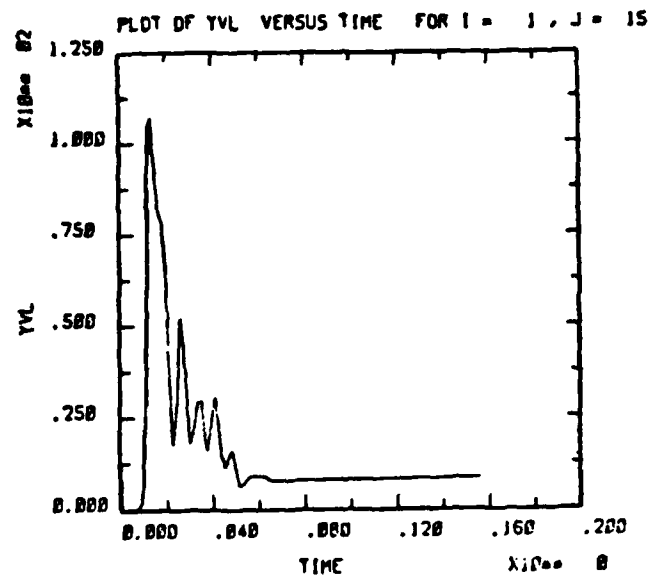


SPALL RUN No. 2, 2Mt, 1 Layer, Non-Hysteretic EOS

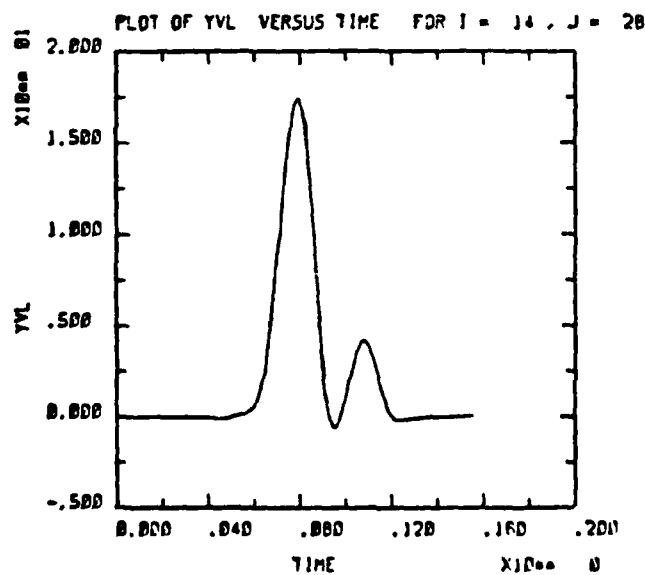
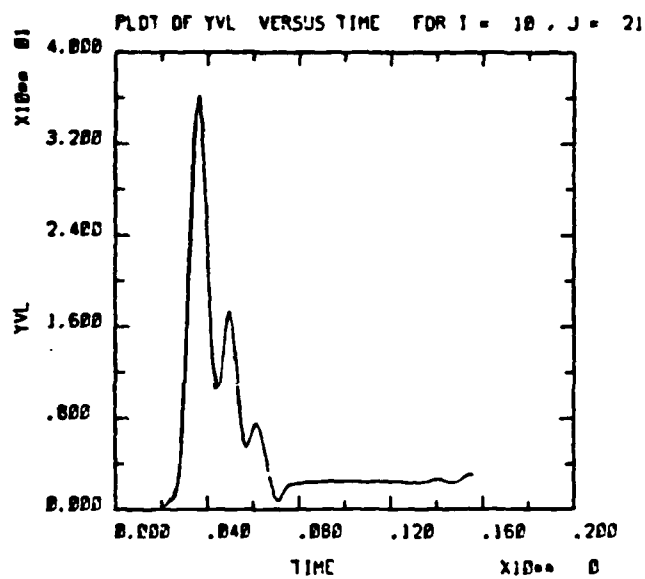
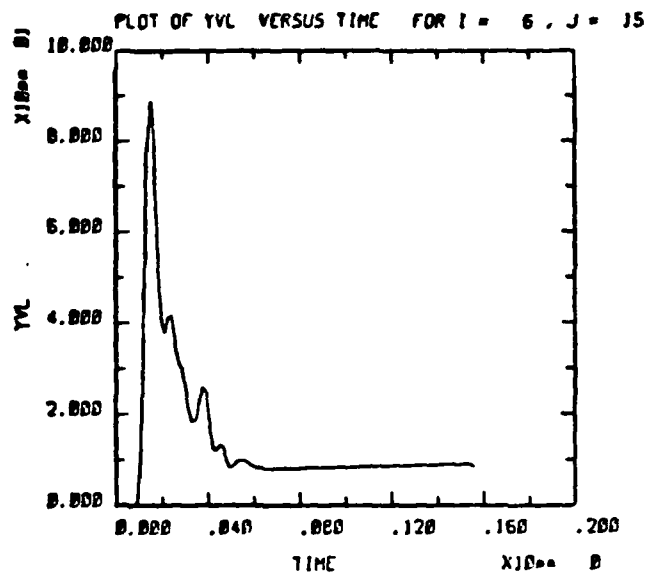


SPALL RUN No. 2, 2Mt, 1 Layer, Non-Hysteretic EOS

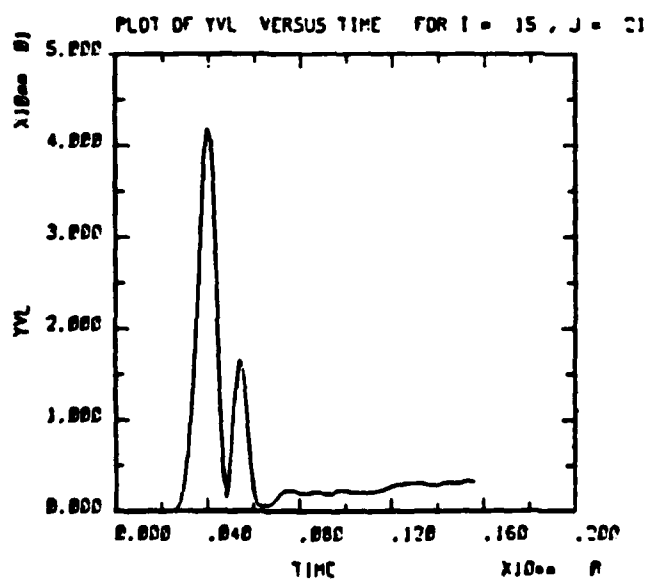
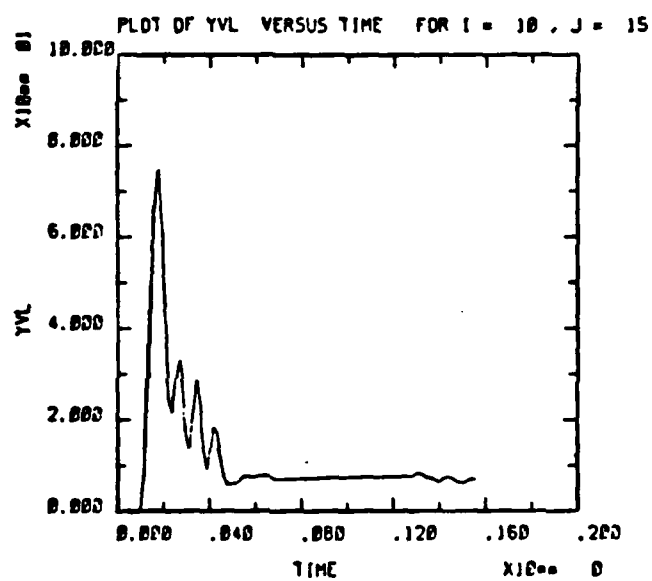




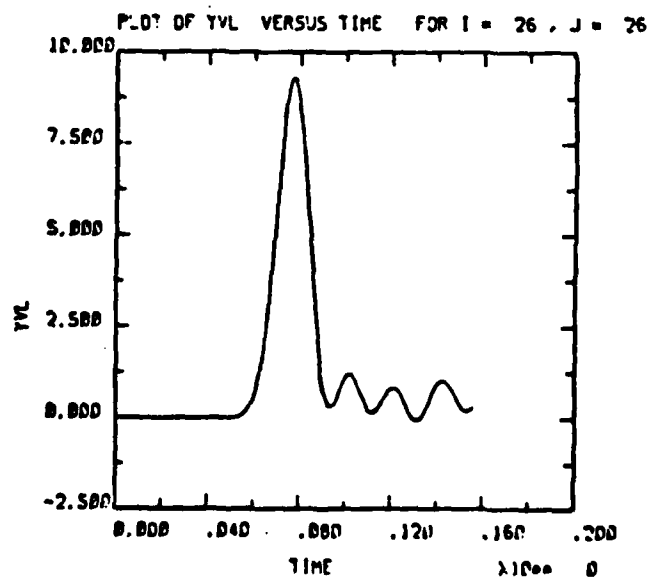
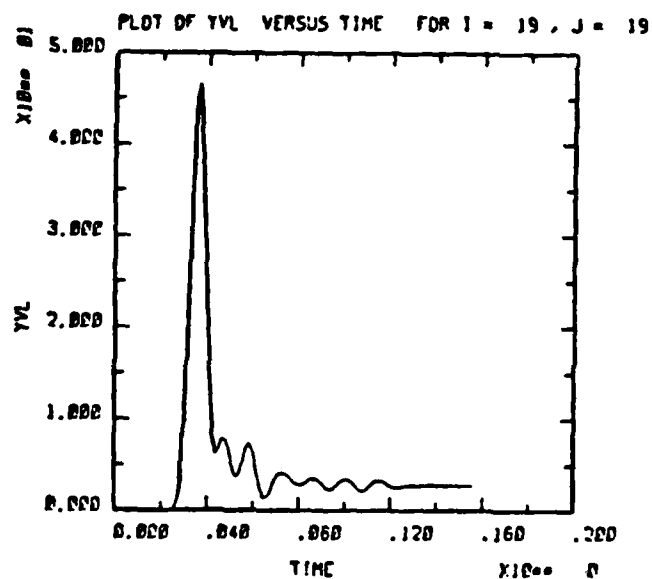
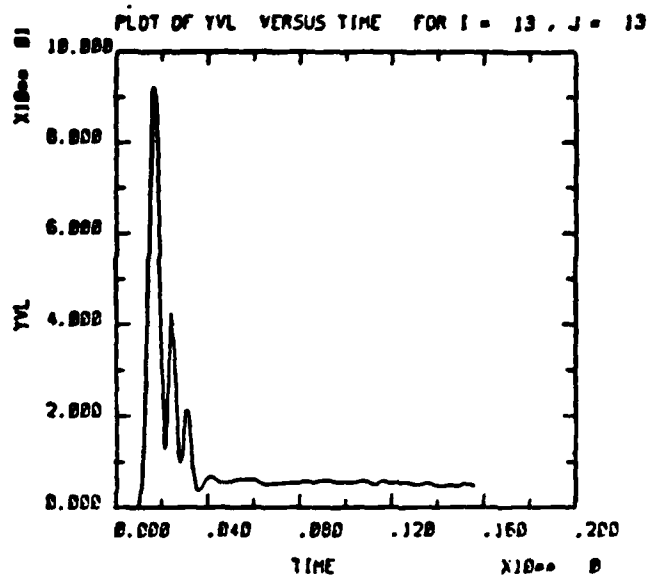
SPALL RUN No. 3, .5Mt, 1 Layer, Non-Hysteretic EOS



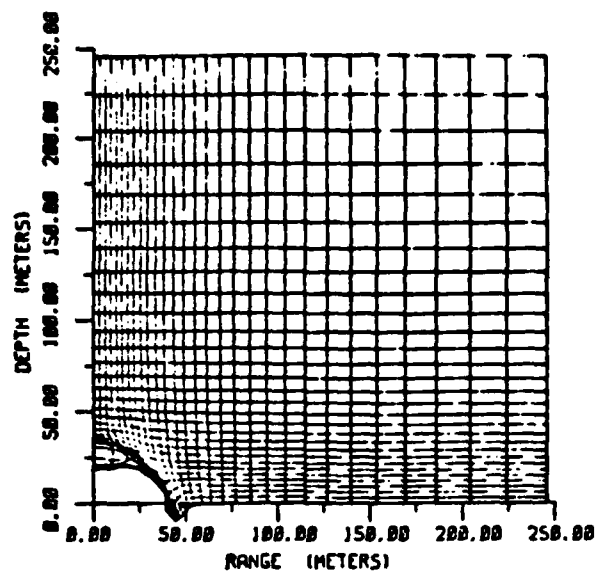
SPALL RUN No. 3, .5Mt, 1 Layer, Non-Hysteretic EOS



SPALL RUN No. 3, .5Mt, 1 Layer, Non-Hysteretic EOS



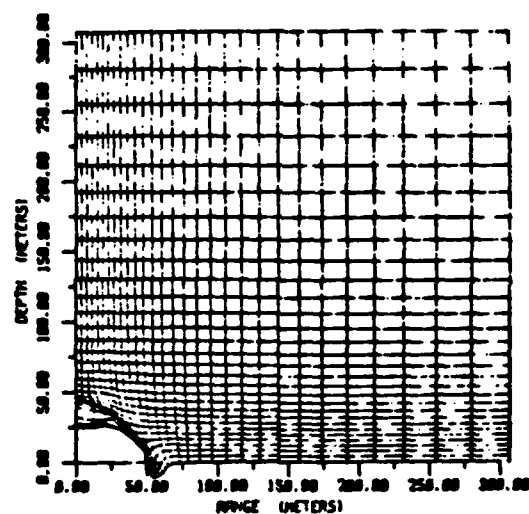
SPALL RUN No. 3, .5Mt, 1 Layer, Non-Hysteretic EOS



1 NT. HYSTERETIC EOS

CYCLE NUMBER 888

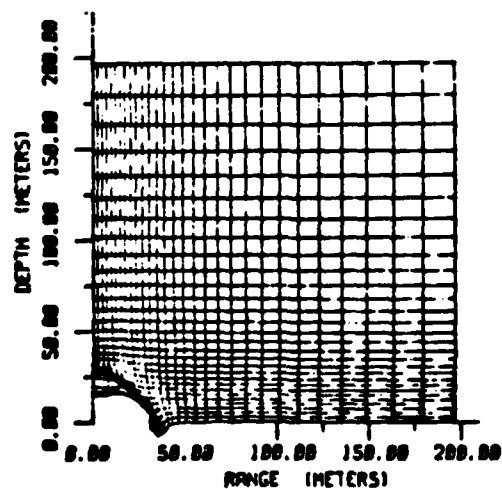
TIME .19152



2NT. HYSTERETIC EOS

CYCLE NUMBER 858

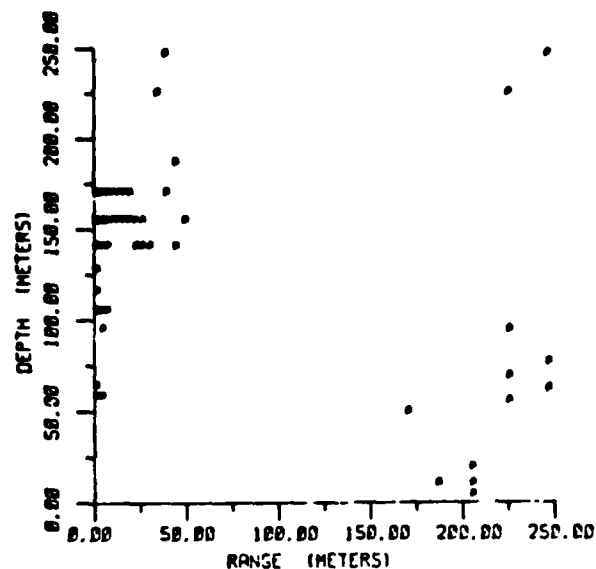
TIME .24681



8.SMT. HYSTERETIC EOS

CYCLE NUMBER 888

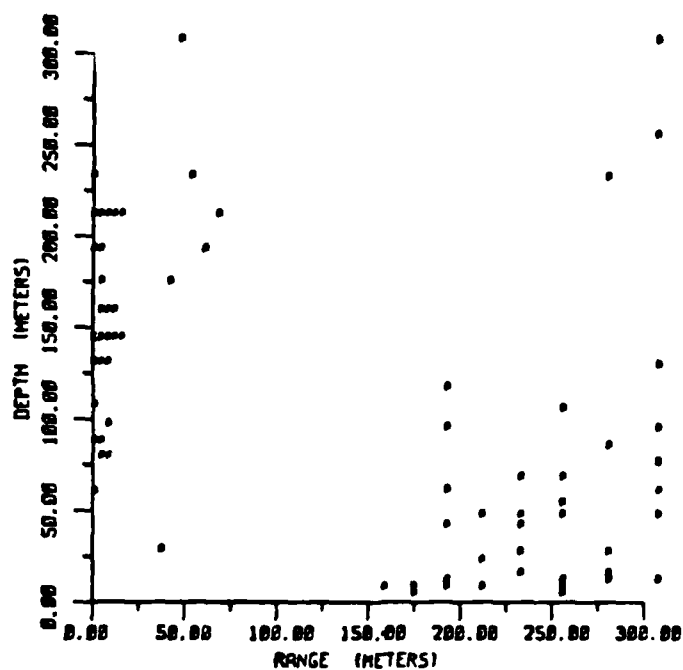
TIME .15372



1 MT. HYSTERETIC EOS

CYCLE NUMBER 000

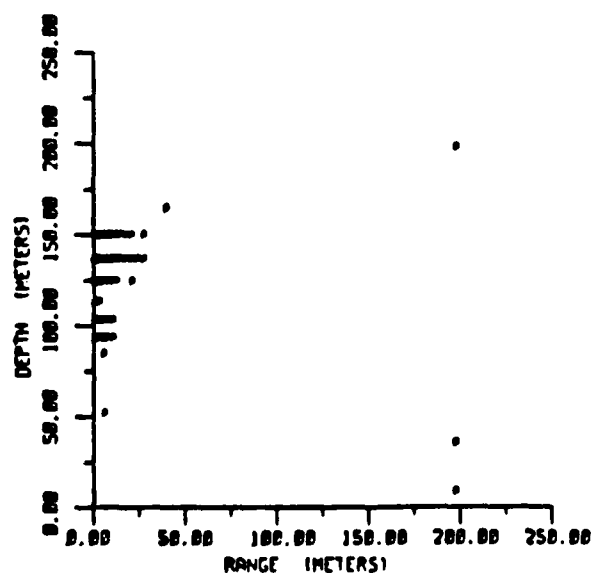
TIME .19152



2MT. HYSTERETIC EOS

CYCLE NUMBER 050

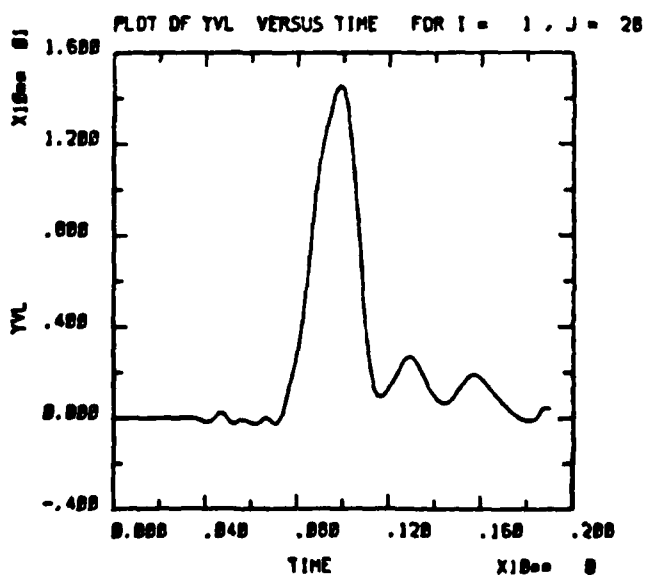
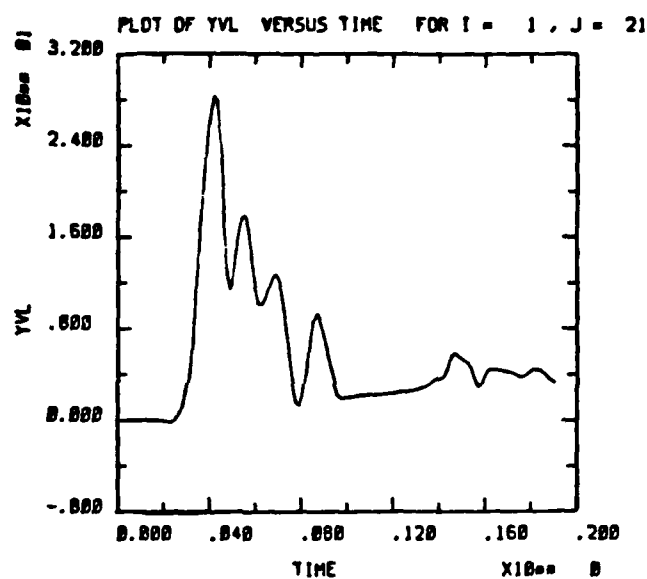
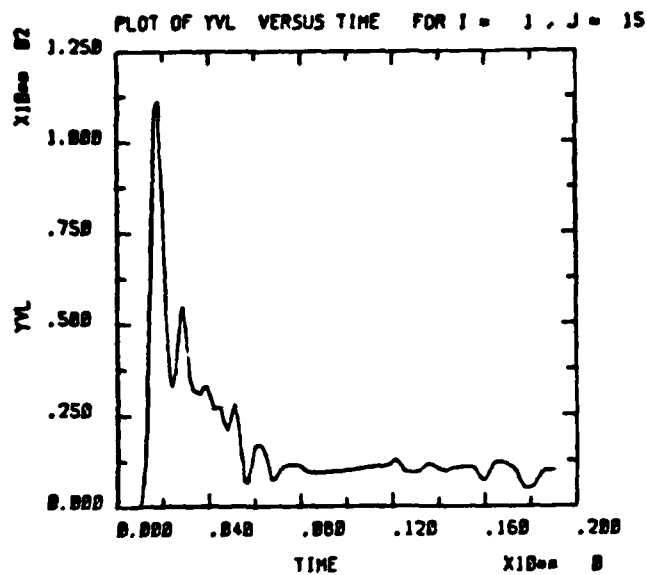
TIME .24501



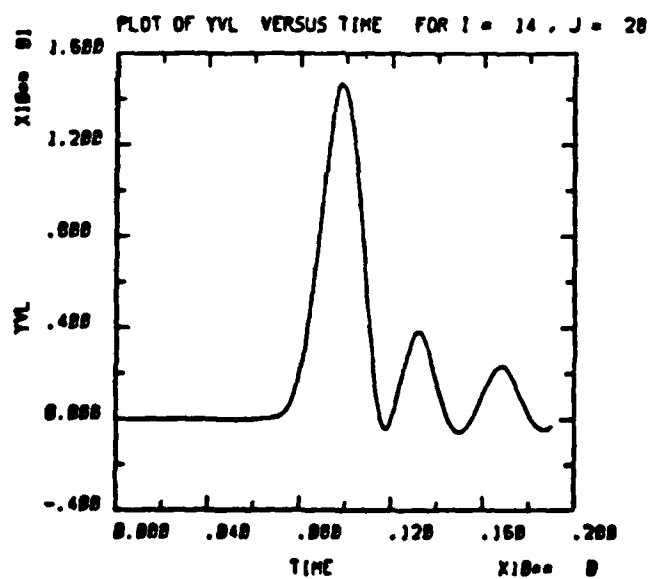
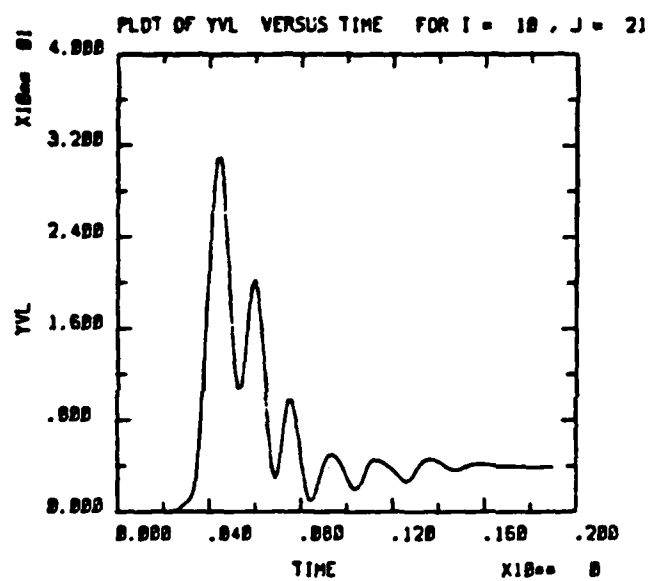
0.5MT. HYSTERETIC EOS.

CYCLE NUMBER 000

TIME .15372

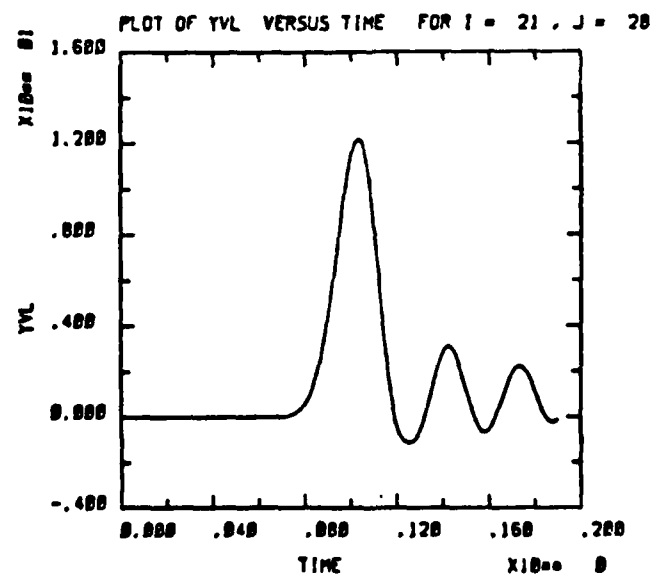
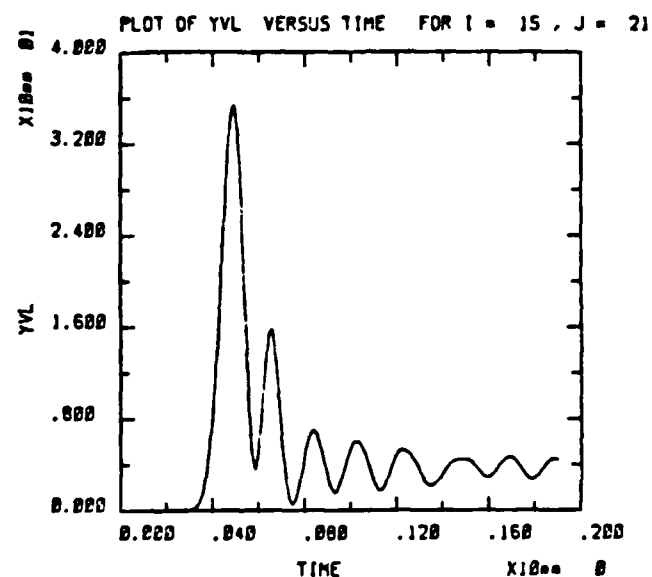
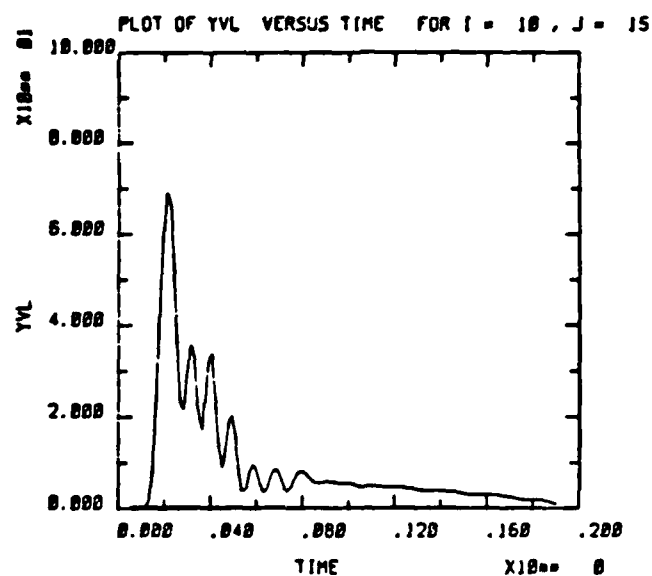


SPALL RUN No. 4, 1Mt, 1 Layer, Hysteretic EOS

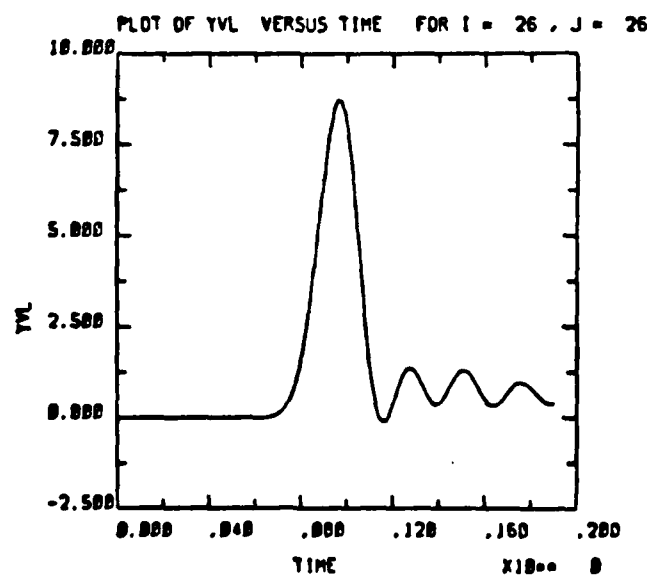
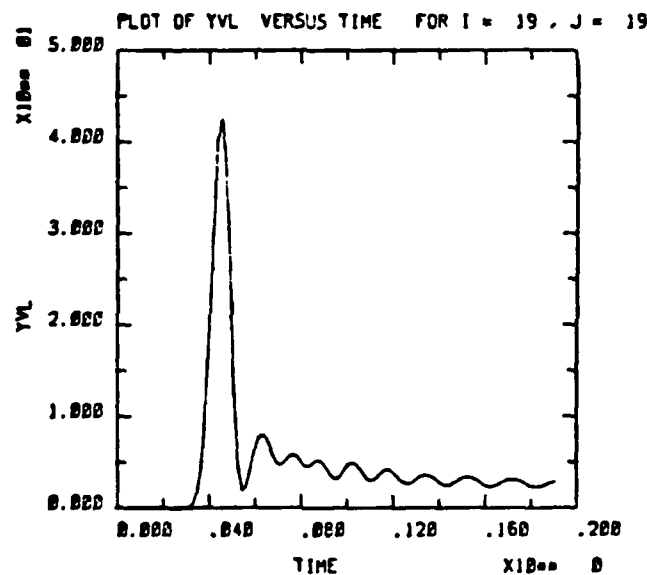
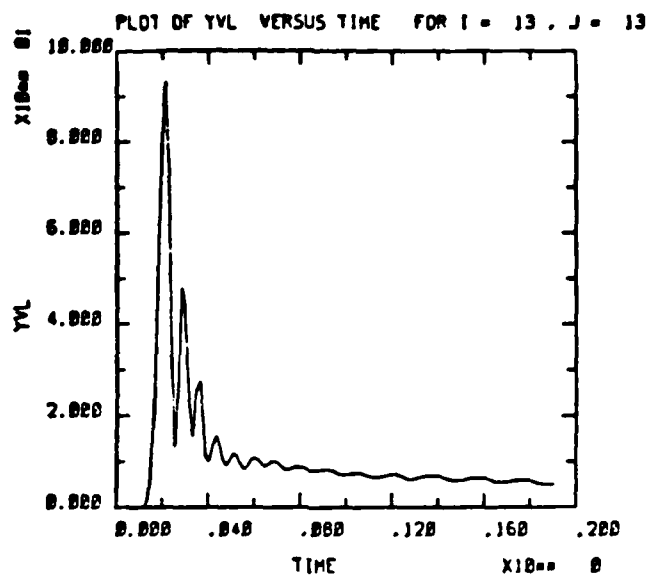


SPALL RUN No. 4, IMt, 1 Layer, Hysteretic EOS

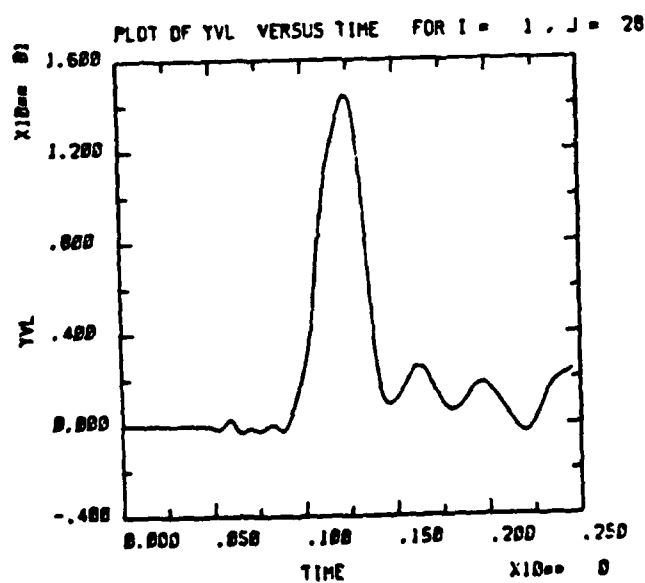
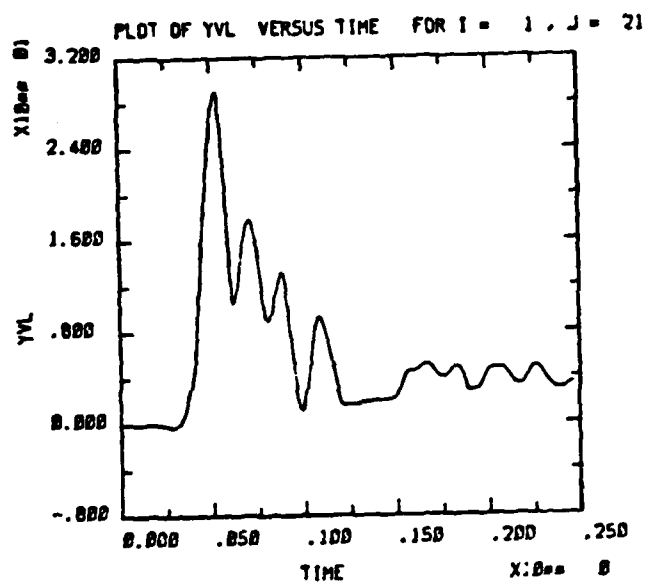
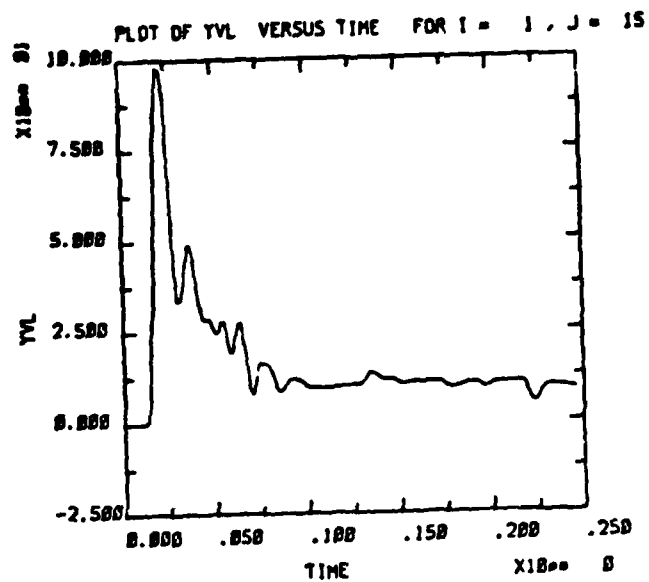




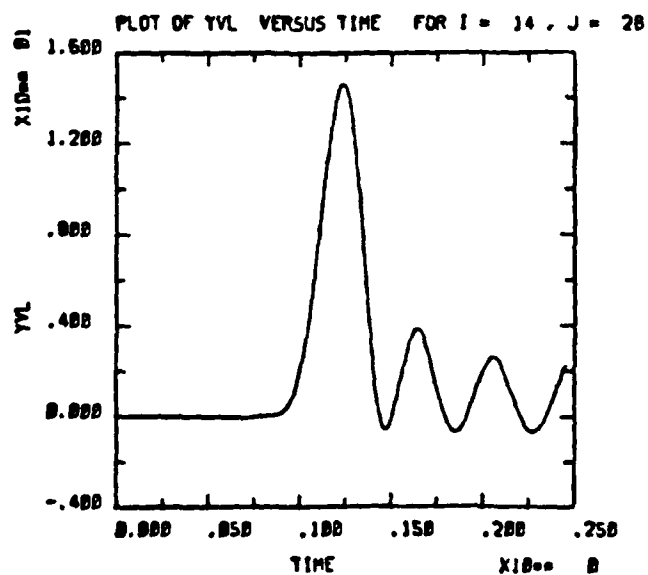
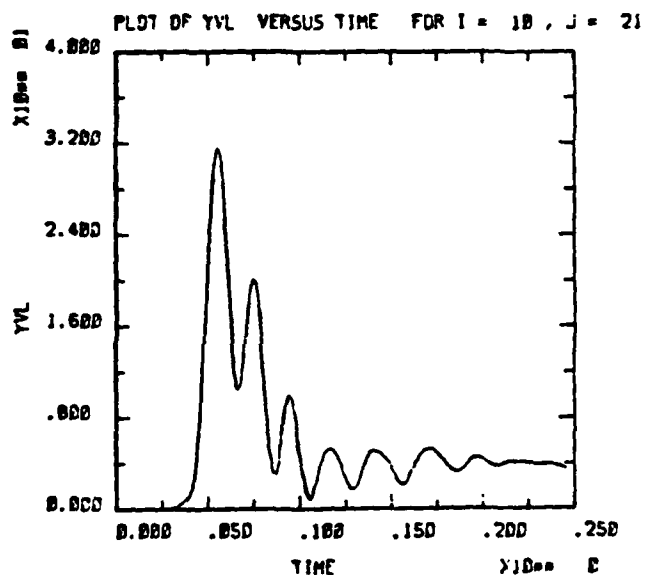
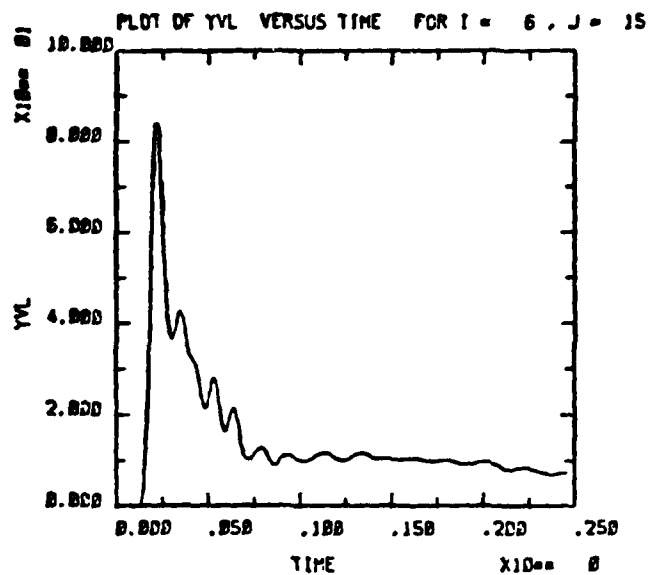
SPALL RUN No. 4, 1Mt, 1 Layer, Hysteretic EOS  
B-20



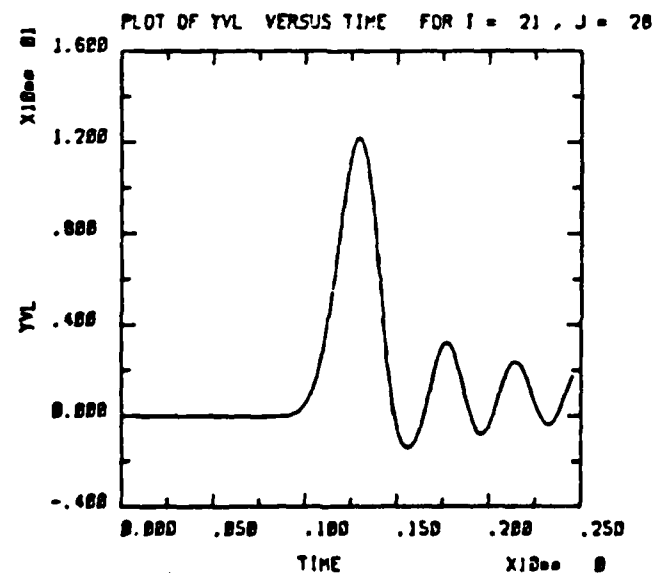
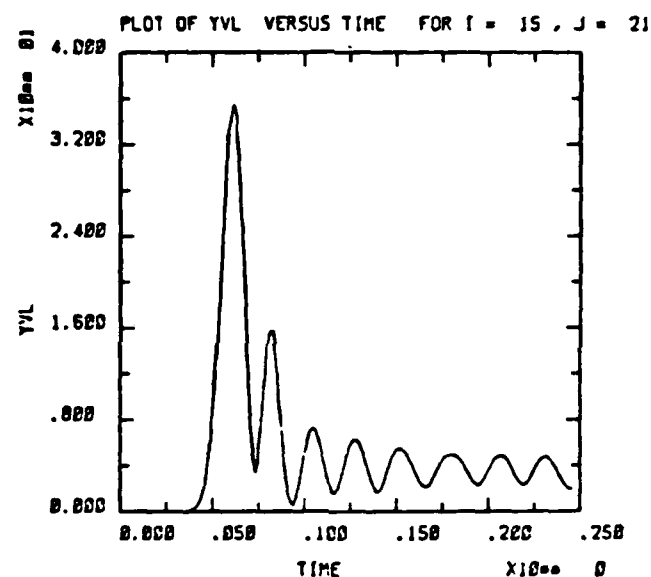
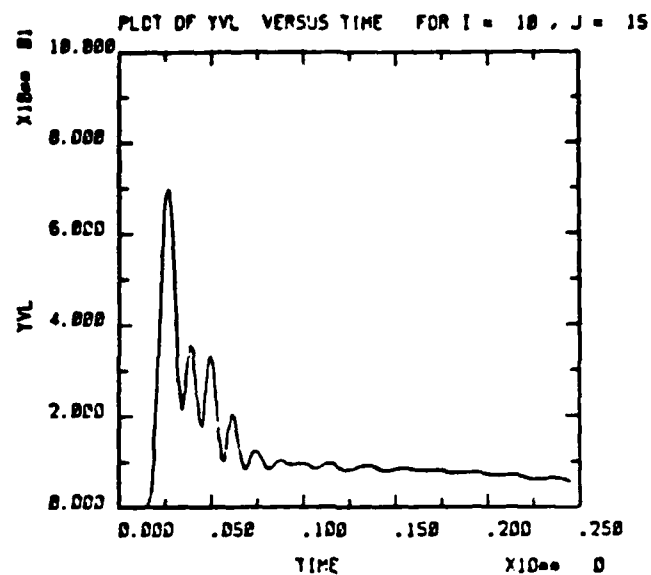
SPALL RUN No. 4, 1Mt, 1 Layer, Hysteretic EOS  
B-21



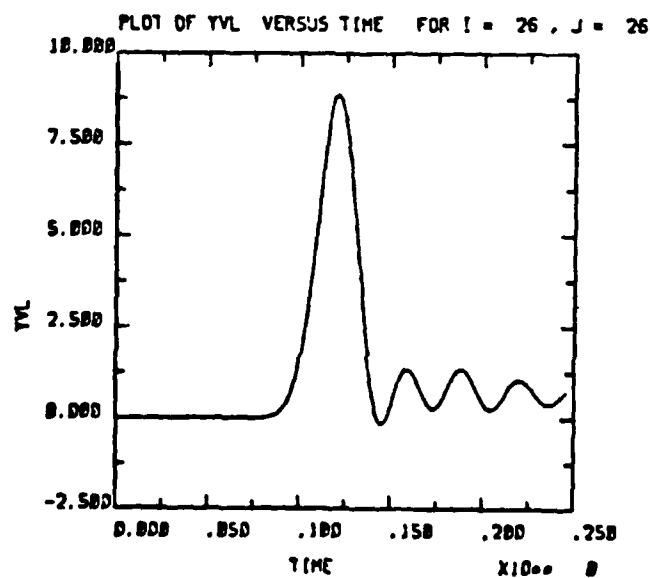
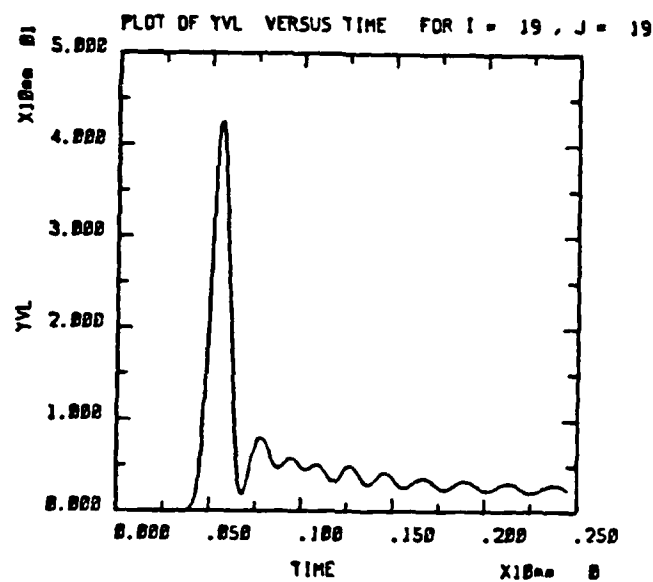
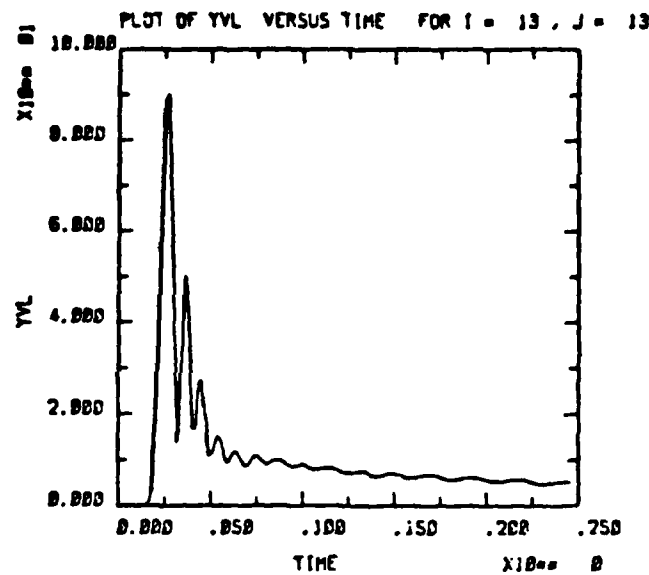
SPALL RUN No. 5, 2Mt, 1 Layer, Hysteretic EOS



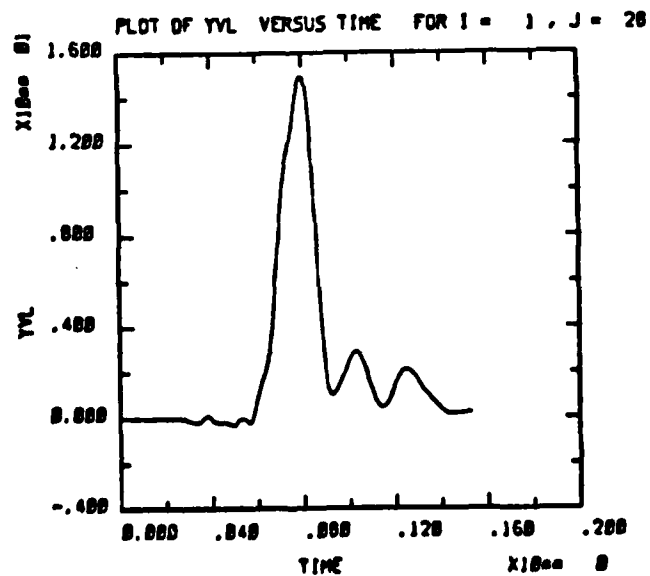
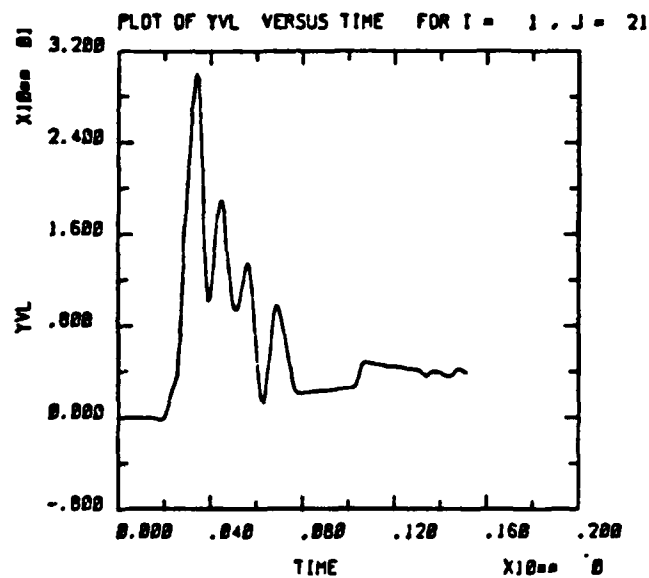
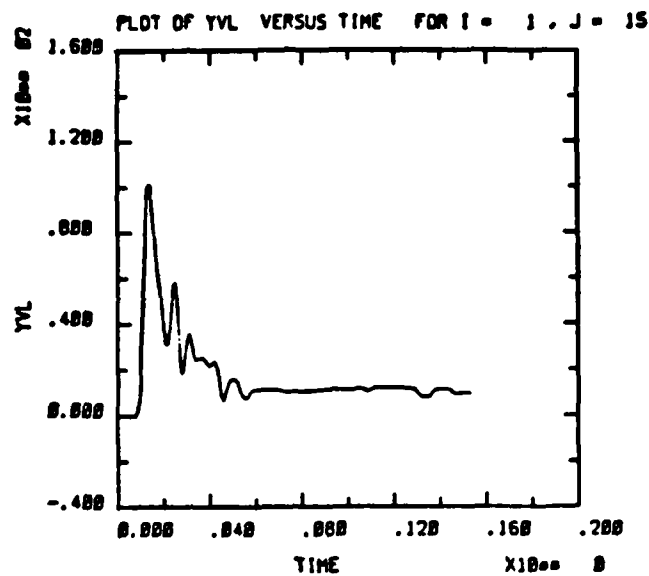
SPALL RUN No. 5, 2Mt, 1 Layer, Hysteretic EOS

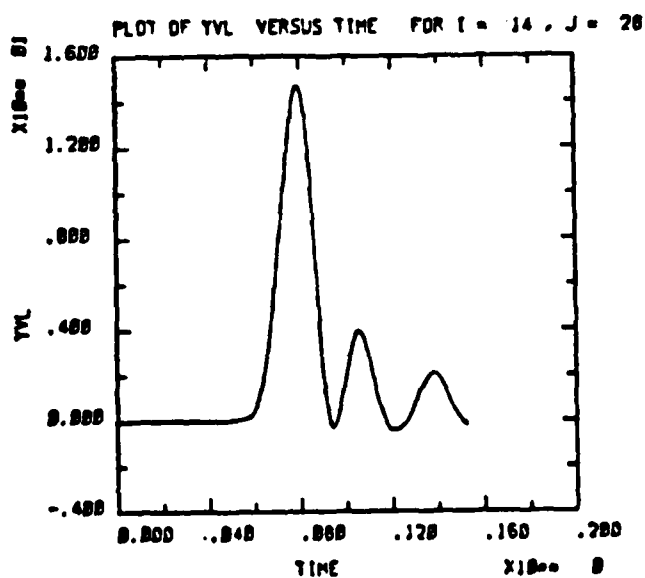
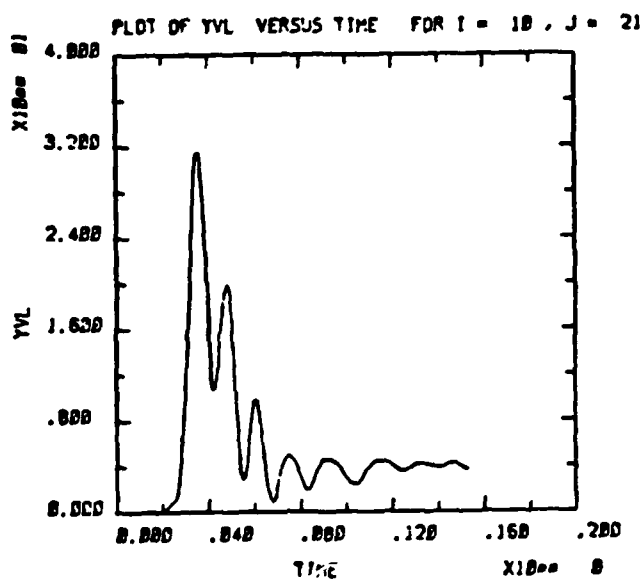
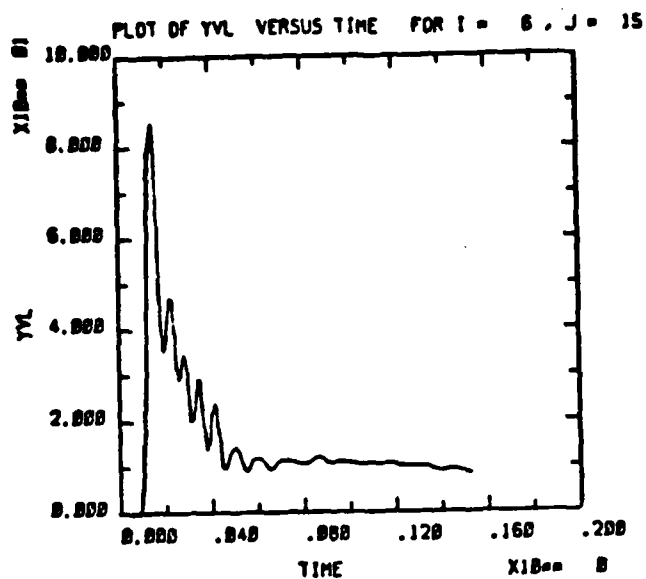


SPALL RUN No. 5, 2Mt, 1 Layer, Hysteretic EOS



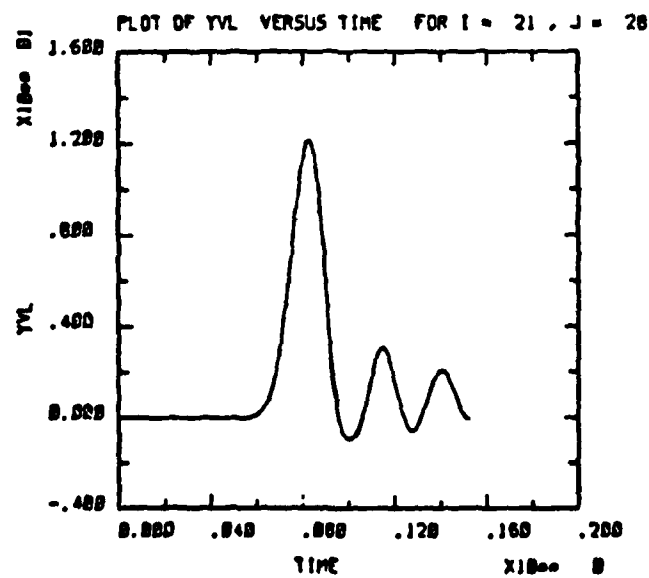
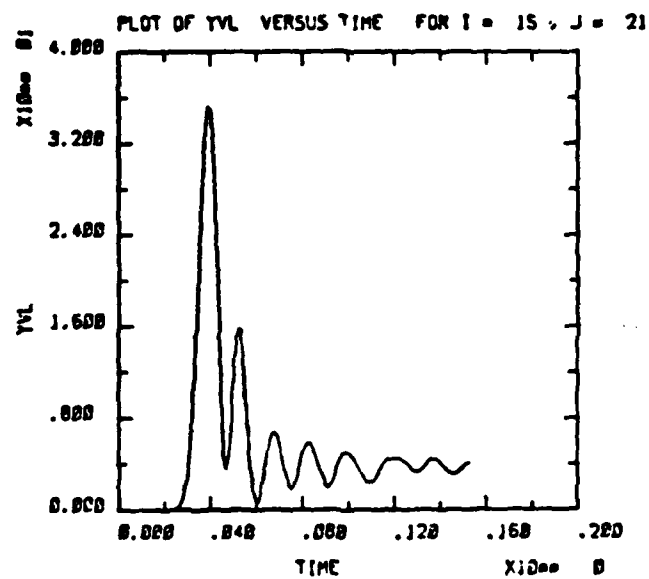
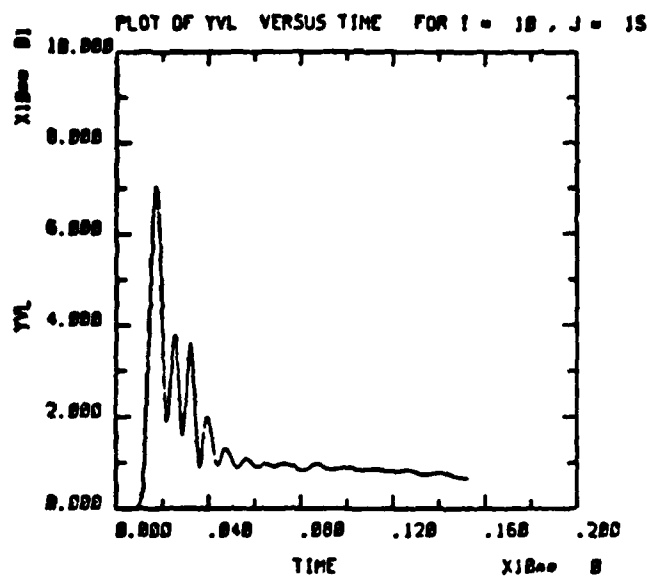
SPALL RUN No. 5, 2Mt, 1 Layer, Hysteretic EOS

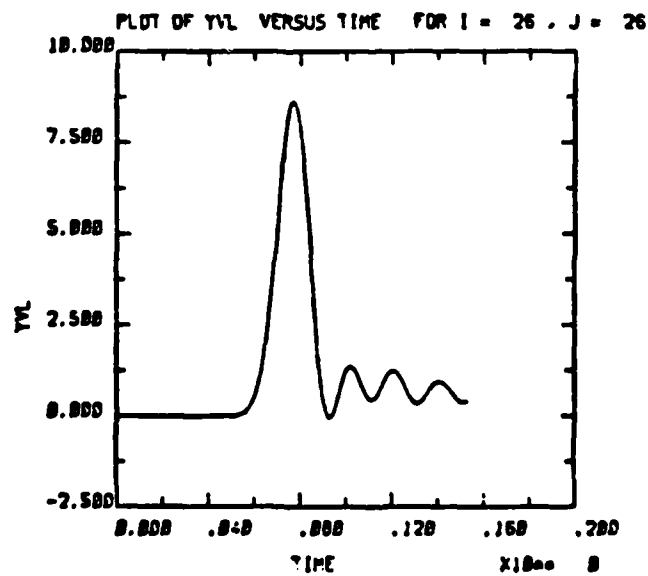
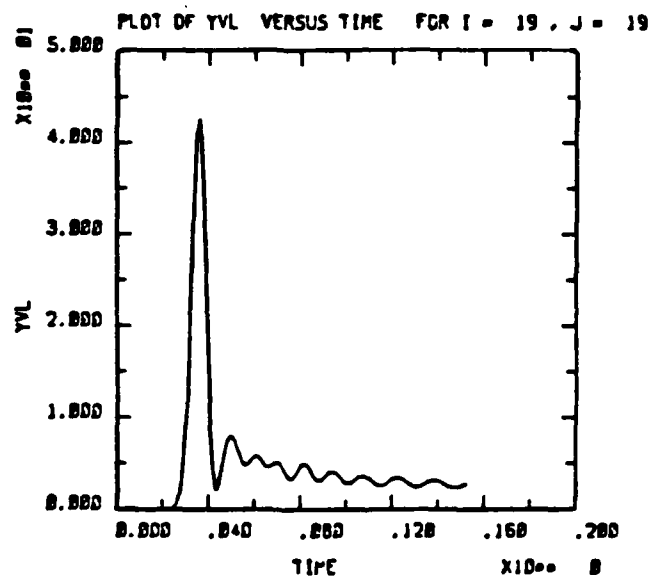
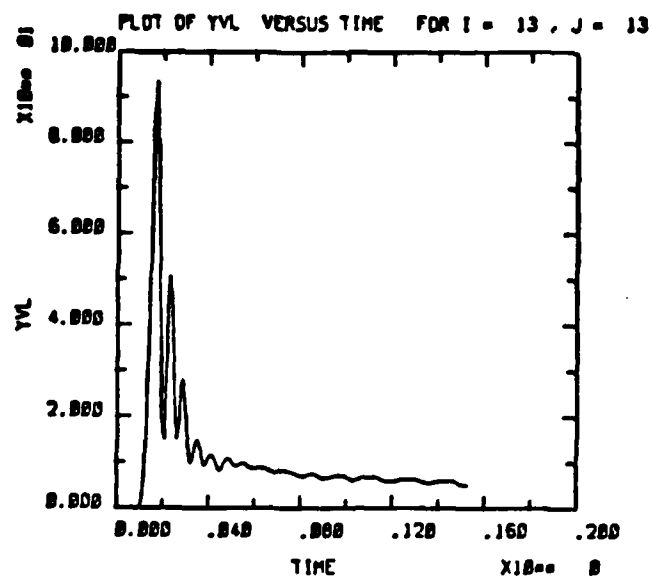




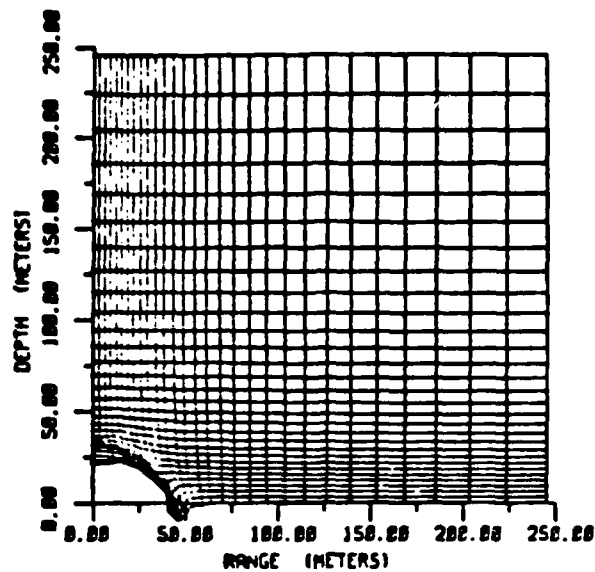
SPALL RUN No. 6, .5 Mt, 1 layer, Hysteretic EOS



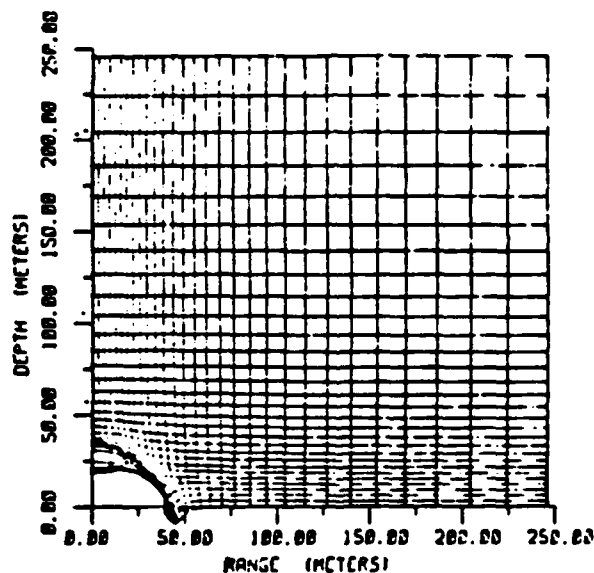




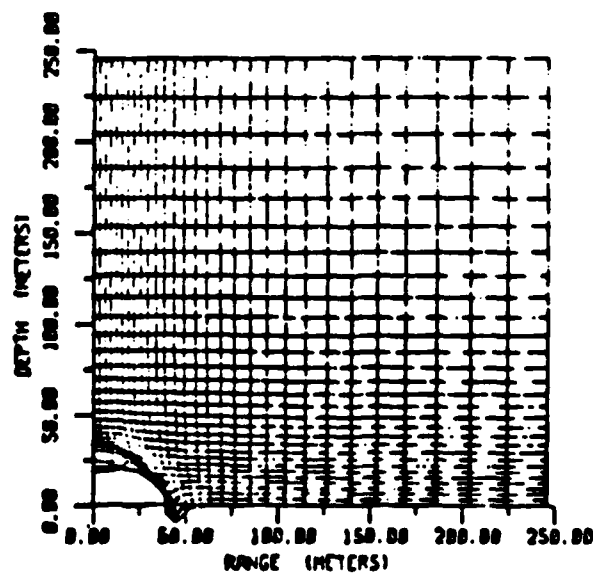
SPALL RUN No. 6, .5 Mt, 1 layer, Hysteretic EOS



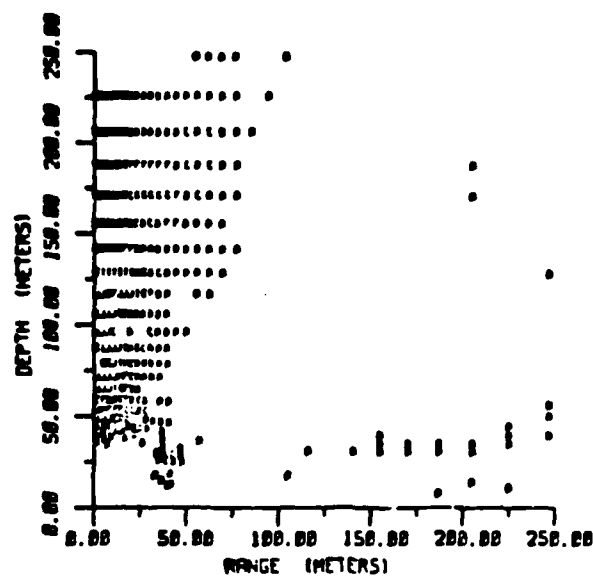
1 MT.  
NON-HYSTERETIC EOS  
CYCLE NUMBER 999  
TIME .21255



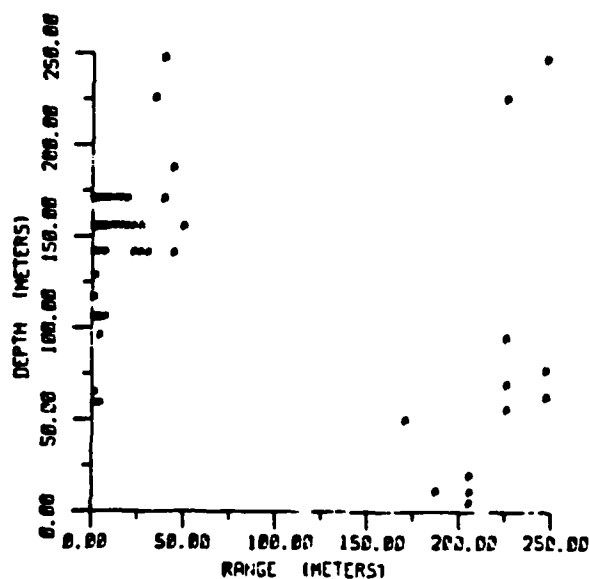
1 MT.  
HYSTERETIC EOS  
CYCLE NUMBER 000  
TIME .15152



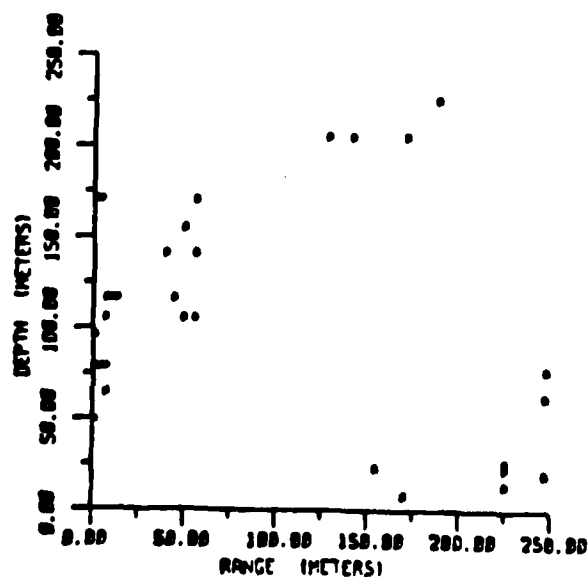
1MT  
HYSTERETIC EOS  
2 LAYER  
CYCLE NUMBER 000  
TIME .19070



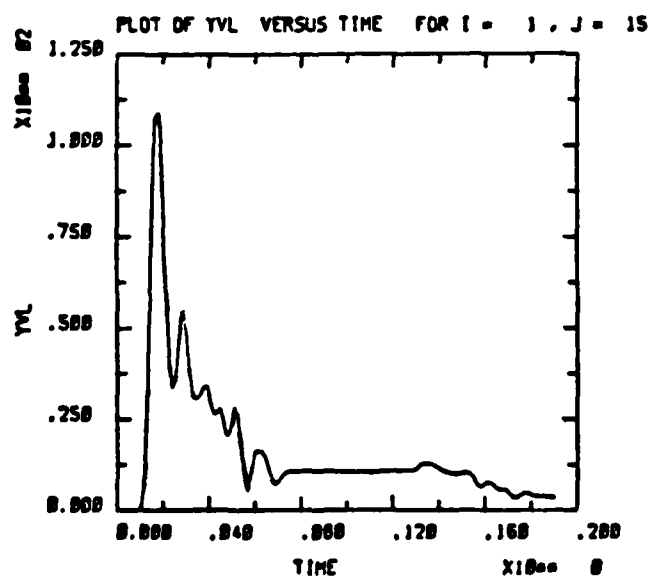
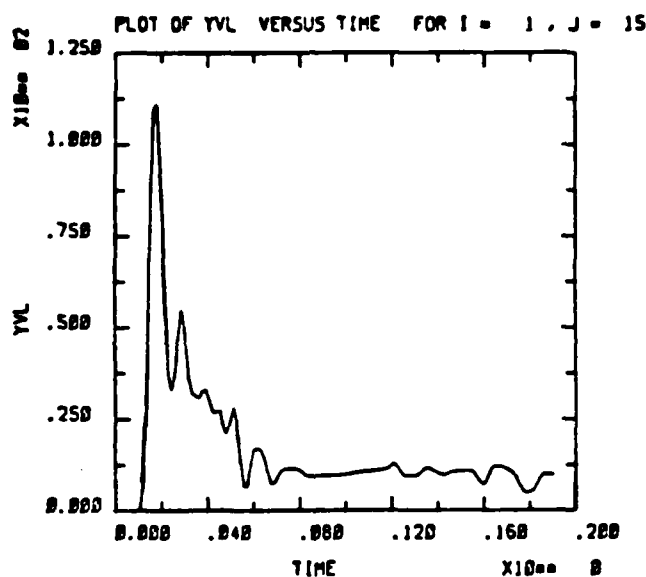
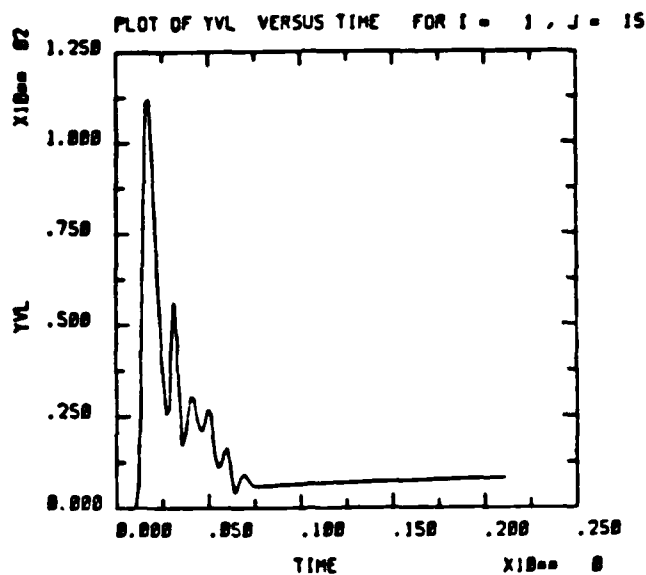
3 MY.  
NON-HYSTERETIC EOS  
CYCLE NUMBER 999  
TIME .21255



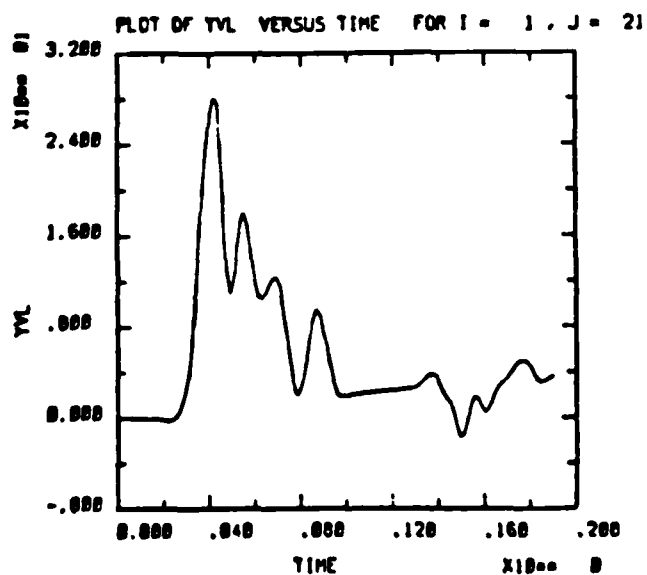
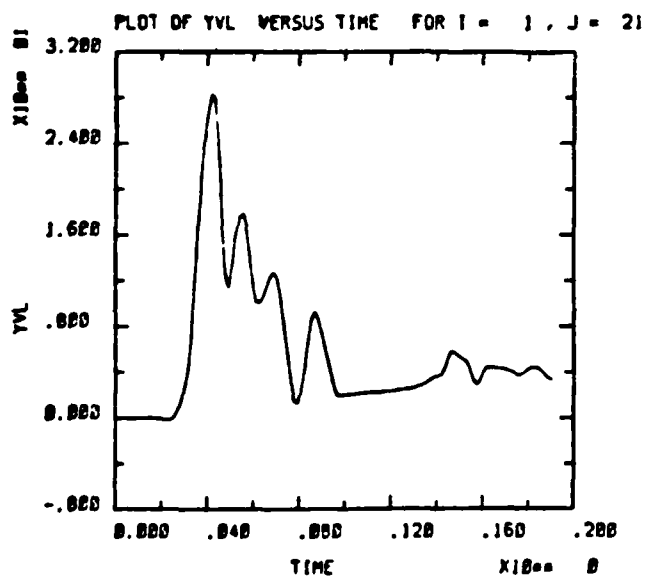
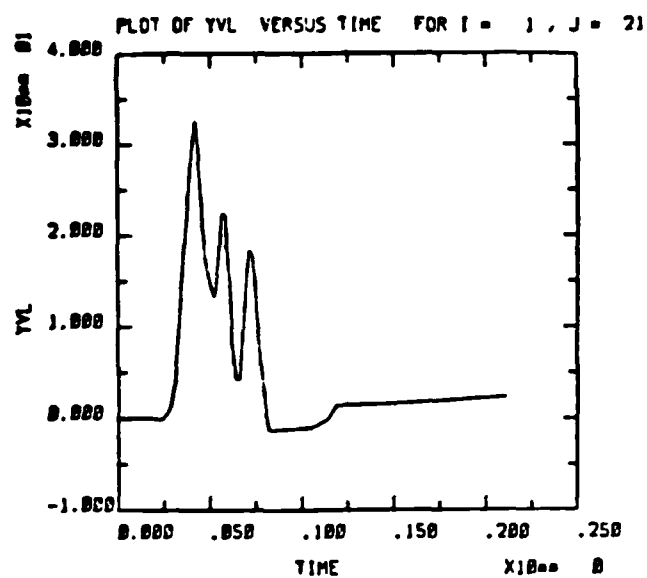
3 MY.  
HYSTERETIC EOS  
CYCLE NUMBER 820  
TIME .19152



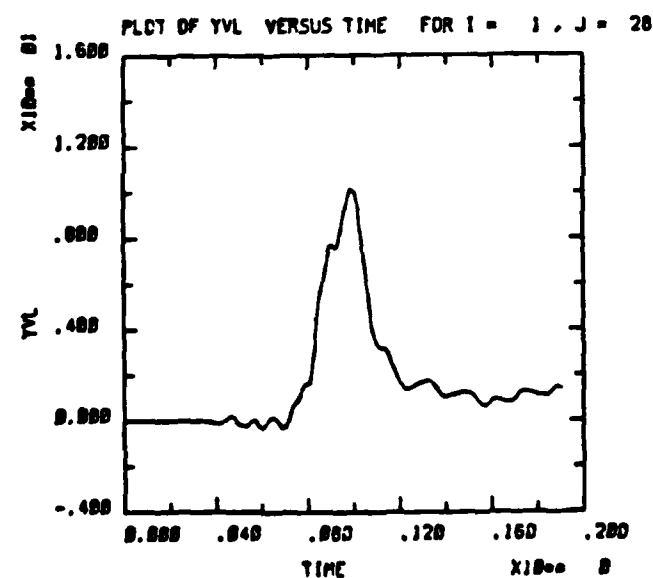
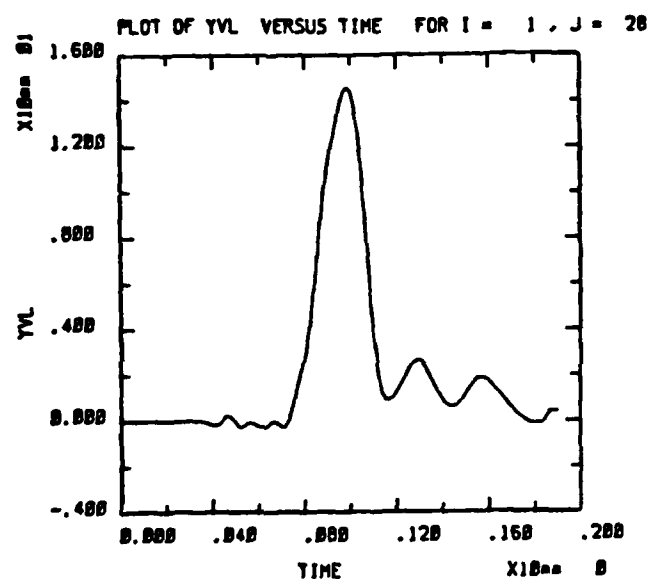
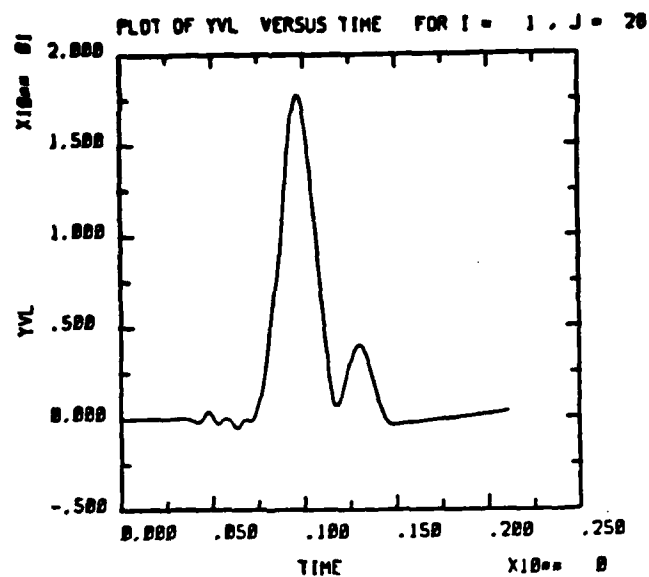
3 MY  
HYSTERETIC EOS  
2 LAYER  
CYCLE NUMBER 820  
TIME .19270



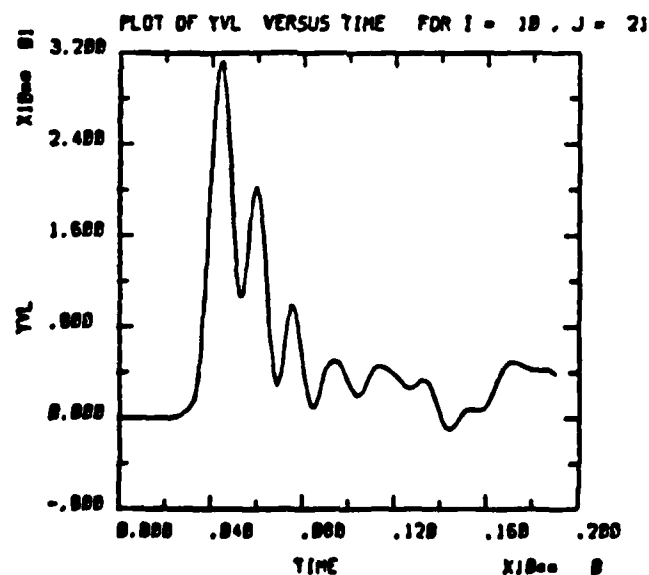
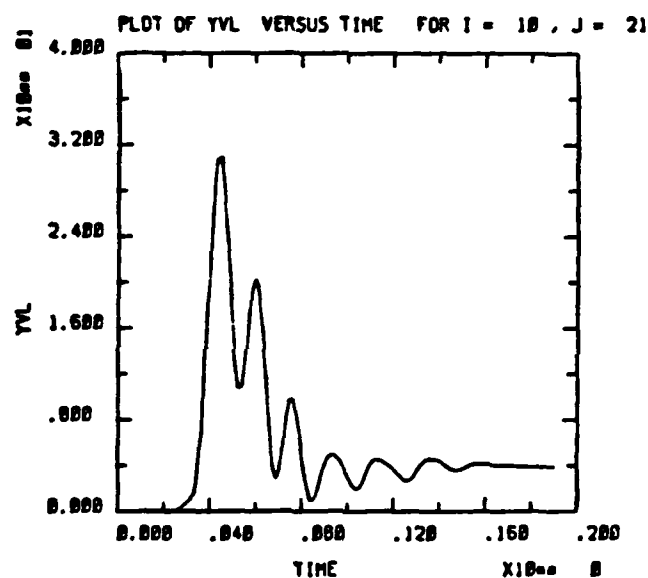
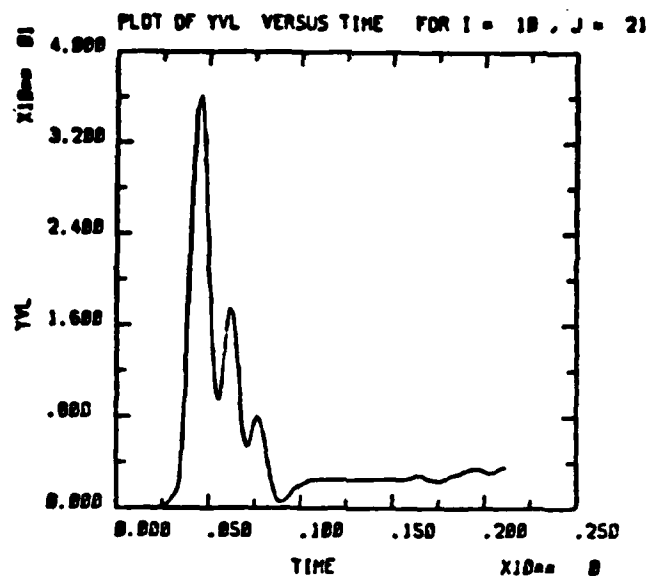
1 Mt comparisons of the 1 layer Non-hysteretic EOS (Run No. 1),  
 1 layer hysteretic EOS (Run No. 4), and 2 layer hysteretic EOS (Run No. 7)



1 Mt comparisons of the 1 layer Non-hysteretic EOS (Run No. 1),  
 1 layer hysteretic EOS (Run No. 4), and 2 layer hysteretic EOS (Run No. 7)

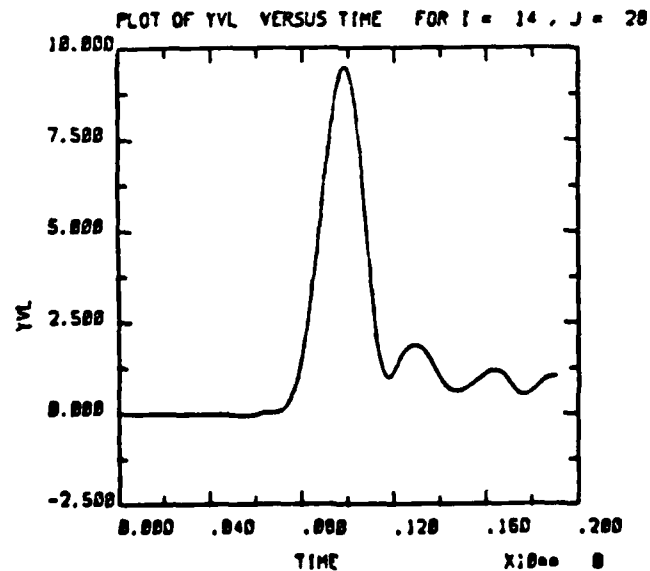
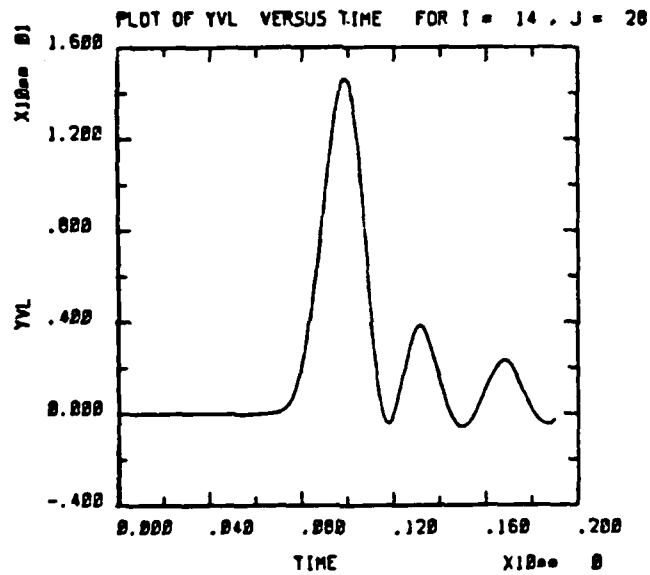
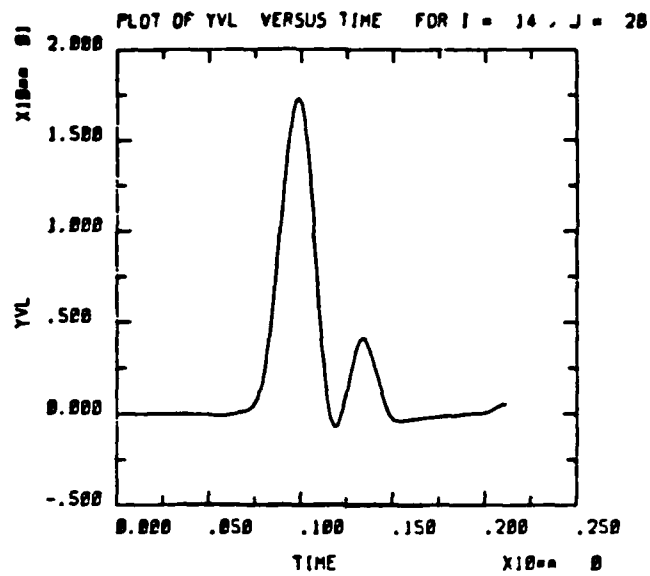


1 Mt comparisons of the 1 layer Non-hysteretic EOS (Run No. 1),  
1 layer hysteretic EOS (Run No. 4), and 2 layer hysteretic EOS (Run No. 7)

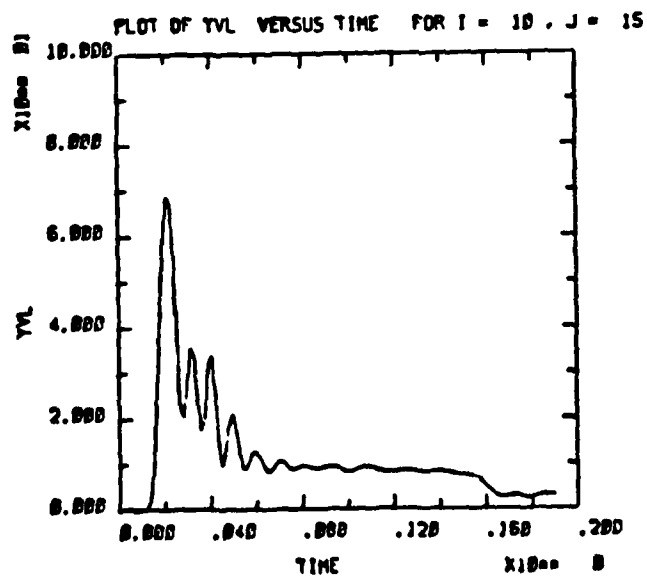
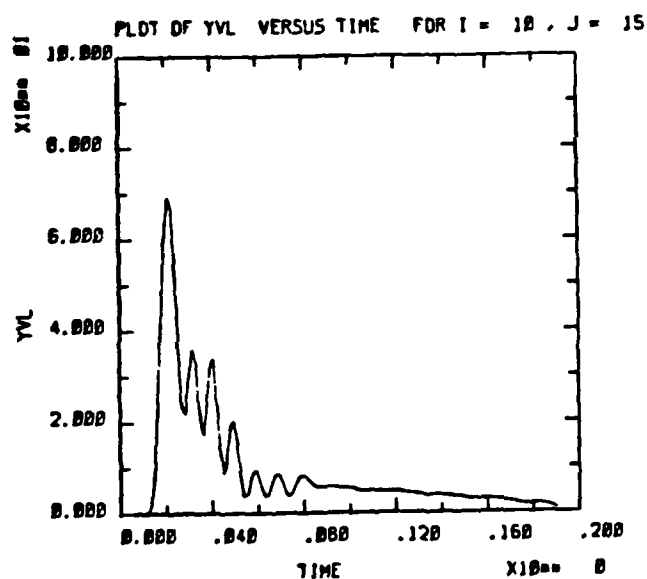
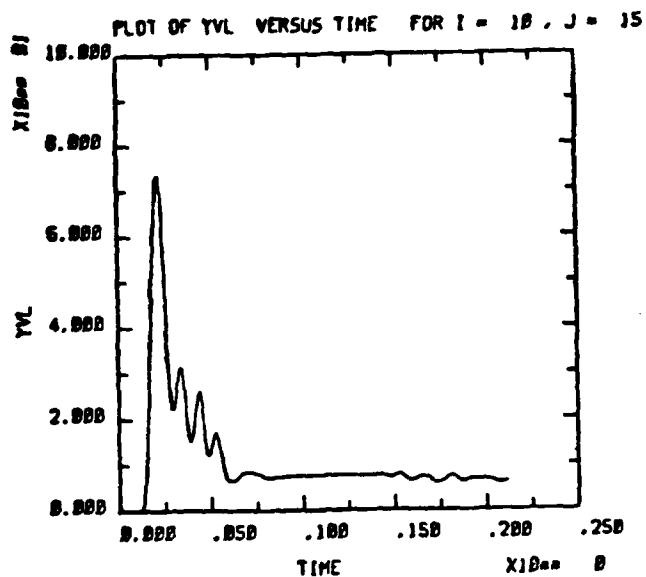


1 Mt comparisons of the 1 layer Non-hysteretic EOS (Run No. 1),  
 1 layer hysteretic EOS (Run No. 4), and 2 layer hysteretic EOS (Run No. 7)

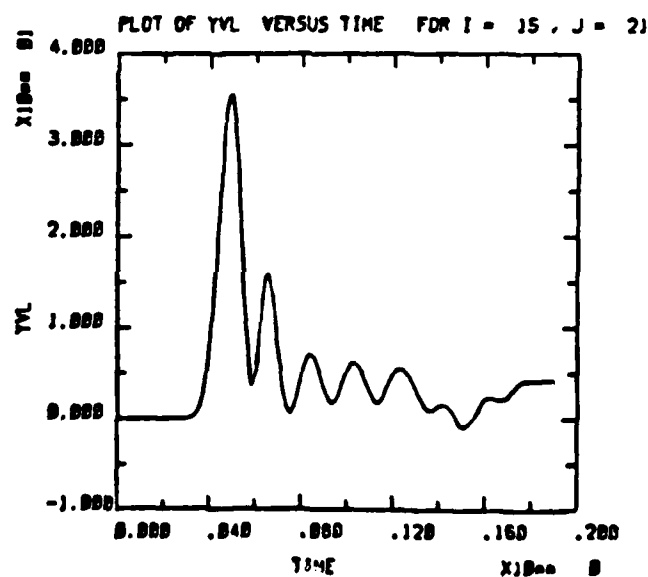
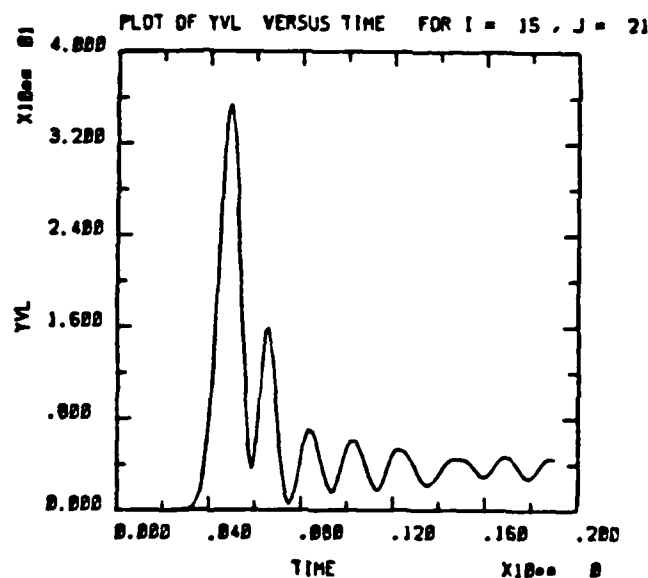
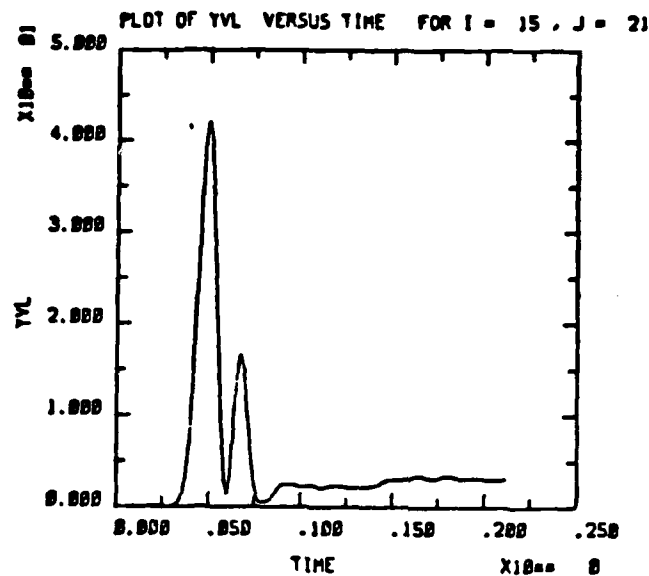




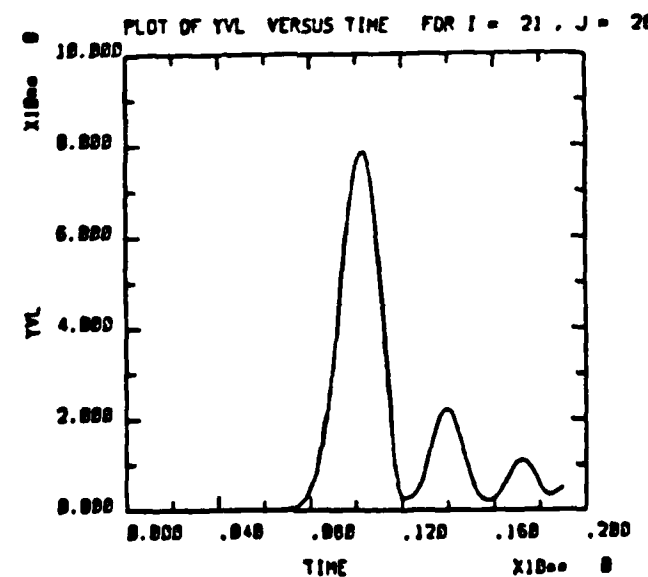
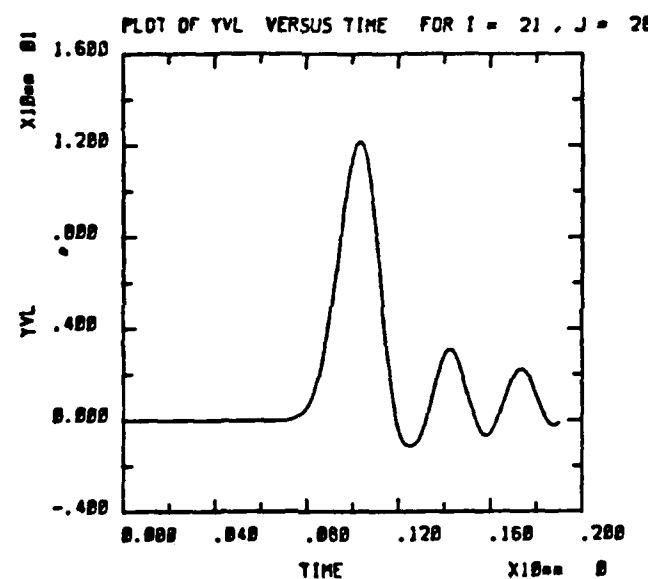
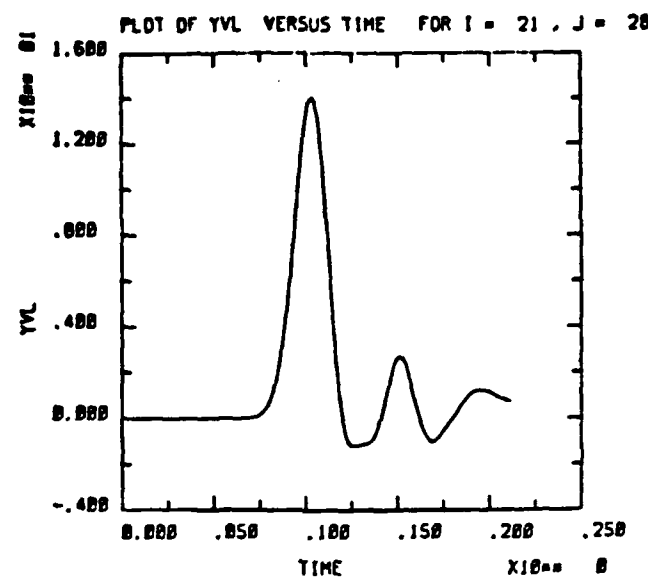
1 Mt comparisons of the 1 layer Non-hysteretic EOS (Run No. 1),  
 1 layer hysteretic EOS (Run No. 4), and 2 layer hysteretic EOS (Run No. 7)



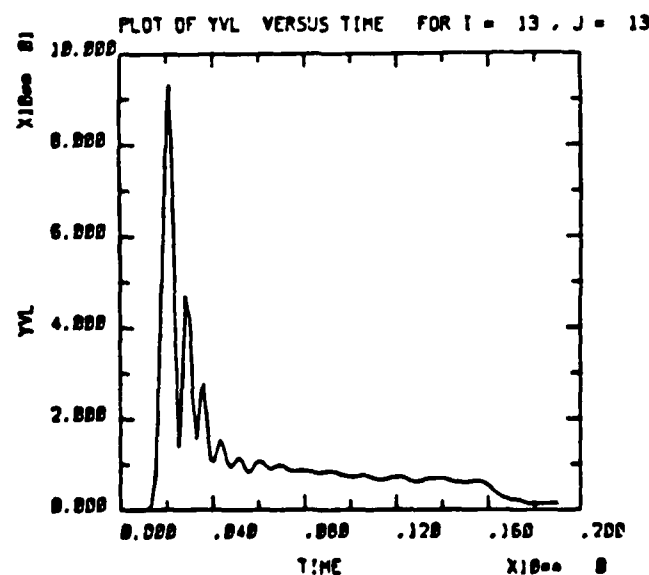
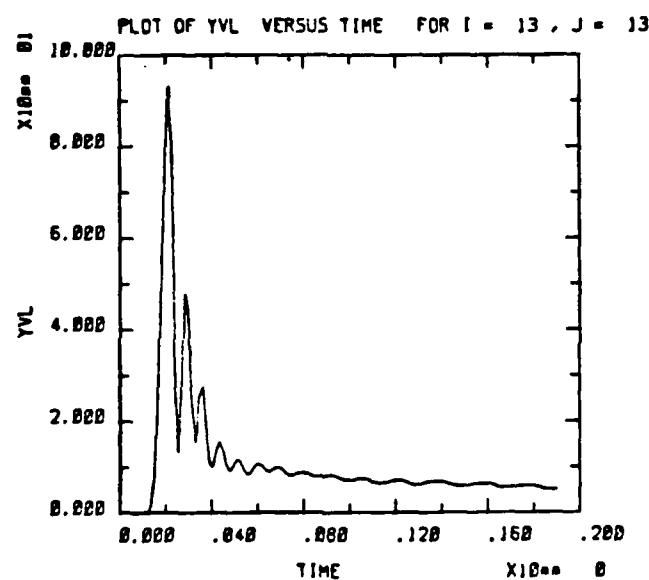
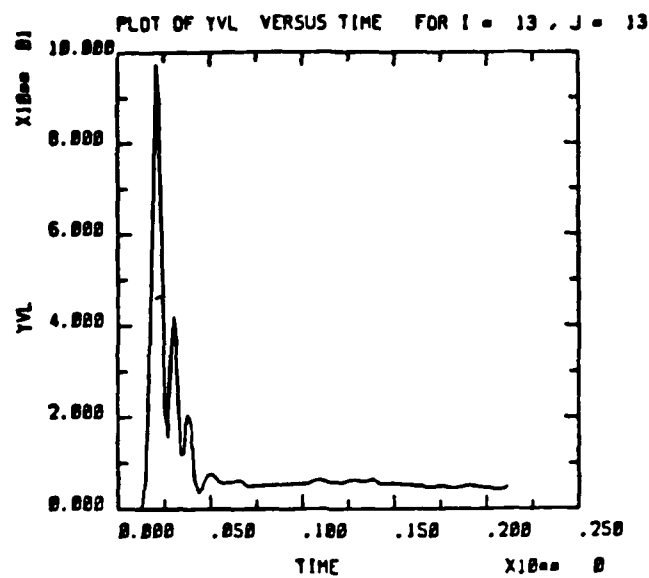
1 Mt comparisons of the 1 layer Non-hysteretic EOS (Run No. 1),  
 1 layer hysteretic EOS (Run No. 4), and 2 layer hysteretic EOS (Run No. 7)



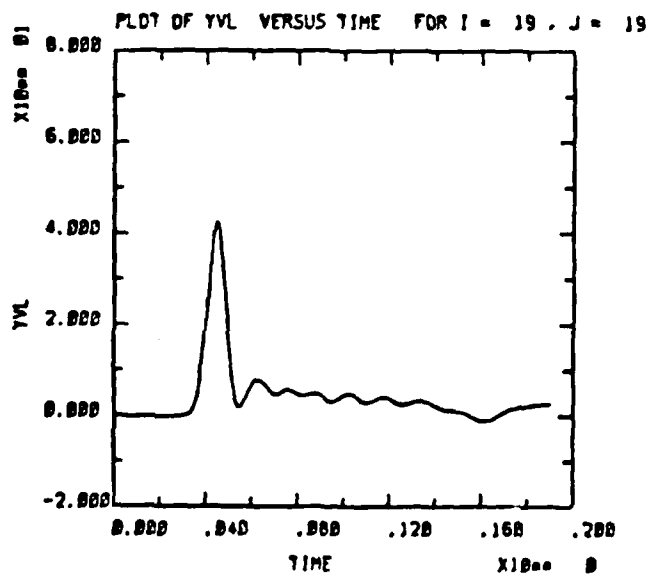
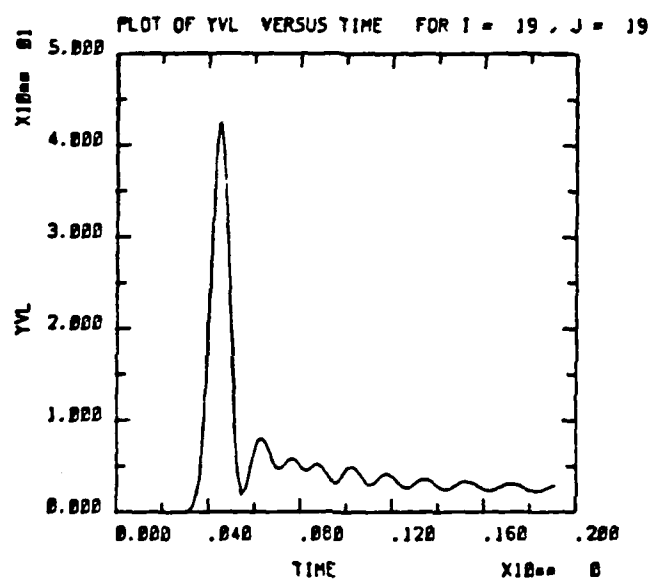
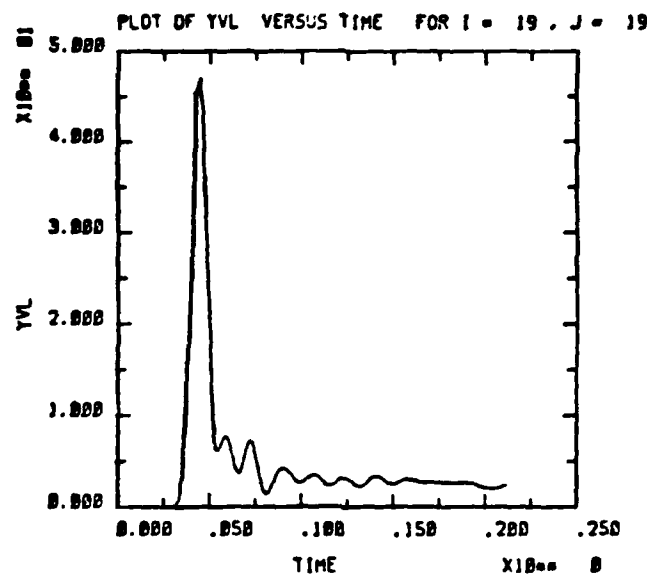
1 Mt comparisons of the 1 layer Non-hysteretic EOS (Run No. 1),  
 1 layer hysteretic EOS (Run No. 4), and 2 layer hysteretic EOS (Run No. 7)



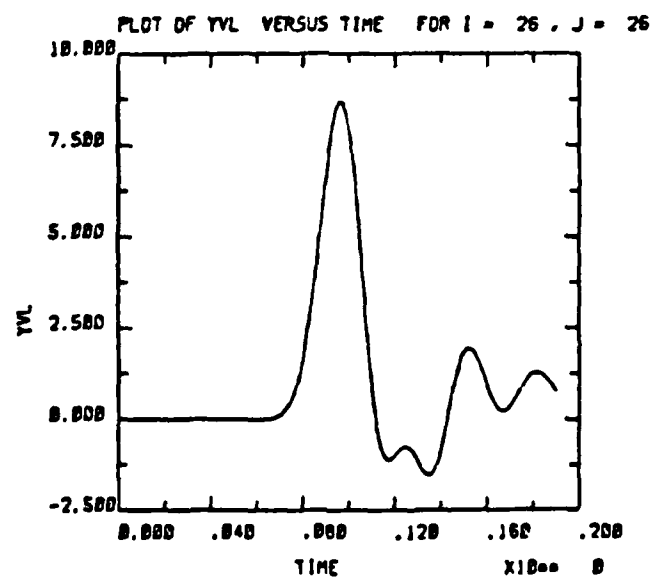
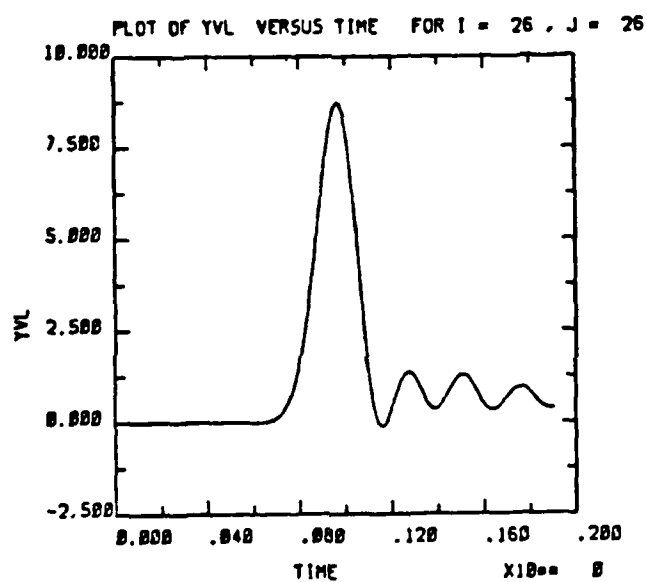
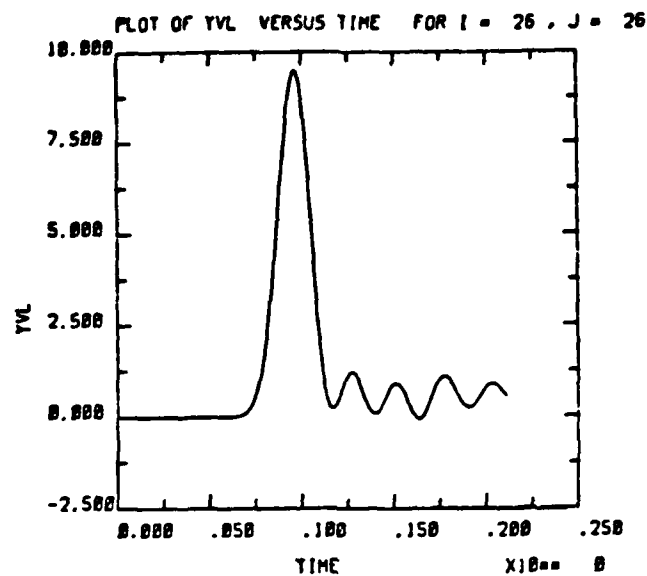
1 Mt comparisons of the 1 layer Non-hysteretic EOS (Run No. 1),  
 1 layer hysteretic EOS (Run No. 4), and 2 layer hysteretic EOS (Run No. 7)



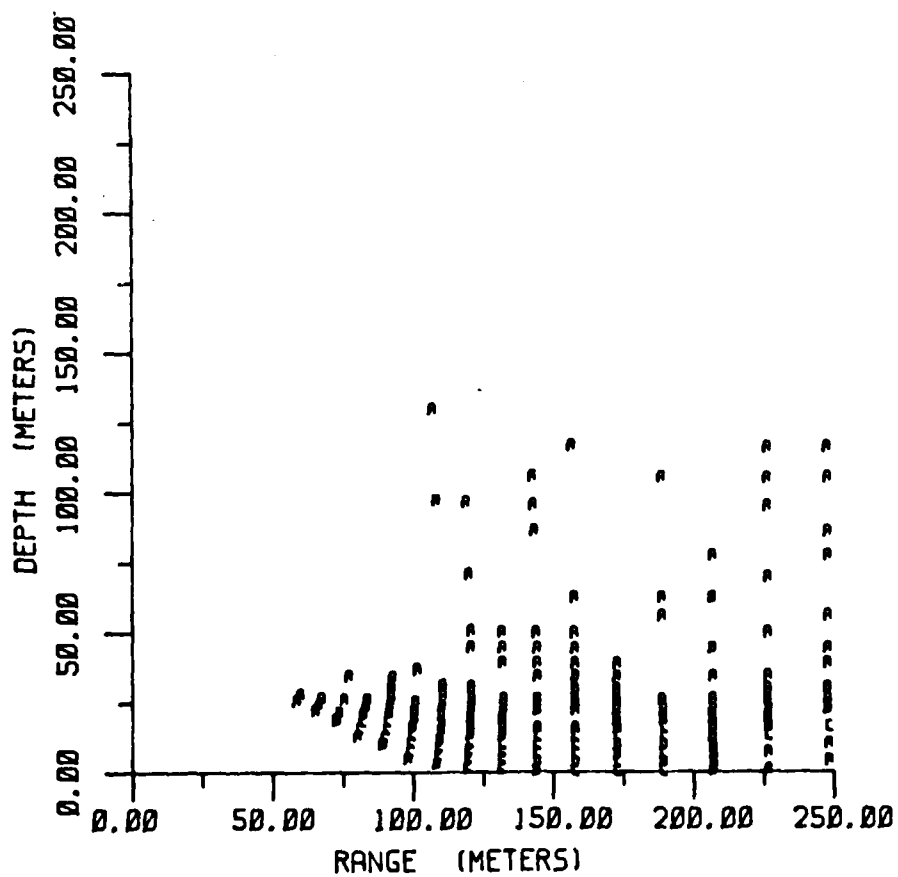
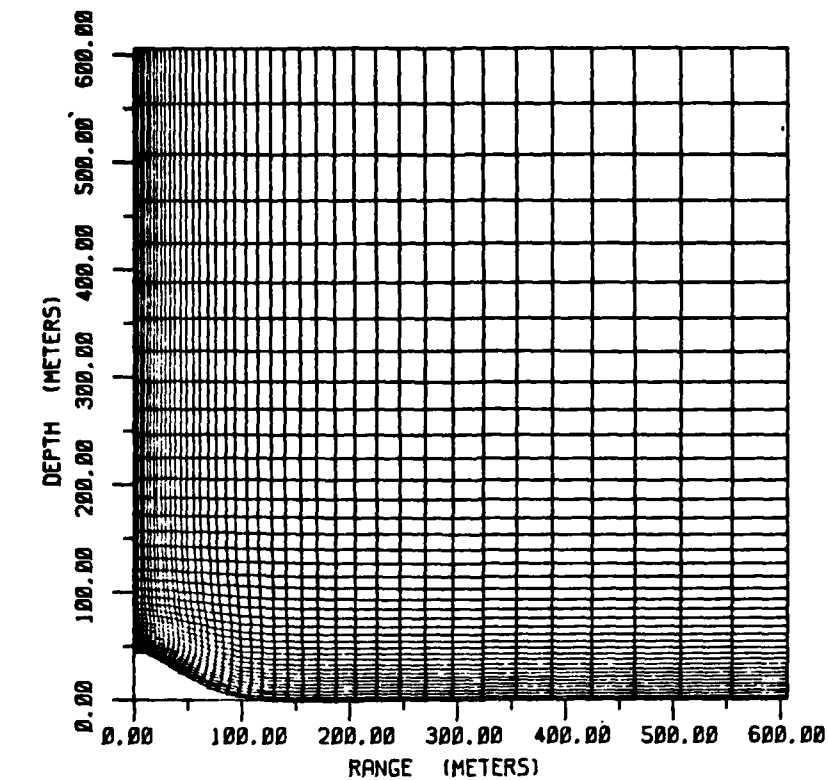
1 Mt comparisons of the 1 layer Non-hysteretic EOS (Run No. 1),  
 1 layer hysteretic EOS (Run No. 4), and 2 layer hysteretic EOS (Run No. 7)  
 B-40



1 Mt comparisons of the 1 layer Non-hysteretic EOS (Run No. 1),  
 1 layer hysteretic EOS (Run No. 4), and 2 layer hysteretic EOS (Run No. 7)

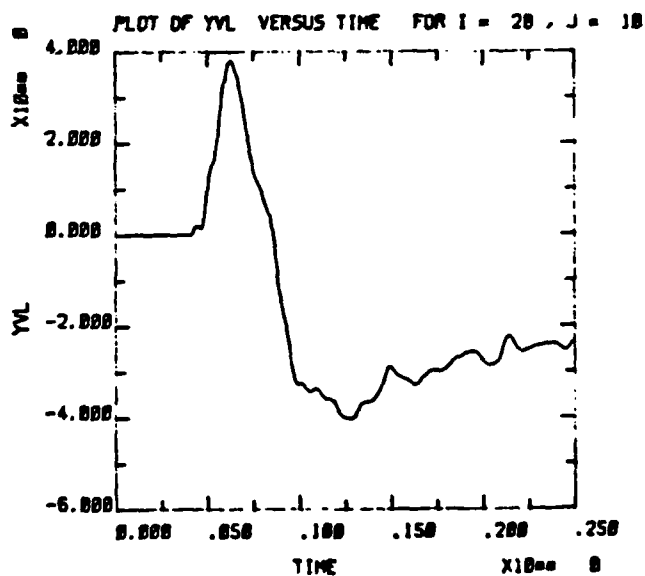
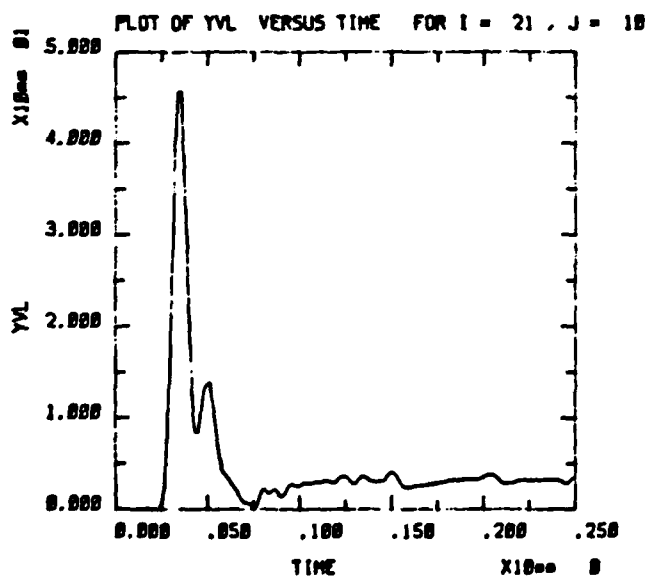
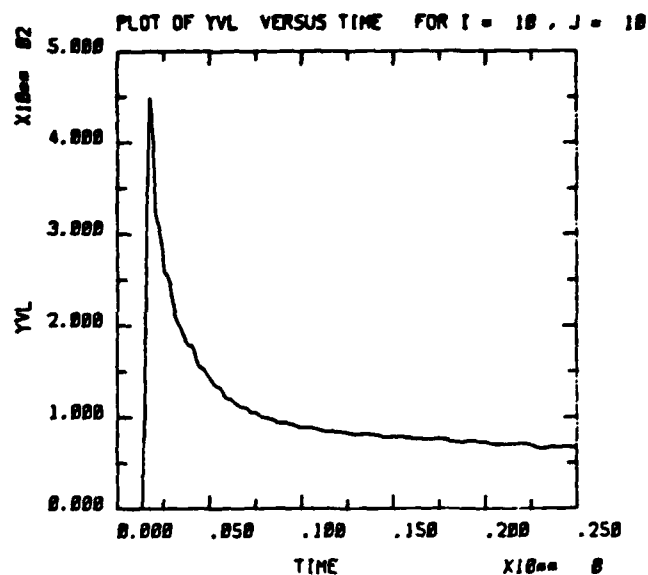
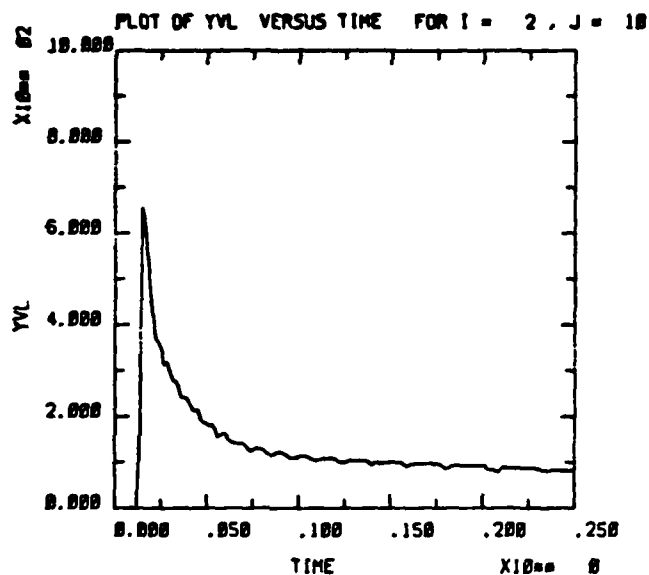


1 Mt comparisons of the 1 layer Non-hysteretic EOS (Run No. 1),  
 1 layer hysteretic EOS (Run No. 4), and 2 layer hysteretic EOS (Run No. 7)



Run 8 Deformed Grid and Spall Indicators





INT AMPLD TIME .25025 CYCLE NUMBER 479

Run 8 Velocity-Time Waveforms

**END**

**FILMED**

**11-85**

**DTIC**